Manufacturing Repeatability Study of a Titanium Electron Beam Melting Additively Manufactured Topology Optimized Tapered Box Beam Structure

Eric David Bol

A thesis

submitted in partial fulfillment of the

requirements for the degree of

Master of Science

University of Washington

2020

Committee:

Ramulu Mamidala

Junlan Wang

Dan Sanders

Program Authorized to Offer Degree:

Mechanical Engineering

University of Washington

Abstract

Manufacturing Repeatability Study of a Titanium Electron Beam Melting Additively Manufactured Topology Optimized Tapered Box Beam Structure

Eric David Bol

Chair of the Supervisory Committee:
Ramulu Mamidala
Department of Mechanical Engineering

For metal additive manufacturing to fully penetrate into the commercial aircraft industry the process must be stable and repeatable. The product safety of high-quality serial production components is directly related to manufacturing repeatability. Three experiments were carried to understand the repeatability of the electron beam melting powder bed fusion additive manufacturing process using an Arcam A2X with Ti-6Al-4V. The first experiment studied a single beam segment while the second looked at the layering and hatch scan effects. This study culminated in a tapered box beam resembling a scaled down commercial aircraft engine pylon forward strut box that was designed for additive manufacturing using 3D topology optimization. The final design had an asymmetric organic-like truss structure that was manufactured in two

halves. A series of three builds was executed to produce six beam specimens that were topologically 3D scanned to determine the variation from the CAD model and part to part.

TABLE OF CONTENTS

LIST OF FIGURES

LIST OF TABLES

NOMENCLATURE

3D	Three Dimensional
AM	Additive Manufacturing
CAD	Computer Aided Design
CMOS	Complementary Metal Oxide Semiconductor
DED	Direct Energy Deposition
DfAM	Design for Additive Manufacturing
DfMA	Design for Manufacturing and Assembly
DMLS	Direct Metal Laser Sintering
EBM	Electron Beam Melting
FEM	Finite Element Method
FFF	Fused Filament Fabrication
GE	General Electric
HIP	Hot Isostatic Pressing
PBF	Powder Bed Fusion
PRS	Powder Recovery System
SARP	Society for Advanced Rocket Propulsion
SLM	Selective Laser Melting
SLS	Selective Laser Sintering
STL	stereolithography
UTS	Ultimate Tensile Strength
YS	Yield Strength

ACKNOWLEDGEMENTS

This work was partially accomplished using facilities funded by the Joint Center for Deployment and Research in Earth Abundant Materials (JCDREAM) in Washington State. The authors also sincerely acknowledge the Boeing Pennell Professorship funding and Mr. Bill Kuykendall of Mechanical Engineering for his assistance on ARCAM machine during this investigation. The Boeing Learning Together Program is appreciated for providing tuition funding in support of this work.

In addition, I would like to acknowledge the excellent career coaching provided by Jade Husdon, a Senior Manager at Boeing, which inspired me on a path to seek a higher degree. Dr. Dan Sanders provided me the much-needed mentoring and encouragement to pursue education and research in metal additive manufacturing. Professor Ramulu Mamidala as my advisor guided me through completion of this work. Professor Julan wang graciously served as a member of my thesis committee. Curtis Doyle, a colleague, who provided assistance with the setup of the ARCAM machine and specimen data collection.

DEDICATION

I would like to dedicate this work to my loving wife, Raquel, and daughter’s Jasmine and Aurora, who are the ones that give this work real value and meaning.

Chapter 1. INTRODUCTION

Additive Manufacturing (AM), or otherwise known as three-dimensional (3D) printing, has changed and expanded much since first being developed in the 1980's [1-2]. Now the term additive manufacturing encompasses processes like stereolithography (STL), fused filament fabrication (FFF), powder bed fusion (PBF), and direct energy deposition (DED), all of which have numerous sub categories and material options. In terms of metal AM, the most common is the powder bed fusion which grew out of the early selective laser sintering (SLS) process that used a laser to sinter polymer powder. While the lasers at the time did not have the power to go to full melting, the heat sources of today all fully melt the powder feedstock material. If the heat source is a laser, the process is referred to as selective laser melting (SLM). Some of the most common manufacturers of metal PBF SLM machines are Renishaw, Concept Laser, SLM Solutions, 3D Systems, and EOS. If the heat source uses an electron beam the process is called electron beam melting (EBM), and the only manufacturer of this process at the time of this work is Arcam who is now owned by General Electric [3].

There are many benefits with metal additive manufacturing, one of which is by being an additive process means waste is kept low. With the EBM process, only the powder material needed for the final part is used with minimal amount of powder lost, material removed in post-processing, or supports scrapped. Many design engineers are excited about the design freedom AM technology promises. Where they were once constrained by the manufacturing processes such that they were able to design objects that could not be built, now they can build objects they cannot design. Topology optimization is a finite element based mathematical field that is growing thanks to additive manufacturing since the organic truss structure shapes the optimization algorithms generate can be more easily manufactured [4]. Additive began with polymers so initially it was useful for prototyping and remains so today, but now it has moved beyond with the capability to produce actual functional metallic parts. In this way lead times can be dramatically shortened and quantity of tooling reduced since this one tool can manufacture numerous parts of any shape.

Additive manufacturing, specifically PBF, does have several drawbacks as well, as seen in Figure 1.1 [1-2]. Most notably is that the machines are expensive and their manufacturing is not well controlled. The machines may initially behave as if they are prototypes where two of the same machines side by side can be given the same build file, but end up with different results in quality. This is due to the large number of parameters that can affect the build and are difficult to control precisely. Another part of the expense is the raw feedstock powder material is much more expensive than plate or sheet stock. While the machines themselves are very large, the build volumes are still quite small. Printing is also very slow taking tens of hours or days per build. Larger build volumes take even longer to print and that leads to more challenges and risk in keeping a machine operating uninterrupted for that amount of time.

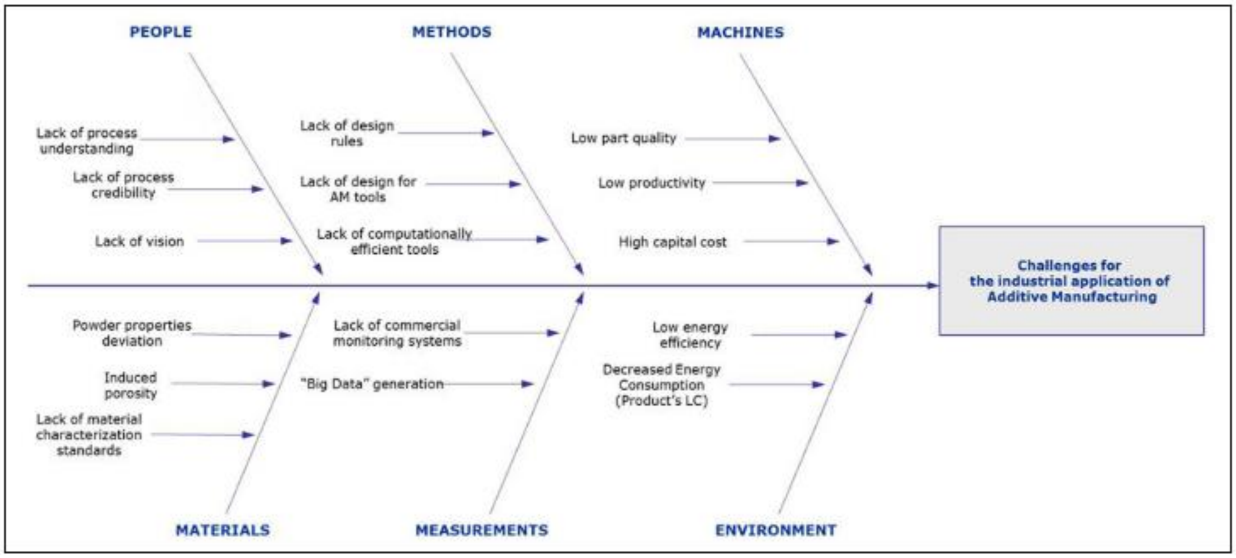

Figure 1.1. Challenges of applying additive manufacturing to industry [2].

Still, metal PBF additive manufacturing applications are finding their way into commercial products as more knowledge is gained on the effects of processing parameters. Two of the biggest industries to take advantage of this technology are the medical and aerospace industries [2-3,5]. Applications in tooling can allow for conformal cooling channels to be inserted near the surface to shorten heating and cooling cycles. General Electric has been the biggest and most successful adopter of additive manufacturing due to their GE LEAP fuel nozzles pictured in Figure 1.2 [1,3]. GE has taken such large steps to control the whole additive eco system from powder production with the acquisition of AP&C, to acquisitions of Concept Laser (SLM) and Arcam (EBM) machine manufacturing, to GE Addworks design solutions, and GE power providing uninterruptable quality power sources. Other aerospace industry companies such as Boeing and Airbus have taken more cautionary approaches to metal AM, but are eagerly searching for the right application at the right price.

Figure 1.2. Metal additively manufactured GE LEAP engine fuel nozzle [3].

In this work is an in-depth look at the metal powder bed fusion electron beam melting additive manufacturing process with an Arcam A2X machine and Ti-6Al-4V powder feedstock. The process is described by taking a topology optimized three-dimensional computer model and translating that into a build file that the machine can read and know where in the build volume it needs to melt. The purpose of this investigation is to understand the repeatability of the additive EBM process when it comes to manufacturing engineered components. The EBM system setup and operation of the machine is first discussed, as well as the most common defects that can occur during a build are identified. Just as important as the process is what one can expect to come out in terms of the metal microstructure and mechanical properties, and how those can be affected by the powder feedstock and the melting process.

In this thesis work, two experiments were conducted that analyzed the topology of the metal melt at the micro and macro scales before a third experiment was performed looking at actual part manufacturing. Given a particular 3D geometry, there is question as to how well the Arcam A2X manufactures that same component at different locations within the build chamber, and from one build to another. By discovering sources of variability within the metal 3D printing process it will lead to greater understanding and process control. Only when the manufacturing process is stable and repeatable will additive begin to reach its full potential to revolutionize product performance in industries and bring about the next step change in product capability.

The objective of this work was to understand the repeatability of the EBM process for manufacturing an engineered component that was designed for additive manufacturing. To achieve this a procedure was developed which consisted of a series of three experiments that built upon each other. The first, the Line build, was a one-dimensional fundamental look at the topology of a single melt line with two different sets of process parameters in order to determine the minimum feature size. The second, the Step-Ramp build, was a two-dimensional assessment of manufacturing repeatability within the build chamber by horizontally printing numerous very thin specimens and analyzing the melt topology of the part infill versus the thermal mass (i.e.

thickness). The third and final experiment, the Tapered Box Beam, examined geometric repeatability and dimensional deviation from build-to-build with a designed for additive manufacturing engineered component.

Chapter 2. BACKGROUND

The aerospace industry has been investing in metal additive manufacturing for the benefit of being able to print parts that are lighter weight and more capable than those manufactured with traditional methods. High quality serial production is important in this industry as it directly impacts product safety; therefore, the manufacturing repeatability of additively manufactured components has to be proven prior to wide implementation. Electron Beam Melting, a powder bed fusion form of additive manufacturing, is capable of producing fully dense titanium components where an electron beam is used as the energy source to selectively melt Ti-6Al-4V powder within a heated build chamber to produce a 3-dimensional part. This technology promises designers the freedom from the design constraints imposed by traditional manufacturing techniques (e.g. machining, casting, etc.) with the capability to print complex structures that could not be manufactured any other way, such as those generated by topology optimization codes. While topology optimization algorithms have been used previously to optimize the weight of metallic structures, they often generate complex organic like shapes that cannot be manufactured with traditional methods, or at least in a cost-effective way. Therefore, traditional manufacturing has limited the optimization applications due to various rules and restrictions of the fabrication methods.

2.1 ELECTRON BEAM MELTING PROCESS

The powder bed fusion EBM process uses a powerful electron beam as a heat source to selectively melt a powder feedstock. The process takes place in a vacuum chamber where electromagnets guide the beam and can sustain multiple melt pools simultaneously. When the electron beam is powered and melting the powder it is also electro-statically charging the metal particles. A schematic of the EBM system is shown in Figure 2.1. For this reason, each build layer is worked in a two-step process where the entire top layer of powder is first preheated and sintered by an unfocused high velocity beam scan. Then the beam selectively melts the areas of the layer that are designated to make the part [1,3-6].

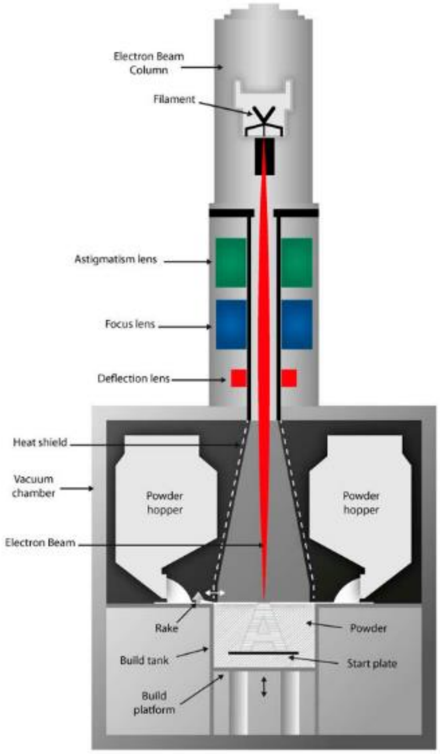

Figure 2.1. EBM system Schematic [1].

The melting step also takes place in two scanning stages referred to as contouring and hatching, but either can be done before the other. Contouring is an outline scan of the part cross-section which is meant to improve the surface finish of the part and accomplished in one or more concentrically offset passes. Hatching is how most of the melting takes place and is done in a variety of back and forth rastering patterns. Unlike a laser system, the near instantaneous deflection of the electron beam enables the machine to maintain multiple melt pools simultaneously which allows for an increase in the build speed. After the selective melting on a given layer has been completed, the build area is lowered slightly and a rake distributes a small quantity of new powder from a hopper before the preheating of the next layer takes place. This process repeats for each layer until the full height of the build is complete. Figure 2.2 shows images of the build chamber during a layer cycle along with the beam current and grid voltage extracted from the log file. [1,4-5].

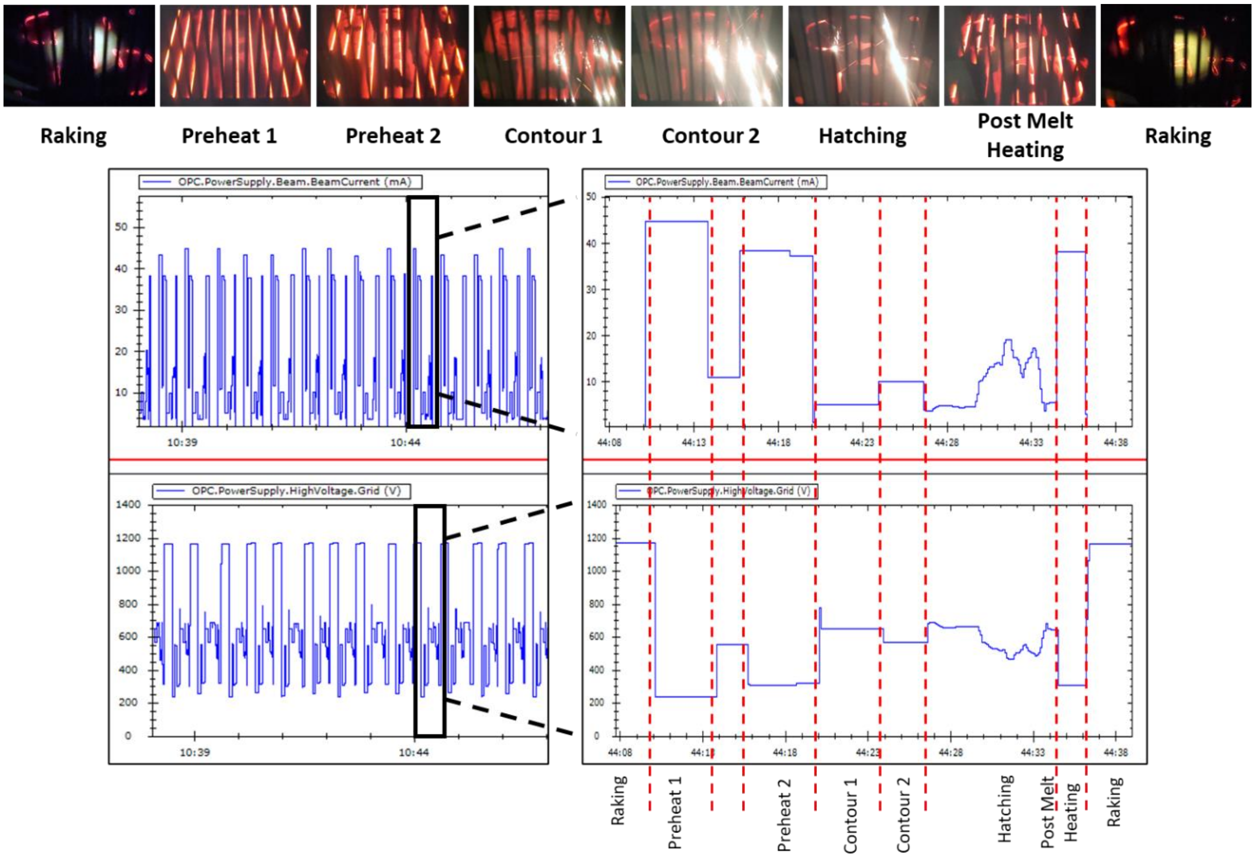

Figure 2.2. EBM layering process shown for each step of the cycle with the beam current (top) and grid voltage (bottom).

2.1.1 *Inputs*

Before a build can take place, the machine has to know what it will be manufacturing. This begins with a 3D computer aided design (CAD) model or 3D scan model. Typical commercial software for producing these models are SolidWorks, CATIA, NX, etc., and the model file formats are typically proprietary to the software that created it. There are some formats that are neutral in order to enable files to transfer between programs, such as .stp and .iges as some of the more common types. All CAD models have to be transformed into a .stl file triangulated mesh representation before they can go to a printer and this flow is shown in Figure 2.3. The triangulated mesh enables the model to be processed by slicing software that generates the scan/tool path for each layer of the part so a printer can manufacture it [2,5,7-8].

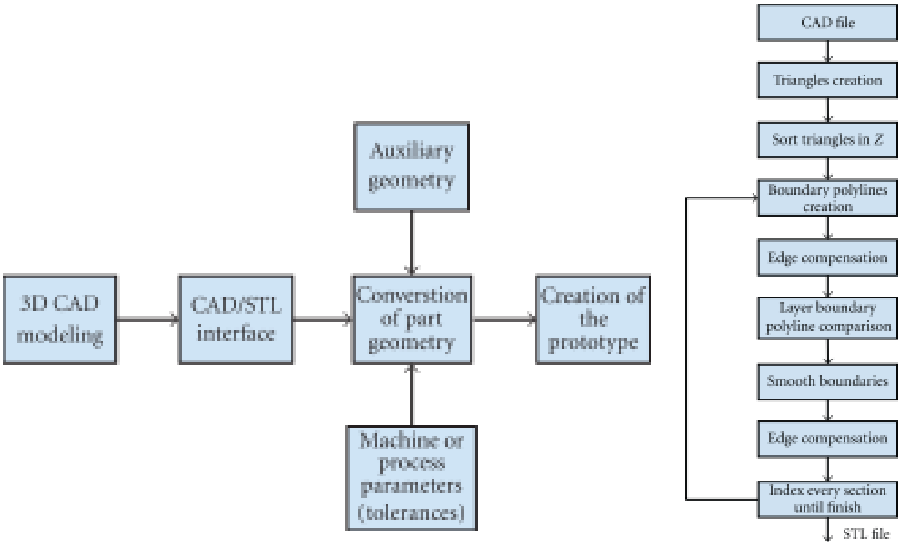

Figure 2.3. Data flow in rapid prototyping (left) and data flow of .stl file creation (right) [8].

STL is an abbreviation for "stereolithography," created by 3D Systems [8], which has been the de facto standard for file formats for additive manufacturing across multiple industries since the mid 1980's. The .stl file only describes the exterior surface geometry of a three-dimensional model with no representation for color, texture or other model attributes. They also contain no scale information, and the units are arbitrary. All existing CAD programs allow the saving of 3D models in .stl format which usually requires defining a "sag" and "step" value for an unstructured triangulated surface mesh. The number of triangles needed to describe a smooth curved surface as AM technology approaches micron scale resolution greatly inflates the file size. This in turn leads to file errors or the users choosing poor tessellation values sacrificing accuracy to keep the file size manageable. Poor .stl files that contain errors are also common, such that an entire software platform called Materialise Magics originated around repairing badly tessellated CAD models so they could be processed for 3D printers.

Materialise Magics is the most common commercial software for preparing build files for all kinds of 3D printers. This is where multiple .stl formatted models can be loaded and arranged into a representative build volume for the machine. Improperly arranged or oriented parts can lead to build failures so the user preparing the build file must be cognizant of the geometry and the limitations of the printing process. In addition to just placing models in the build volume, a build file must contain support structures that serve many purposes. Supports are needed to anchor the part in the build chamber either to another part or the build plate. They are also needed to support the part if there are overhangs at small angles with respect to the planar build surface. In the EBM process especially, the supports are needed to function as heat sinks to help conduct the heat from the melt area into the surrounding powder. Figure 2.4 displays an example of what can go wrong when supports are not utilized. Supports are typically porous thin walls that are sacrificial and manufactured with less strength than the actual part to facilitate easier removal.

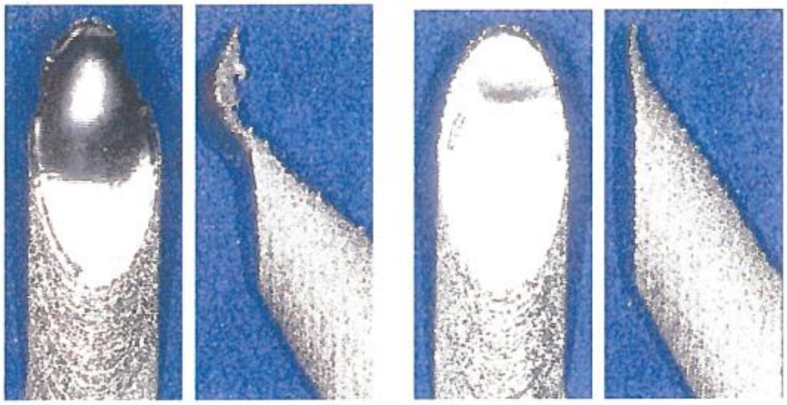

Figure 2.4. Truss members without supports show distortion at small angles with respect to the planar build surface [4].

Once the build volume has been arranged with parts and supports for the build, it is exported and loaded into the Arcam machine software for slicing and beam path generation. Slicing is where the representative build volume is divided into print layers like a cake based on the desired layer thickness. Where parts and supports are located in the layer, a beam scan path is specified for full melting. A contour scan will melt the outline of the objects being built while the infill hatching scan will melt the interior solid portion which can be done in a unidirectional, bidirectional, spiral, zig-zag, cross-wise, or checkerboard pattern. Supports are treated differently than the parts in that to make them weaker and easier to remove they only get melted at lower power or every other layer. Once the software automatically generates the build file that contains the build instructions for the machine, it can be loaded into the machine for build execution [1-2,4-6,8].

2.1.2 *EBM machine*

An electron beam powder bed 3D printer consists of two main parts. First and foremost is the build chamber with a large door on the front with an observation window. Next to it is a controller cabinet that contains the operator interface, pumps, and cooling manifold. External to the main machine is the powder recovery station, helium supply, and miscellaneous support and cleaning equipment [1].

The build chamber is where the manufacturing of the parts takes place as shown in Figure 2.5. Since the electron beam can only operate in a vacuum, the chamber has to be completely sealed off from the surrounding environment. At the top of the chamber is a tungsten filament that when energized generates the beam. Just below the filament the beam will pass through a tall column of electromagnet coils that steer and focus the beam onto the build surface. The build area surface contains a substrate stainless steel build plate and the powder to be melted. To the left and right sides of the build area are powder hoppers where the powder is stored, and there is a rake that can move across the build surface between them that collects and distributes the powder for each layer [3,5-6].

Below the build surface is a box that the sintered and melted powder descends into. There are also catch containers on either side of the build tank that can be seen in Figure 2.5 that collect any powder that spills from above as well as the power that drops through holes to both sides of the build area. As the rake sweeps powder across the surface, powder falls through these holes past sensors that detect it to serve as a method for detecting rake movement. Located above the build area is a cone of sheet metal heat shields that protect the hoppers and walls of the build chamber from degradation by repeated exposure to the extreme environment inside while the machine is operating. There is also a camera positioned to observe the build area with a sacrificial Kapton film that protects it from damage by vaporized particulates [5,9].

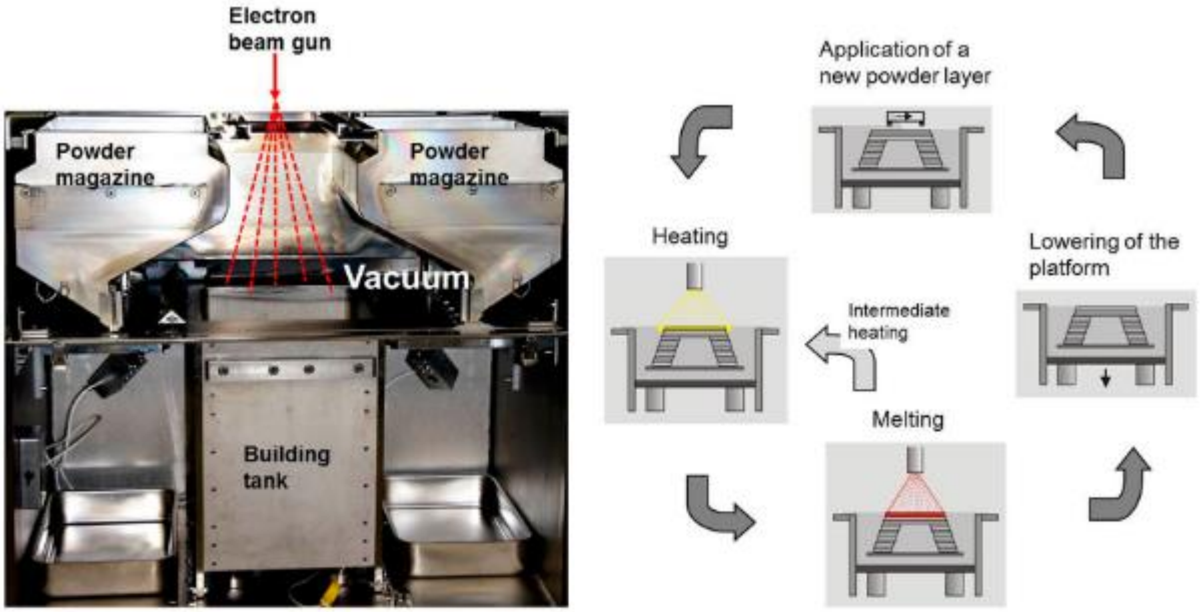

Figure 2.5. EBM Process chamber (left), 4-step process for building a layer (right) [5].

The powder is first loaded into the build chamber by an operator during the setup process. The hoppers must contain all of the powder necessary for the build since it is not possible to add powder while the machine is operating. Fresh powder is fed to the build area by gravity. When the hoppers are placed inside, the operator pulls the gate from the bottom allowing the powder to flow out and pile on either side of the build area. The rake is responsible for distributing the powder evenly across the build area. Between each build layer sequence, the rake moves into the pile of powder under a hopper until the set quantity of powder falls over the top in front of it. Then as the rake is moved back across the build area the powder in front is swept evenly across. The rake will often times make multiple passes depending upon the layer thickness [5].

When a build is complete, the parts are stuck inside a cake of sintered metal powder. To get them out the machine is first cooled and pressure restored. Once the door is open and the heat shields removed, the build is raised up to expose the metal cake imaged in Figure 2.6. It is then transitioned into the powder recovery station where it is manually abrasive blasted with pressurized air mixed with metal powder. The blasting removes the sintered powder to expose the parts seen in Figure 2.6 and the powder is filtered to be reused in subsequent builds. Not all powder gets reused since during the sintering process some particles melt together to form globs and these are filtered out as waste. Another source of waste is the support material which gets scrapped after it is removed from the part. Therefore, it is best to use as few supports as needed to achieve a successful build [5].

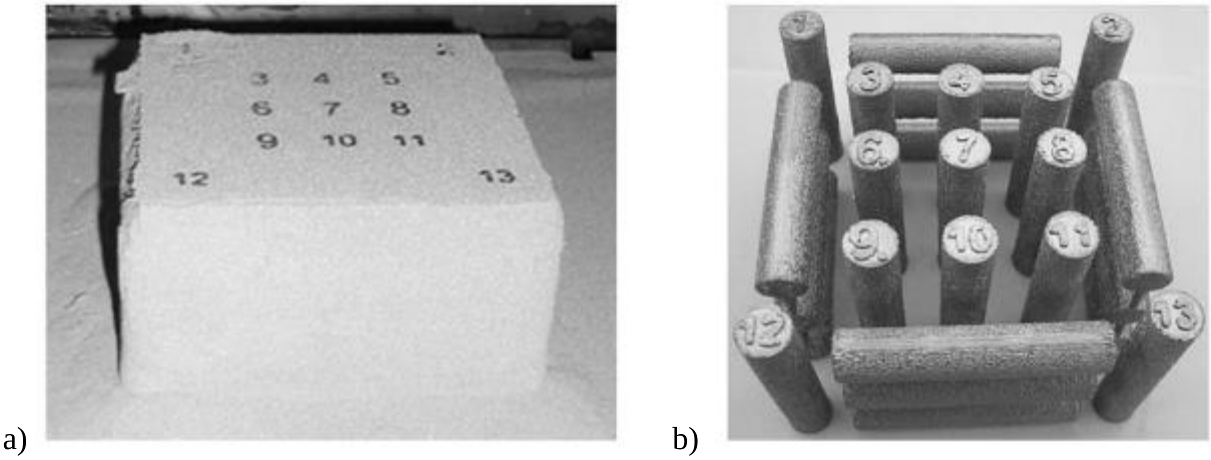

Figure 2.6. Image of completed build sintered powder cake (a) and build after sintered powder has been removed at the powder recovery station (b) [5].

The setup of the machine prior to each build is a very manual process that takes several hours. Even once the build file has been prepared and loaded into the machine, there is still the calibration and meticulous cleaning that must take place before a build can commence. With the necessary powder loaded into the hoppers, the rake fetching of powder must be calibrated [7]. This calibration is accomplished by commanding the rake into the pile of powder beneath one of the hoppers and visually inspecting the quantity of powder that falls over the top in front of the rake. The rake fetch position is chosen and set at the desirable location when a quantity about the size of a pencil width is sitting in front of the rake to be swept; that must be set for both sides of the build area. Another calibration step involves the build plate leveling which is not automated.

The build plate “floats” on a bed of metal powder and is leveled by visually observing how powder looks as the rake passes over it and tapping an area with a hammer if it appears to be higher. The procedure is continued until the powder distribution across the plate appears even to the operator. Since the positioning of the build plate is not precise and operator dependent it is not recommended to build anything directly from the plate. Instead, best results are obtained by using support features for the first 5 mm of the build height.

Rake and build plate calibration are followed by very careful cleaning of the internal chamber and seals since pulling a vacuum can take 1 to 3 hours, or possibly never if there are any contaminating substances on the door seal or other leaks in the column assembly. After the door is closed and the chamber pumped down to the required vacuum pressure levels, the beam can be switched on, then centered, and the focus calibrated. Since the build plate is simply floating in the build chamber on powder and is not physically restrained to any locating features, the operator must manually center the beam on the build plate by visual observation. Then the beam focus must be calibrated for the nine regions of the build plate that is divided into a three-by-three grid. For each of the nine grid areas, two alternating beams are displayed and the operator must adjust the location of the beams until they visually appear to be a single beam. Once each location has been properly focused and calibrated, the operator may move on to initiating the build.

The build process involves the electron beam shown in Figure 2.7 that selectively melts areas of powder and the temperature of the melt pool can be several hundred degrees above the liquidus temperature of the material. Because of the rate at which the heat source moves in an EBM machine the temperature is highly transient and difficult to measure. The melt pool size in EBM is smaller than that of welding and so the material cools and solidifies more rapidly. Significant research has been put into finite element modeling of the melt pool in order to better understand the heat flows and cooling rates of the material through multiple layers [2,6]. Initially the build plate acts as a large heat sink that rapidly conducts the heat away from the melt area, but as the build layer gets further from the build plate it has less influence on the cooling. This is where the part geometry with respect to the build direction and support material can be highly influential in the heat dissipation from the top layer melt pool. These differences are of great significance to the formation of the grain structure and the resultant material properties such that it is undesirable for a final part to have different properties from one location of the build volume to another.

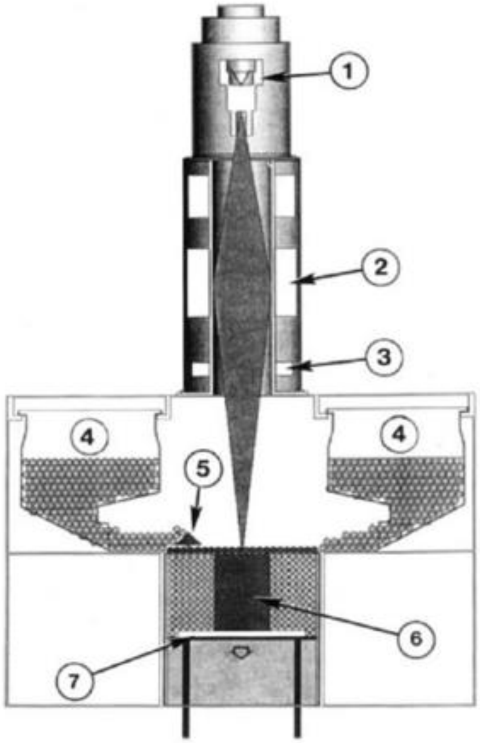

Figure 2.7. Schematic of an EBM machine 1) tungsten filament electron gun, 2) electro-magnet lens system, 3) beam deflection lens, 4) powder hoppers with feedstock, 5) rake, 6) component being built, 7) build plate [3].

2.1.3 *Process Parameters*

As with any manufacturing process there are process parameters that must be controlled to achieve a repeatable quality process. Additive manufacturing has many process variables that are actively being researched to determine their effects [1-2]. With the powder bed fusion electron beam melting process in Figure 2.8 some of the most critical are the preheating temperature, scan strategy, layer thickness, beam speed, and beam power.

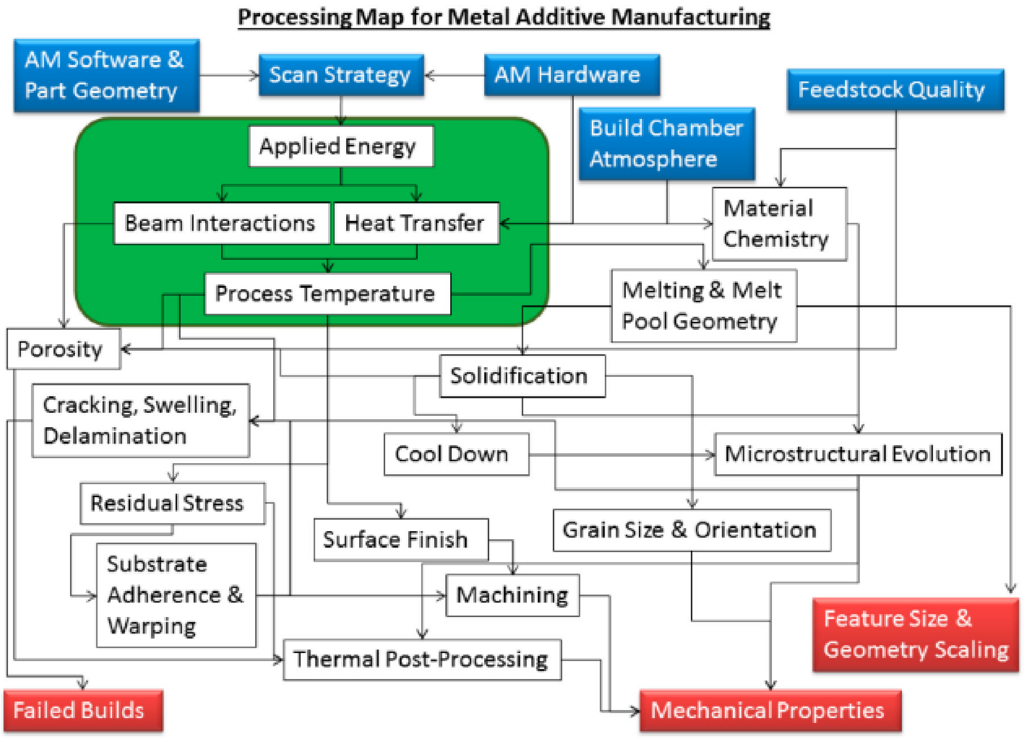

Figure 2.8. Overview of the relationship between process parameters and the underlying physics to achieve the desired outcome of metal additive manufacturing [1].

The preheating at the beginning of each new layer is done by scanning the beam across the entire build area at high velocity. In order to maintain the desired temperature for the material, the machine solves a one-dimensional thermal model [4]. That model balances the energy that will be lost by conductance through the powder with the energy input based on the area to be melted. The temperature of the bed is monitored by a thermocouple placed under the build plate and the preheat scanning is adjusted based on the feedback. If the thermocouple is not functioning properly or stops working altogether, the preheating could be too much or too little and a build failure will result.

The scanning of the melt beam typically takes place in two stages with the contouring scan and the hatching scan. Although both are not required and they can be done in any order, the chosen scan strategy can affect the quality of the components the machine is producing. The contour scan uses constant beam power and traces the edge of the part cross section in one or more passes with the purpose of improving the surface finish. With each pass the melt pool is set to a line offset parameter that will partially overlap the melted powder from the previous pass causing some mixture and remelting. The hatching scan for the part infill will raster the beam back and forth in a designated pattern. These patterns seen in Figure 2.9 and Figure 2.10 can be unidirectional, bi-directional, snaking, island scanning, spot melting, or a combination of any and all. In addition, the scanning pattern is typically rotated by a set angle from one layer to the next so that start, stops, and turns do not occur in the same location throughout the build layers. The goal of the scan strategy is to reduce residual stress build up and porosity within the parts and therefore incorporates a lot of variables that must be considered [1-2,4,6,10].

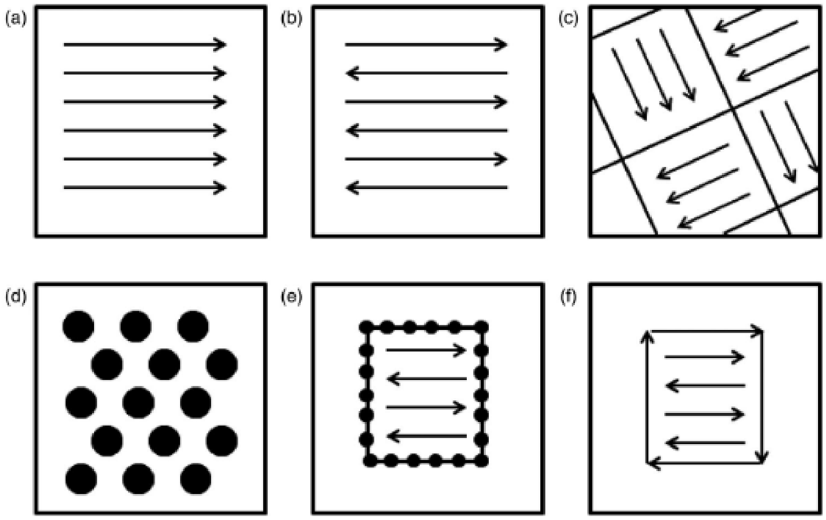

Figure 2.9. Illustration of scan strategies as seen from the top down: unidirectional fill (a), bi-directional fill or snaking (b), island scanning (c), spot melting (d), spot melting contours with snaking fill (e), line melting contours with snaking fill (f) [1].

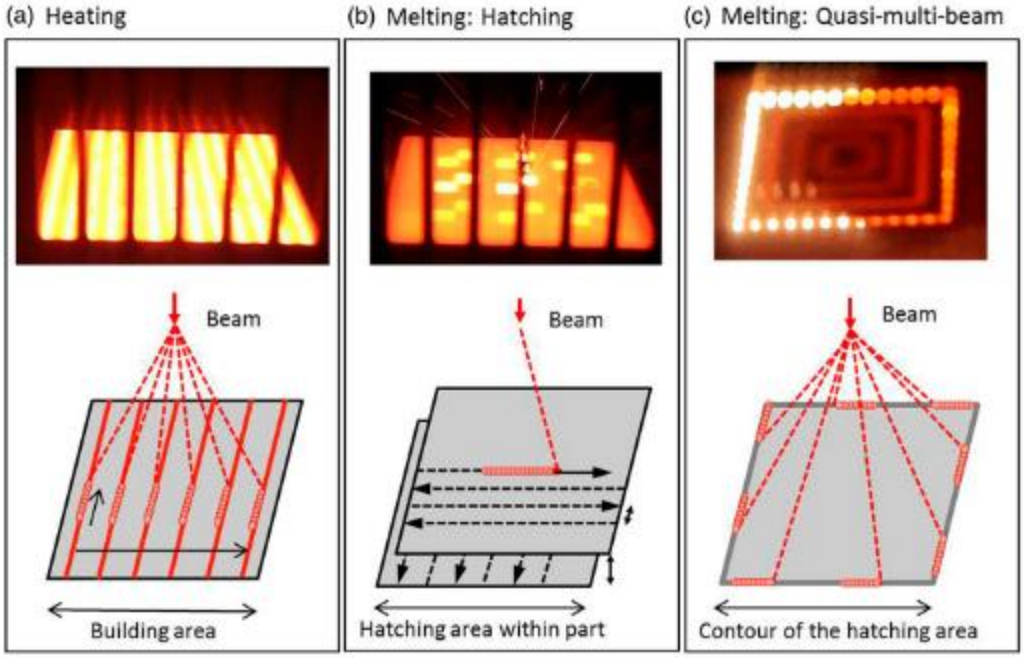

Figure 2.10. Heating and melting by hatching and contouring during the EBM process with photograph of actual process (top) with a schematic of the beam movement (bottom) [5].

During the hatching scan the beam power and speed is varied to keep the melt pool properties consistent. There are four analytical functions that get evaluated to determine the beam power and velocity, the first of which sets the beam current based on the length of the hatch line and is called the current compensation algorithm. Then the speed function sets the velocity based on the beam current to keep the melt pool size constant. The third is called the turning point function which reduces the beam energy near the beginning of each hatch line. The thickness function shown in Figure 2.11 is the fourth and that will reduce the beam energy input when melting close to an overhanging surface. The turning point and thickness function serve to reduce the energy where there will likely be significant heat accumulation [2,4].

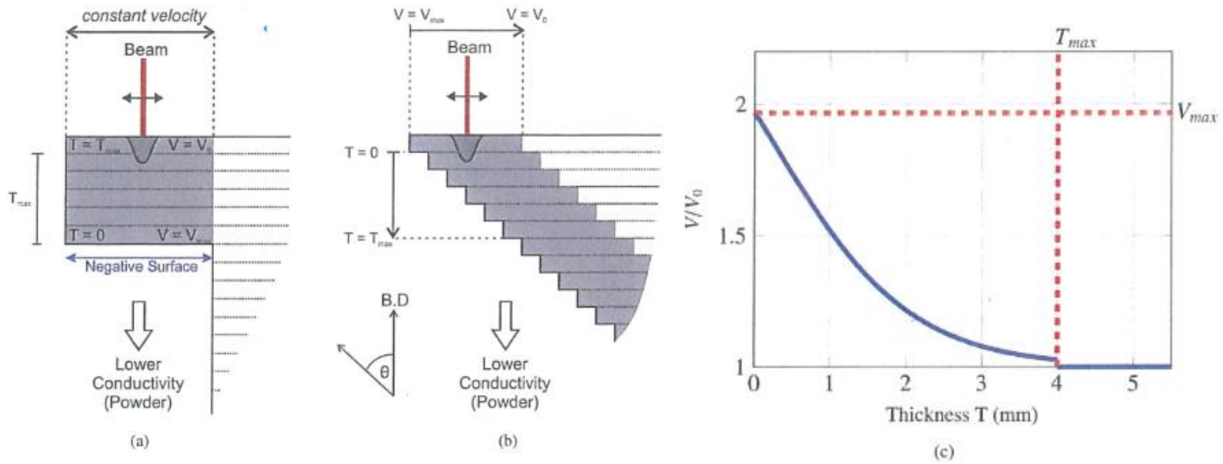

Figure 2.11. diagram of the EBM process melting overhanging features for a ledge type overhang (a), and a ledge type overhang (b). Dark regions show where thickness function is active. Also, the relative velocity profile with default thickness function parameters (c) [4].

2.2 DESIGN FOR ADDITIVE MANUFACTURING

It is common in research now to come across the term ‘Design for Additive Manufacturing,’ or DfAM, though it is rarely explicitly defined. This term is very similar to the traditional ‘Design for Manufacturing and Assembly’ (DfMA) which is where the design and optimization of a product is combined with a production system in order to reduce cost and development time, while increasing quality and performance. The design goals are therefore considered simultaneously with the manufacturing constraints that might include materials, assembly methods, energy sources, processes, maintenance requirements, market needs, and the end user. DfMA can further be broken down into different layers that are process-specific, feature-specific, and activity-specific, each with their own tools, techniques, and guidelines, with the intention of adapting a design for all the various downstream constraints. In essence it is just the exploration of the relationship between design and manufacturing, and how the top-level conceptual design is controlled by the subsequent steps necessary to get the product to market in the most cost-effective manner [13].

Because DfMA is seemingly so general, one might think it should also apply to additive manufacturing, just like saying, “Design for X;” however, additive manufacturing is so different in the tools, techniques, knowledge, methods, and processes that it requires a more specific term. Design for Additive Manufacturing is necessary since AM has the ability to create complex features that are very different from other manufacturing processes. The often-mentioned freedoms that AM brings can produce a component in one part that traditionally would have required an assembly of parts, and that capability can therefore reduce the importance and the need to design for assembly. The AM machine volumes and build times produce different batch sizes and cost drivers that are still being figured out and widely vary from one manufacturer to the next. Also, the feature complexity requires new approaches to quality control and metrology as will be demonstrated in later chapters. Overall, an entirely new body of knowledge is necessary to describe the different approaches to the practice of design that includes exploring large complex design spaces.

Design engineers tend to adhere to designs they have previously encountered which makes it difficult to evolve beyond the barriers imposed by conventional fabrication techniques. When presented with an empty design space, and an AM machine, the challenge becomes envisioning a marketable design that cannot be manufactured another way. It is important for engineers to find powerful additive examples to use as instruments for shifting mindsets and changing perspectives [14]. Topology optimization is a necessary tool for assisting the additive designer by generating seemingly infinite geometric examples that could satisfy some or all design requirements. As reported by Zhu et. al. [15] in their review of how topology optimization has been utilized in aircraft and aerospace structures, they recognize how effective the tool can be at generating nontraditional configurations of common structures to make best use of material and space.

A metal PBF AM machine can offer a greater material choice for production. Where once a production run is complete using titanium, the machine can be reconfigured to manufacture different parts using nickel alloys, copper, steels, aluminum, etc. The material choices are not infinite however and at present for quality purposes are largely kept to weldable alloys. It is possible through precise process control to manipulate the micro structure for desirable material properties. Additive manufacturing can also enable the creation of internal passageways with complex curvatures that improve the performance such as integrated cooling ducts like the one shown in Figure 2.12.

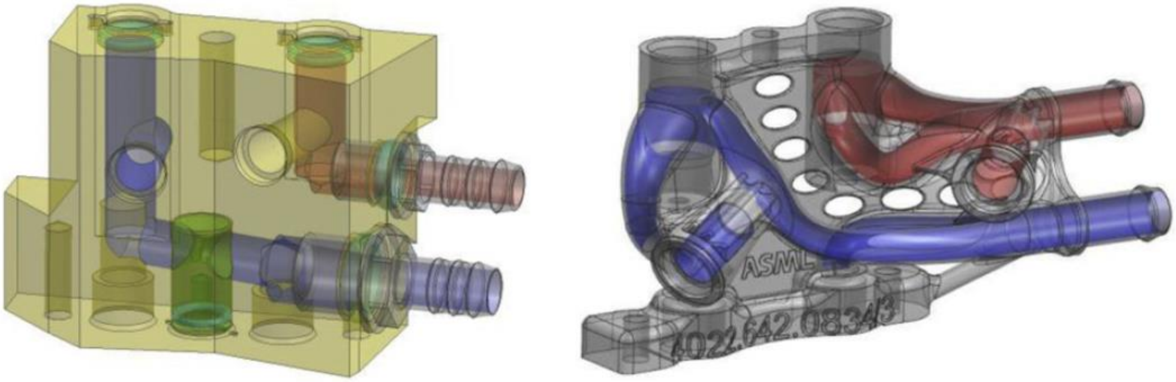

Figure 2.12. Example of a manifold redesigned for additive manufacturing with optimized internal passageways that reduced internal vibration by 90% [13].

Additive manufacturing enables such complexity with design that even traditional CAD tools are not efficient at designing some features that additive machines are easily capable of. While Lattices, trusses, and periodic structures require new software tools to design these features, they can be very beneficial at light weighting components to improve performance. Software programs like nTopology and Materialise Magics enable the designer to easily create these complex features with ease, and fine tune them to fit a specific purpose. During the additive process there are forces that a component may experience such as gravitational forces and internal forces from thermal and residual stress. These forces can be accounted for in the design process through designing a structure to be self-supporting, proper part orientation within the build chamber, and by adding support features. How a part is supported within a build is called the ‘support strategy,’ and is often process specific between materials and also machines.

The support strategies used for laser PBF are different from EBM largely due to the significantly elevated build temperatures (600°C for Titanium) enabled by the electron beam heat source. As described by Körner, C. [5], EBM allows for the application of innovative melting strategies with low levels of residual stresses in high performance materials like titanium. Due to stress-relief annealing at the elevated chamber temperatures, topology optimized structures do not need to be as concerned about build direction so long as sufficient thermal supports are provided on negative (downward facing) surfaces. Many of the various defects that can arise in laser and electron beam additive manufacturing processes have been characterized, where most defects are the result of too much or insufficient application of heat [1,17-20].

2.3 TOPOLOGY OPTIMIZATION

Design of aerospace structures typically requires the lowest weight and highest performing parts, since overall weight of the vehicle drives significant operating costs and reductions in efficiency. Over time the performance improvement and weight reduction requirements have increased, and along with the availability of computing power, has driven the adoption of FEM based sizing and shape optimization. Over the past decades, topology optimization for theoretical studies that go back to Bendsøe and Kikuchi [21] have been continuously developed and improved for practical applications. Topology optimization, has become one of the most promising techniques in the design of aerospace structures by showing engineers how material can be best distributed according to the load paths. The intent is to determine the optimal configuration of a structure provided a design space (domain) and specified constraints, objectives, and boundary conditions. A simple two-dimensional example showing compliance design given a constraint volume is displayed in Figure 2.13

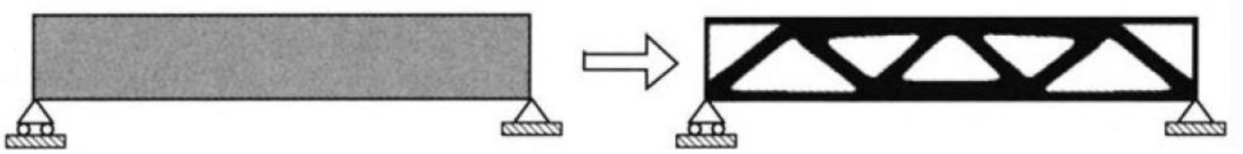

Figure 2.13. Example of a 2D structural topology optimization for a simple bridge [22].

The design freedom made possible with additive manufacturing PBF makes it an ideal application for topology optimization. In the past, topology optimization had to be setup by a stress analyst and ‘interpreted’ by a designer who had to make sacrifices in the design to ensure manufacturability. In aerospace it was largely used to determine the placement and thickness of webs and stiffeners over surfaces that were either milled or assembled. An improvement to stiffener layout came by introducing casting constraints to the topology optimization where the material distribution has to meet certain criteria along a specified direction to comply with manufacturing requirements as shown in Figure 2.14. This type of directional constraint is now more commonly known as a shape control and can be applied for additive manufacturing to prescribe a particular build direction. With additive manufacturing the topology optimized shape can largely be maintained. Where some interpretation of the results is still required, the end product weight and structural properties are much closer to the generated optimized geometry.

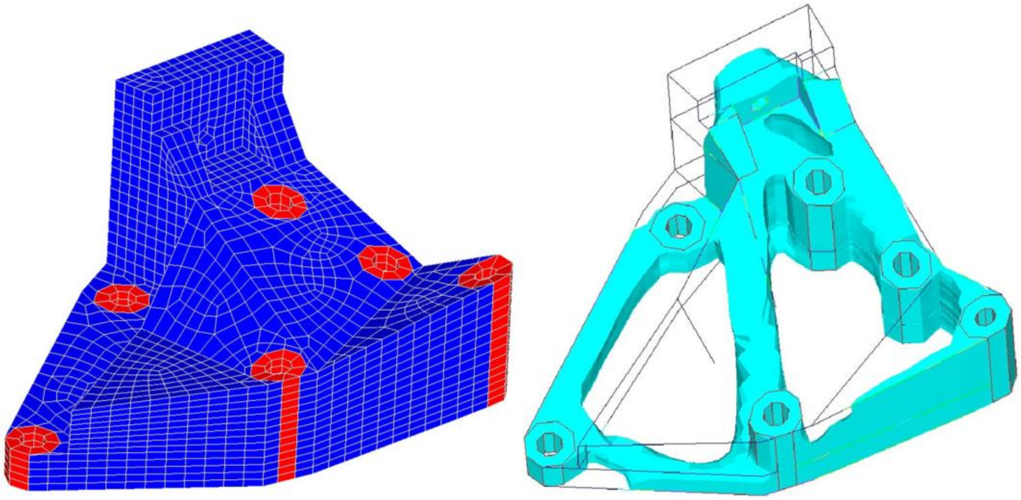

Figure 2.14. Engine bracket topology optimization utilizing a casting constraint [15].

Commercial aircraft engine pylons are traditionally tapered cantilevered box beam assemblies built up from numerous bulkheads, frames, webs, and chords. Since the engines also drive the electric, pneumatic, hydraulic, oil, and fuel systems for the airplane, a particular problem is that numerous additional holes have to be cut from the structure to facilitate the routing of these systems. This drives additional thickness, i.e. weight, into the structural components. By contrast topology optimized engine pylons appear to be rather porous and truss-like, which would ease the routing of systems without weakening the structure. In the case study from Altair Engineering and SOGECLAIR Aerospace [23], topology optimization was utilized to redesign an engine pylon structure. The new structure was reported to be 20% lighter and contain 97% fewer components while maintaining similar strength to the conventional design. It is the reduction of detailed parts that provides better durability, and thus the reduction of engineering drawings that provides a decrease in overall cost. Similarly, Remouchamps et. al. [24] designed a topology optimized aircraft pylon using a bi-level scheme with resulting geometry shown in Figure 2.15. The first level optimized the global geometric parameters that impacted drag and weight of the structure, while the second optimized for weight based on the first level constraints. However, the manufacturing of the structure was not considered.

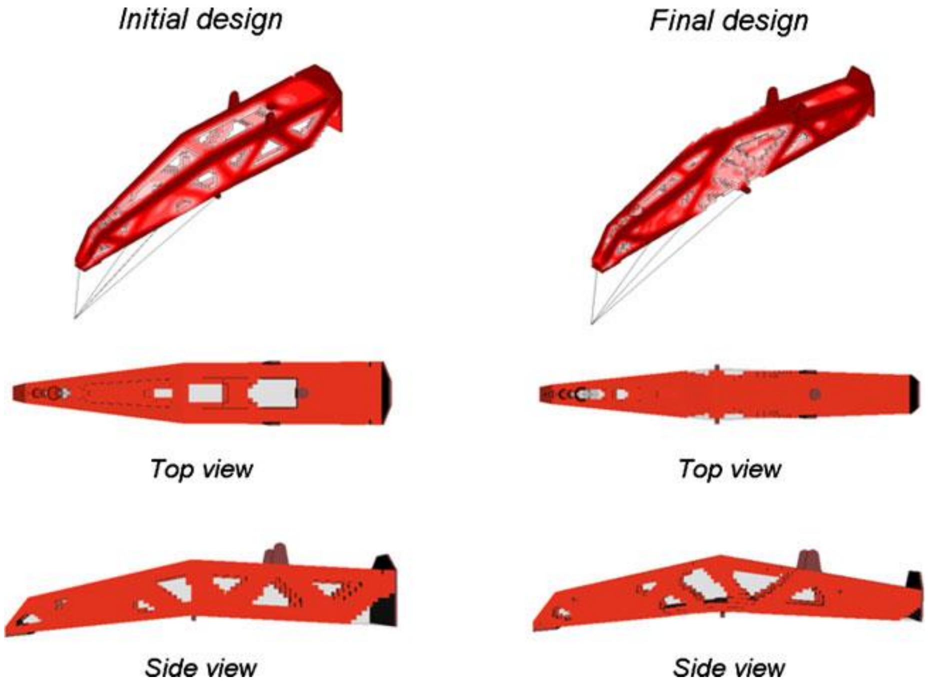

Figure 2.15. Initial and final designs of a commercial aircraft engine pylon using a bi-level scheme [24].

While PBF additive manufacturing provides more design freedom, there are still limitations that must be considered for a design to be producible. One of the key elements of this process are support features, sacrificial melted material that performs a structural and/or thermal function to enable the geometry above it to be fabricated. Insufficient supporting features can result in unwanted distortion and cracking of the end part, but they must be as minimal as possible because removing them in post-processing increases the cost of manufacturing. Leary et. al. [16] utilized topology optimization to create an optimal support-free additive structure. This used an algorithm to identify in two dimensions design features, such as overhangs, that were at risk of not being able to be produced, and then modified the geometry of the structure to reduce the risk of build failure. Where that was tested using polymer fused filament fabrication (FFF), Smith et. al. [4]

looked at the dimensional accuracy of weight optimized truss structures using EBM. They showed that truss members not aligned with the build direction required sufficient thermal supports to manage the heat in order to yield dimensionally accurate parts. There are some commercially available algorithms that attempt to make use of overhang constraints for additive manufacturing, but they often fall short for complex problems or properly take thermal management into account. The burden still largely remains with the design engineer to ensure the structure is capable and producible.

2.4 GEOMETRY VARIATION AND DEFECTS

It is often difficult to identify the cause of any particular defect post-build since one type of defect can be the result of another. One defect can change the localized heat transfer conditions which leads to compounding defects. An example of this would be that the formation of a pore or multiple pores reduces the thermal conductivity of the underlying material, creating unexpected thermal resistance and causing swelling or balling of the layers above. It is therefore important to understand all the different defects that can occur and learn how to identify them [1,3,9].

While the EBM process obviously involves melting of the top layer, the beam is also responsible for the remelting of underlying layers which produces a thermal cycling as the material heats and cools. Unlike the SLM processes that have build chamber temperatures close to room temperature or slightly above, Figure 2.16 shows that EBM operates at much higher temperatures, dependent upon the material, due to the preheating and therefore has a unique thermal history. Since it can then take many more hours or days for the build volume to cool once the build is complete, hold time and hold temperature can impact the material properties by essentially aging the metal parts longer than standard industry processes [1,9-10].

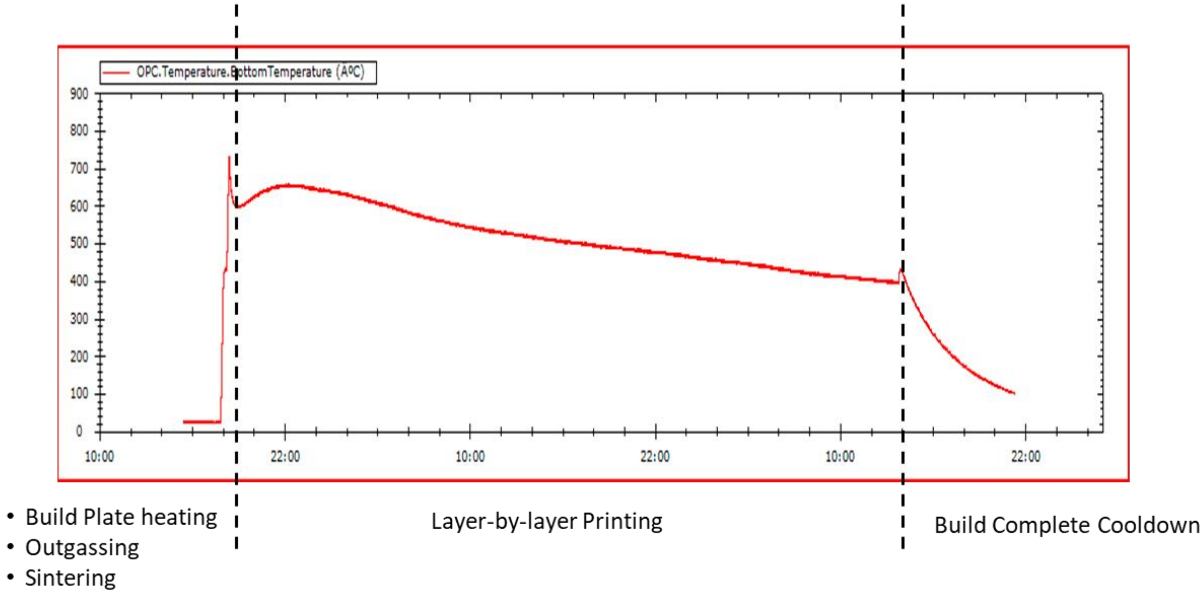

Figure 2.16. Thermal history of EBM process for a sample build using Ti-6Al-4V as measured by the thermocouple under the build plate.

Inspection methods for EBM parts can include 3D laser scan, X-ray, computed tomography, optical microscopy, scanning electron microscopy, and synchrotron radiation micro-tomography. Some of these methods try to capture the surface characteristics while others try to capture the internal porosity. Inspecting the final metal grain morphology, texture, or phase, is typically accomplished with either a light optical microscope, scanning electron microscope, electron backscatter diffraction, x-ray diffraction, or a combination of methods [1,9-11].

2.4.1 *Dimensional Accuracy*

Three-dimensional laser scans of the as built surface can measure geometric accuracy of the EBM process when compared to the original part model. Dimensional accuracy is important to the final part, especially if it was designed with minimal mass topology optimization that has little to no redundant material. The EBM process does not fabricate overhanging (downward facing) surfaces with respect to the build direction as well as other upward facing or side surfaces. When there is no previously melted material underneath such as a portion of the part or support features, the newly melted area has a tendency to distort upwards. This can cause powder in the next layer to not be properly distributed in that area or immediately adjacent and the problem compounds. The inaccuracy of overhanging surfaces can be mitigated by decreasing the beam energy density in the vicinity of overhanging surfaces [4]. The process parameters to adjust would be to increase the hatching scan beam speed and not doing the contour scan as depicted in Figure 2.17; however, this can cause an increase in porosity. The most common mitigating action to achieve dimensional accuracy of overhangs is to include sacrificial support structures under the part melt area to conduct the heat away from the melt region.

Figure 2.17. Contour scan (a) and hatching scan (b) [4].

2.4.2 *Surface Roughness*

Powder bed additive manufacturing processes are known to have poor surface roughness when compared to other manufacturing methods like casting or machining. For now, additively manufactured parts are considered to be near net shape and not final shape due to the poor as-built surface roughness. The surface roughness stems from the scan strategy which includes the beam power and contouring. When the edge surface of the part is melted, unmelted or partially melted powder immediately adjacent to the melt pool becomes sintered and referred to as satellites. The final roughness can be influenced by the powder particle size where finer powder means smaller satellites and a smoother overall surface. The roughness of an EBM part can be difficult to characterize with standard equipment used in other manufacturing processes. This is because the surface is so irregular from peak to valley and can also contain caves and overhangs as can be seen in Figure 2.18 that simply calculating average roughness (Ra) may not adequately describe it [2,6,11].

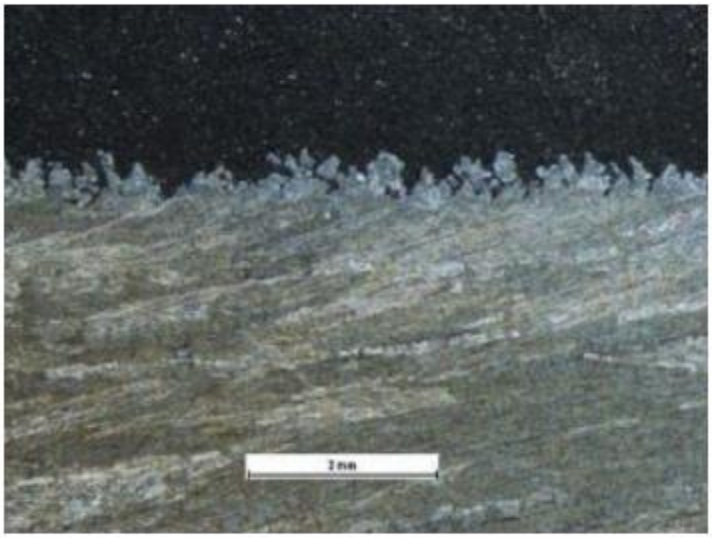

Figure 2.18. Typical EBM surface condition of a part cross section [12].

2.4.3 *Porosity*

Powder bed fusion additive parts will contain very small internal pores, or voids in the material that can decrease the strength of the final part and it is a common defect. With optimized parameters it is possible for porosity to be less than 1% for EBM built parts. The pores are microscopic (<100 μm) and difficult to detect without expensive equipment like micro computed tomography (CT). Porosity can originate in PBF EBM parts as effects of the build parameters, the scan strategy, the part feature orientations, or even the powder itself. Once porosity is found, answering the question of what was the cause is very difficult or impossible because there are so many potential sources to control. As shown in Figure 2.19, *gas induced* porosity can typically be identified by having a spherical shape, *process induced* pores form either when the applied energy is not adequate for complete melting or spatter ejection occurs and creates irregularly shaped pores [1,6-7].

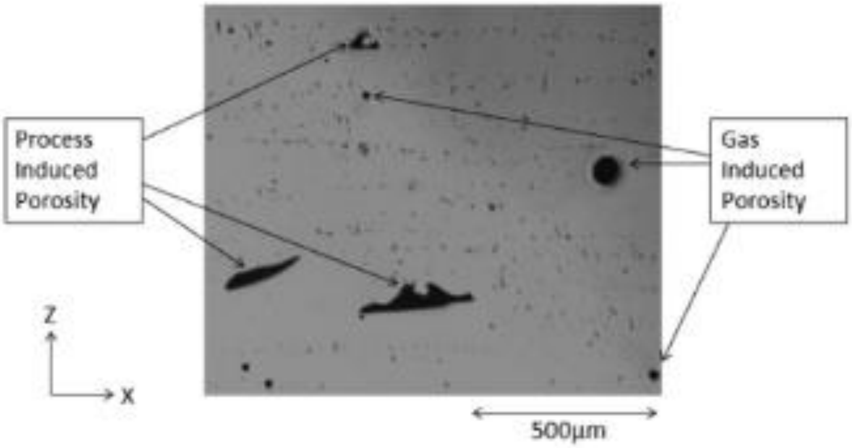

Figure 2.19. Comparison of entrapped gas induced porosity transferred from powder feedstock and process induced lack of fusion porosity from light optical microscopy [1].

Keyhole formation is the spatter ejection of molten material when too high of power is applied that raises the temperature of the melt as high as the boiling point and can leave a trail of voids along the scan direction. *Balling* as seen in Figure 2.20 is when large amounts of material solidifies into spheres rather than solid layers due to surface tension forces [7]. It can gather up into a heap greater than the distance between the build surface and the rake or recoater arm. This leads to significant interactions between molten material at the build surface and the rake, or recoater, which will eventually lead to build failure. *Lack of fusion* can occur when not enough power is applied to an area of powder. These regions can be identified by un-melted powder near a pore. Since the powder can contain particles larger than the layer thickness it is the intention that when melted the material will consolidate into the correct layer height; however, *shrinkage porosity* also known as hot tearing occurs when there is incomplete flow of material into the desired melt region [1].

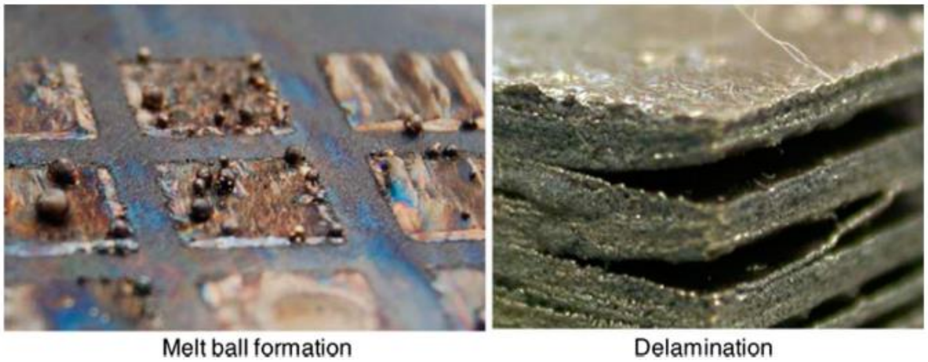

Figure 2.20. Example of balling (left), and delamination (right) [7].

Gas induced porosity is a problem that originates with the way the powder feedstock is produced. The most common method since it is relatively inexpensive is called gas atomization (GA). This is where molten metal material is poured into a tall chamber where it is hit with a high velocity inert gas like argon or nitrogen. Molten particles get blasted away and solidify as they fall to the bottom of the chamber. When the material is hit with the gas, it sometimes surrounds the gas as a shell such that under scanning electron microscopy (SEM) the powder appears solid; however, when sectioned in Figure 2.21 the pore is encased inside the metal powder particle. Therefore, even if all machine parameters were tightly controlled such that process induced porosity was essentially zero, the feedstock material could still be a source of porosity. Metal powder can be produced through other methods like the plasma rotating electrode process (PREP) which is known for high quality feedstock powder with no gas induced porosity [1,5-6].

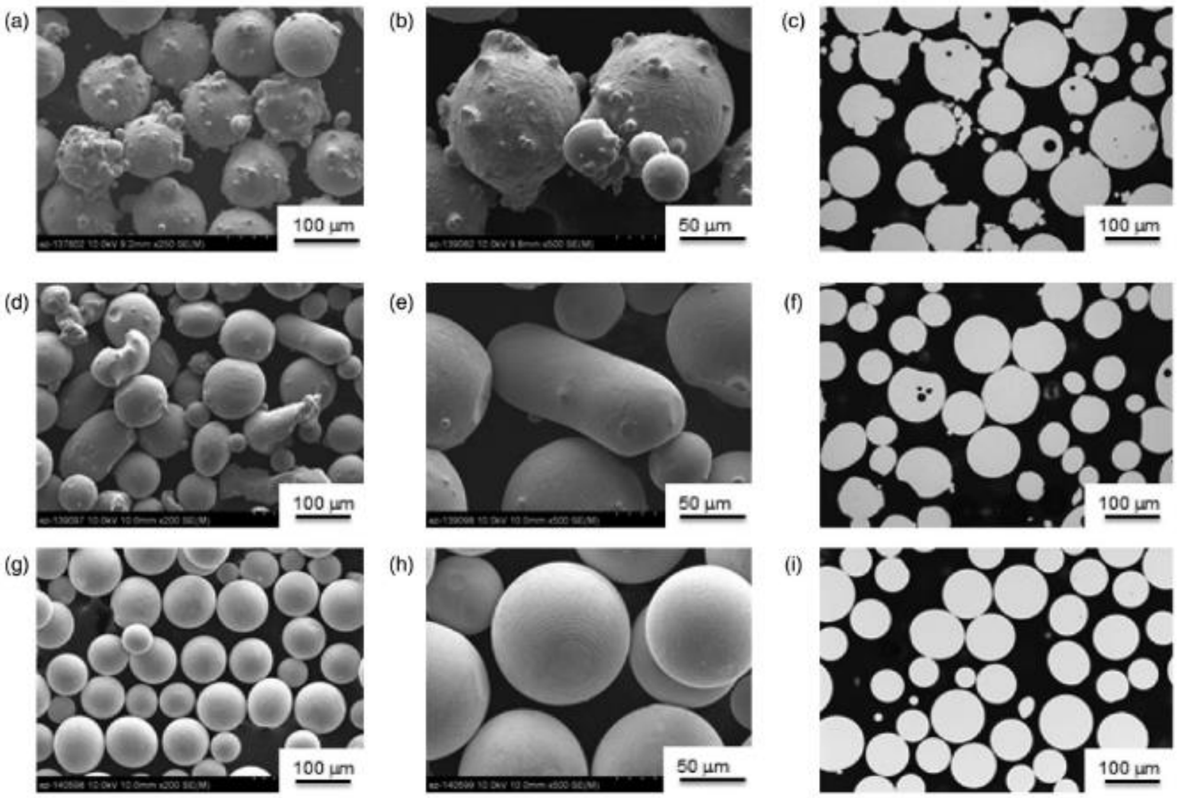

Figure 2.21. Gas Atomized powder (a, b, c), Plasma atomized powder (d, e, f), PREP atomized powder (g, h, f) [1].

2.4.4 *Residual Stress*

Residual stress is a stress within a material that remains even after removing applied stresses. Defect formation is dependent upon the residual stress in the material that comes from the melting and remelting process at high temperatures so it is common in metal AM materials. Residual stress can act as a driver for changes in the grain structure as well as negatively impact the material mechanical properties. Plastic deformation or warping may occur if the residual stress happens to exceed the local material yield stress, and cracking or other defects may result if that stress exceeds the local material ultimate tensile stress [6,9].

Large macroscopic cracks in the material, like those in Figure 2.22, can be related to problems with porosity, or interlayer cracking known as *delamination*, *swelling*, or *melt balling*. Microstructure cracking is material dependent such that in some cases it may be unavoidable, and it can occur during subsequent heating or solidification processes. *Solidification cracking* can come from applying too much energy where stress is induced between areas of the melt pool that have solidified and areas that have yet to solidify. Higher energy leads to higher thermal gradients and subsequent cracking ensues. *Grain boundary cracking* can also occur which depends on the grain boundary morphology and the formation or dissolution of precipitate phases [1,6-7,9].

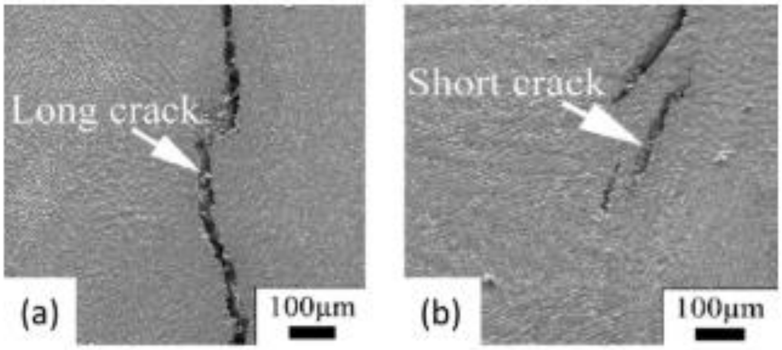

Figure 2.22. Long and short cracks caused by residual stresses in additive manufacturing process [6].

An example of swelling can be seen in Figure 2.23 where the solid material rises above the build plane where powder is distributed and melting occurs. Since EBM is essentially micro welding, the swelling can be seen as a hump forming similar to the humping observed in welding. This occurs due to the melt pool geometry and its effects on the surface tension of the material. Capillary and wetting forces have been identified as contributing to swelling, as well as balling. Like balling, the swelling can cause undesirable rake contact that leads to poor powder distribution and eventual build failure [6-7,9].

Figure 2.23. Region of a completed part that had undergone swelling [9].

Another defect that can have similar effects to swelling is the warping of the build plate. An EBM process uses a metal plate under which the build chamber thermocouple is placed. This build plate may warp during the build at the elevated build chamber temperatures as a form of stress relief that results in permanent plastic deformation. The distortion can push the build material up similar to swelling and cause contact with the rake or distort the part geometry out of the desired shape causing issues with dimensional accuracy [1].

Chapter 3. MATERIALS, METHODS, AND PROCEDURES

The materials addressed in this work are primarily the titanium alloy Ti-6Al-4V since that is what was used for all of the included experiments. The method of manufacture and largely discussed is EBM, however some comparisons are made to SLM since both are PBF additive processes. The procedures for manufacture were all the same which followed the Arcam A2X manual step by step. Post processing was carried out using the Arcam Powder Recovery System (PRS) while any supports were removed using manual cutters. Two metrology systems were employed depending on the size of the specimens. Small specimens that fit on the imaging tray were measured using a Keyence VR-3100. Large specimens had to be professionally 3D laser scanned. In order to become familiar with the materials, methods, and procedures, a rocket motor component build was performed as a case study in this chapter

3.1 MATERIALS

In general, the material feedstock required for the powder bed fusion additive process must be in powder form and electrically conductive. Naturally many metal alloys can meet this requirement so there is a lot of opportunity for new materials research. It is generally accepted that any alloy that is weldable can be used for the EBM or SLM process, so steels, titanium, and aluminum alloys are among the most common used for metal additive manufacturing. The powder composition of the feedstock is very important to the chemistry and material properties of the end parts since the pick-up of oxygen or the vaporization of metal has to be accounted for. Despite the newness of the EBM and SLM additive manufacturing process, powder metallurgy has been around for a lot longer and the processes for making the powder feedstock are well established. Powders are either pre-alloyed made from melting and atomizing other feedstock like ingot or bar Ti-6AL-4V, or blended mixtures of elemental powders that when melted together form the final alloy.

3.1.1 *Morphology*

Metal powder production is an established industry for other powder metallurgical manufacturing processes. This is a benefit for the development of additive manufacturing PBF processes since producers operate to set standards; however, due to the particular nature of AM those standards may need to be more well controlled. Different production methods can result in different powder characteristics such as morphology, size, and chemical composition. The powder feedstock is most commonly produced through some variation of atomization with the goal of producing highly spherical solid particles [6]. The sphereoidocity is desired to facilitate smooth particle flow in the machine for even layer distribution and homogeneous packing density characteristics. In experiments involving EBM, the stock material was typically gas atomized Ti-6Al-4V (some cases ELI) powder provided by the machine manufacturer, Arcam. The typical powder particle diameter ranges from 45-105 μm with an average around 75 μm and ASTM F3001 lays out the chemistry requirements of the powder. Those particle diameters are nearly double the size of those used in SLM processes with an average size around 36 μm which also contributes to the smoother surface roughness. Figure 3.1 shows a powder size distribution and SEM images of the different process powders [18].

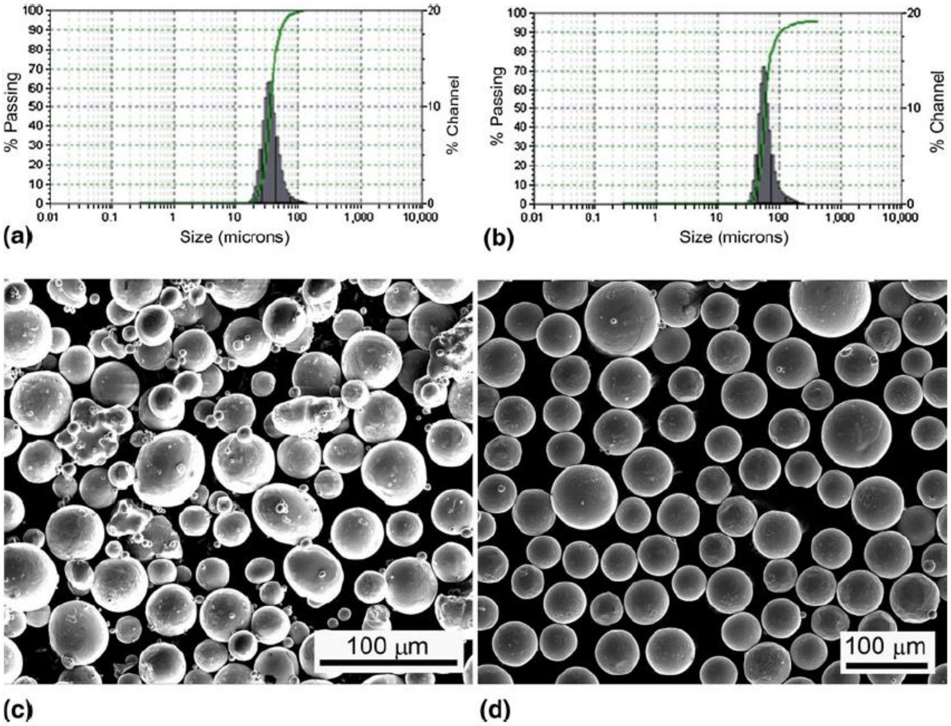

Figure 3.1. Powder size distribution and SEM of EOS supplied SLM Powder (a,c), and powder size distribution and SEM of Arcam supplied EBM Powder (b,d) [18].

3.1.2 *Microstructure*

The typical microstructure of additively manufactured EBM parts consists of dominate prior β columnar grains with a high amount of grain oriented vertically along the Z axis (build direction) with α + β lamellar structure (mainly Windmanstätten, or "basket weave") inside the β grains and organized into discrete groups of α lamellae with similar thicknesses as shown in Figure 3.2 [19]. This is because the scan strategy influences the melt pool geometry and flow of heat through the melt pool [2]. Due to the high processing temperature maintained in the chamber martensite is not present. The identification of grain boundaries is difficult which makes quantifying the size of the columnar grains impossible; although, an α layer with an average thickness of 2 μm marked some of the prior β grain boundaries.

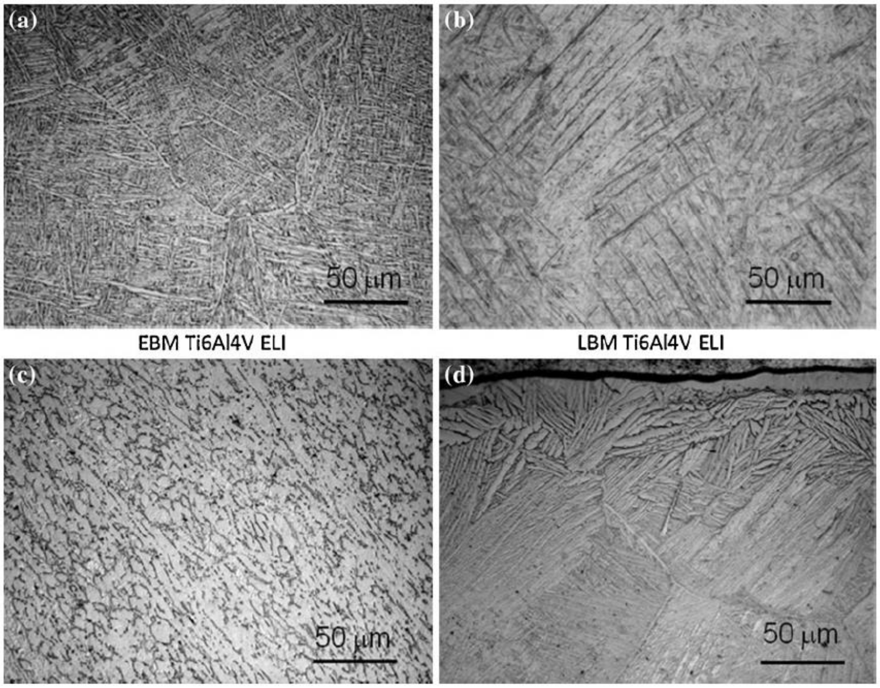

Figure 3.2. Optical micrographs of typical Ti-6Al-4V microstructure in a) EBM material, b) SLM material, c) rolled material, and d) cast material [25].

The XY plane scan layers are visible under low magnification with an average thickness measuring 50 μm, which matches the default layer thickness process parameter [19]. A clear distinction can be made between microstructures from the contour scan which produces an equiaxed fine grained structure, while the hatching scan produces a highly oriented structure [3]. Process parameters for EBM affect both the matrix solidification grain structure and precipitate evolution such that optimizing one may compromise the other. It may be possible to in-situ age material with the EBM process since solidification structures are affected by subsequent heating and holding at elevated temperature [6]. The SLM microstructure while comparable consists primarily of α or α’ (martensite) because of the overall lower heat from the build process, however the fine acicular morphology makes it difficult to distinguish between the two phases since they have a similar crystalline structure [19].

Post process β annealed EBM Ti-6Al-4V microstructure is described as α + β lamellar with large defined groups of aligned α plates in prior β equiaxed grains and coarse α layers at the grain boundaries. The morphology of the as-fabricated columnar β grains are changed to equiaxed because the annealing takes place above the β transus temperature. A slow cooling furnace produces a lot of coarse microstructure, and the whole process eliminates the as-fabricated directionality to produce an equiaxed structure. Therefore, in a β annealed condition EBM Ti-6Al-4V is expected to have isotropic properties. In the case of a post process HIP treatment of SLM and EBM materials, the lamellar microstructure shows significant coarsening in Figure 3.3.

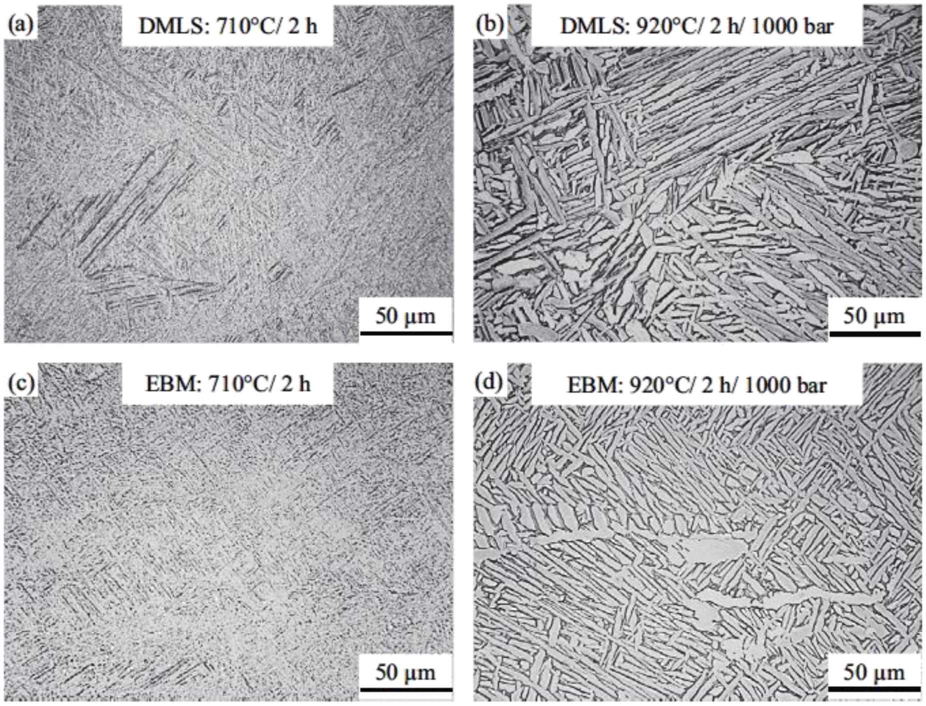

Figure 3.3. Microstructure of AM Ti-6Al-4V: a) SLM annealed, b) SLM HIP, c) EBM annealed, and d) EBM HIP [26].

3.1.3 *Mechanical Properties - Static*

Figure 3.4 shows a comparison of static tensile properties between EBM and SLM in the as-fabricated and post heat treatment states alongside cast, forged, and wrought annealed Ti-6Al-4V. Static tensile properties for SLM as-fabricated with annealing provides a yield strength (YS) of 1017 MPa and an ultimate tensile strength (UTS) of 1096 MPa. Milling the specimen to remove the poor as-built surface roughness increases the YS and UTS to 1086 MPa and 1165 MPa respectively. After HIP the as-fabricated YS and UTS were lower than the annealed at 837 MPa and 949 MPa respectively, while removing the surface roughness with milling improved the HIP condition YS to 894 MPa and UTS to 997 MPa. The martensitic microstructure of as-fabricated SLM Ti-6Al-4V provides high strength, but low ductility so the samples fail at low strain values. Though that can be improved with heat treatment.

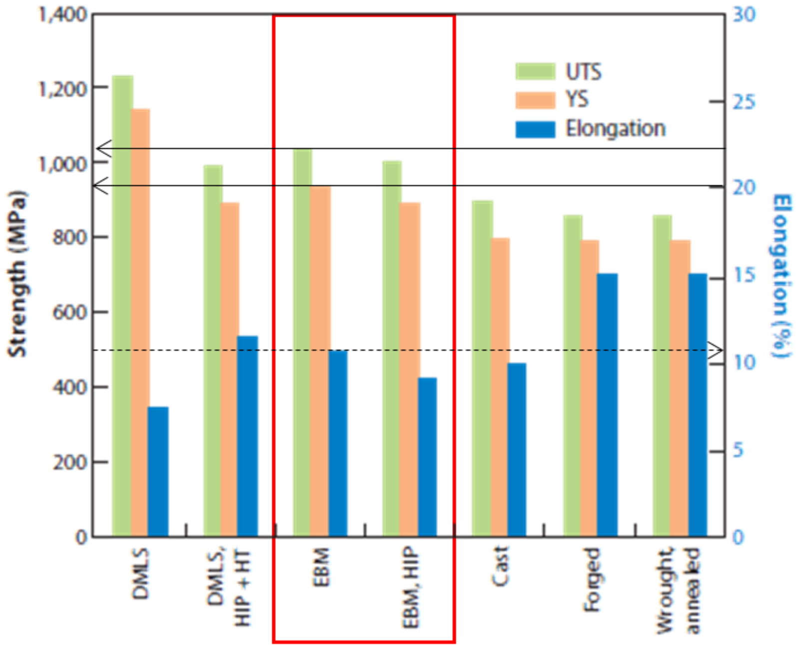

Figure 3.4. Tensile properties for EBM and SLM as-fabricated and after heat treatment compared with cast, forged, and wrought [27].

The EBM Ti-6Al-4V static properties in general are lower than the SLM values stated above. The higher EBM process temperatures tend to decrease static property performance while increasing the elongation. Annealed as-fabricated showed a YS and UTS of 869 MPa and 965 MPa, but a marked difference from the SLM is that milling away the rough surface showed no significant improvement as the YS was 868 MPA and the UTS was 975 MPa. As with the SLM samples, the HIP condition static values were all lower than the annealed condition. As-fabricated the YS and UTS were 718 MPa and 833 MPa, while milling did show some improvement with a YS of 774 MPa and UTS of 896.

Hardness testing on EBM Ti-6Al-4V specimens has been carried out using a Buehler microindentation (Vickers) hardness tester with a 25g force and 10 second dwell time as well as a Rockwell C hardness (HRC) test using a 1.5 kN load. The as-deposited hardness values were comparable to the wrought coarse α and equiaxed α/β. SLM processed material was harder than material processed via EBM [28].

3.1.4 *Mechanical Properties - Cyclic*

Fatigue behavior is difficult to characterize since it is so heavily influenced by the microstructure caused by the processing conditions. With Ti-6Al-4V, the volume fraction and morphology of the α and β elements changes and the structures can exist as lamellar α and β, martensitic α’, bi-modal, and equiaxed. The fatigue performance based on S-N curves shows that the fatigue limit of the SLM process outperformed the EBM process by a significant amount, 550 MPa versus 340 MPa respectively [18-19]. Like the static properties, the martensitic phase also improves the fatigue strength by impeding dislocation motion, though that also results in a smaller plastic strain. The poorer fatigue strength of EBM processed material could be ascribed more to the lamellar microstructure as opposed to the presence of internal porosity [19].

Testing for fatigue crack growth is performed at various stress ratios ranging from 0.1 to 0.8 and start at an initial stress intensity factor K that would provide a consistent crack growth rate. This is followed by load shedding to ascertain the true fatigue threshold ΔK_{th} per ATSM E647. A procedure was introduced in the ASTM-E647 standard to account for closure effects on fatigue crack growth [28]. The method describes using load displacement data to determine the crack opening load while under cyclic loading. Within a defined degree of accuracy, the technique distinguishes the upper linear segment of the load-displacement curve. This was determined to be the range for the effective stress intensity [19]. At the crack growth rate prescribed by ASTM E647 standard to achieve ΔK_{th}, the experiment often requires 5-7 days of machine time to construct a full curve [29].

Recall that the Z direction is considered to be the vertical build direction and perpendicular to the build plane, while the X and Y directions are horizontal and parallel to the build plane. The horizontal and vertical descriptions are also the crack propagation directions. In the as-built condition, it has been observed in testing that for all stress ratios, the vertical crack propagation direction has a higher delta K threshold (ΔK_{th}) than the horizontal direction [19]. The closure effects in the horizonal orientation are lower, which indicates that when compared to the vertical direction, the horizontal roughness-induced closure for the crack propagation is lower. For annealed EBM Ti-6Al-4V, due to its equiaxed grain structure, isotropic properties were observed and there was no significant difference in ΔK_{th} for the vertical and horizon crack propagation directions. The similar crack propagation behavior between vertical and horizontal build directions also led to similar effects of closure. At low stress ratios the β annealed EBM closure effects are higher than the as-built, however at higher stress ratios the closure ratios are comparable [19,28].

Overall annealing EBM Ti-6Al-4V to obtain a coarse lamellar structure can yield a significant improvement in resisting fatigue crack growth regardless of stress ratio or growth stage. When approaching ΔK_{th} lamellar microstructures have three primary factors that influence the resistance to fatigue crack growth: crack tip geometry, material properties, and crack closure. The crack closure effect controls the crack growth behavior at lower stress ratios while the crack tip geometry effect dominates at higher stress ratios. β annealing EBM Ti-6Al-4V grows larger α colonies in the material from the finer size in the prior as-built condition. All three factors depend on the size of the α colonies in the material, and so as the colony size increases so does the influence of the crack tip geometry and the closure effects, which in early stages raises the material's resistance to crack growth. Typically, a material's resistance to crack growth (i.e. ductility) will decrease when the α colony size increases, however this effect is outweighed by the effects of the closure and crack tip geometry [19].

To further explain how the resistance of crack growth in annealed Ti-6Al-4V increases at higher stress ratios, it is necessary to consider how it relates to the crack tip geometry. If two adjacent areas in front of the crack have different crystallographic orientations, then that can cause the crack to shift out of the expected plane of propagation and into the direction of different slip planes determined by the adjacent colonies as depicted in Figure 3.5 (a). This mechanism bifurcates the crack tip into the adjacent areas that will be separated by some distance that is perpendicular to the primary propagation path. Figure 3.5 (b) shows the crack profile in β annealed EBM Ti-6Al-4V is rough with visible bifurcations caused by large α colonies oriented unfavorably to crack propagation. If the load axis is parallel to the lamellae long axes, then the crack will cut straight through the lamellae structure, but if the load axis is perpendicular to the lamellae then the crack will grow along the lamellae boundaries [19].

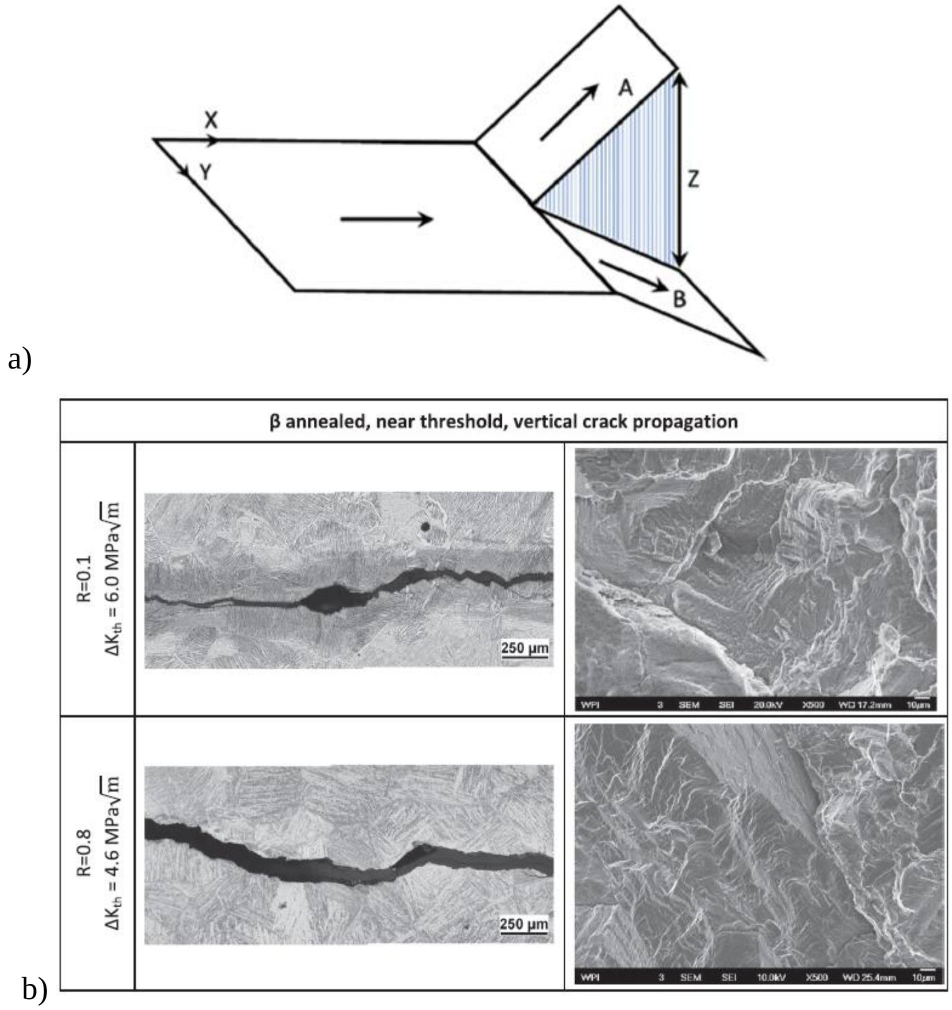

Figure 3.5. Crack tip schematic where adjacent colonies A and B have different crystallographic orientations (a) and Crack path and facture surface of β annealed EBM Ti-6Al-4V for stress rations R = 0.1 and R = 0.8 (b) [19].

By comparison for as-fabricated EBM Ti-6Al-4V the α lath orientation in the "basket weave" can affect the crack direction if the orientation is similar to the crack growth direction. This results in smoother crack profiles since the bifurcation steps are smaller. With the as-fabricated horizontal direction, the crack propagation is perpendicular to the columnar grains and parallel to the scan layers. The opposite is true for the as-fabricated vertical where the crack propagates parallel to the grain boundaries and perpendicular to the scan layers. The scan layers promote crack deflection which boosts the tortuous nature or large-scale meandering of the crack path; while columnar grain structures control the crack branching which is where two or more crack tips will advance simultaneously, or the crack splits. Grain boundaries and colonies are difficult to identify due to the fine microstructure, even under higher magnifications it is challenging to detect the fracture mode and how crack interacts with the microstructure. Despite the differences in microstructure between EBM and SLM Ti-6Al-4V, like the presence of α’ martensite in SLM, crack growth rates are also lower in the crack propagation direction parallel to the columnar grains [19,26,28].

The resistance to crack growth after a post process HIP treatment was found to be higher for SLM (4.4 MPa√m) and EBM (4.8 MPa√m) Ti-6Al-4V materials when compared to annealed material (SLM: 3.2 MPa√m, EBM: 4.2 MPa√m). Within the Paris regime however similar crack propagation was observed which behaved independent of additive manufacturing process or heat treatment. At higher stress ratios where the roughness-induced closure has less of an effect, the crack growth is within the threshold regime and similar to results determined at lower stress ratios (SLM: 2.0 MPa√m, EBM: 2.9 MPa√m). Figure 3.6 shows a comparison of the fatigue crack growth properties of SLM and EBM Ti-6Al-4V in the as-built, annealed, and HIP condition [26].

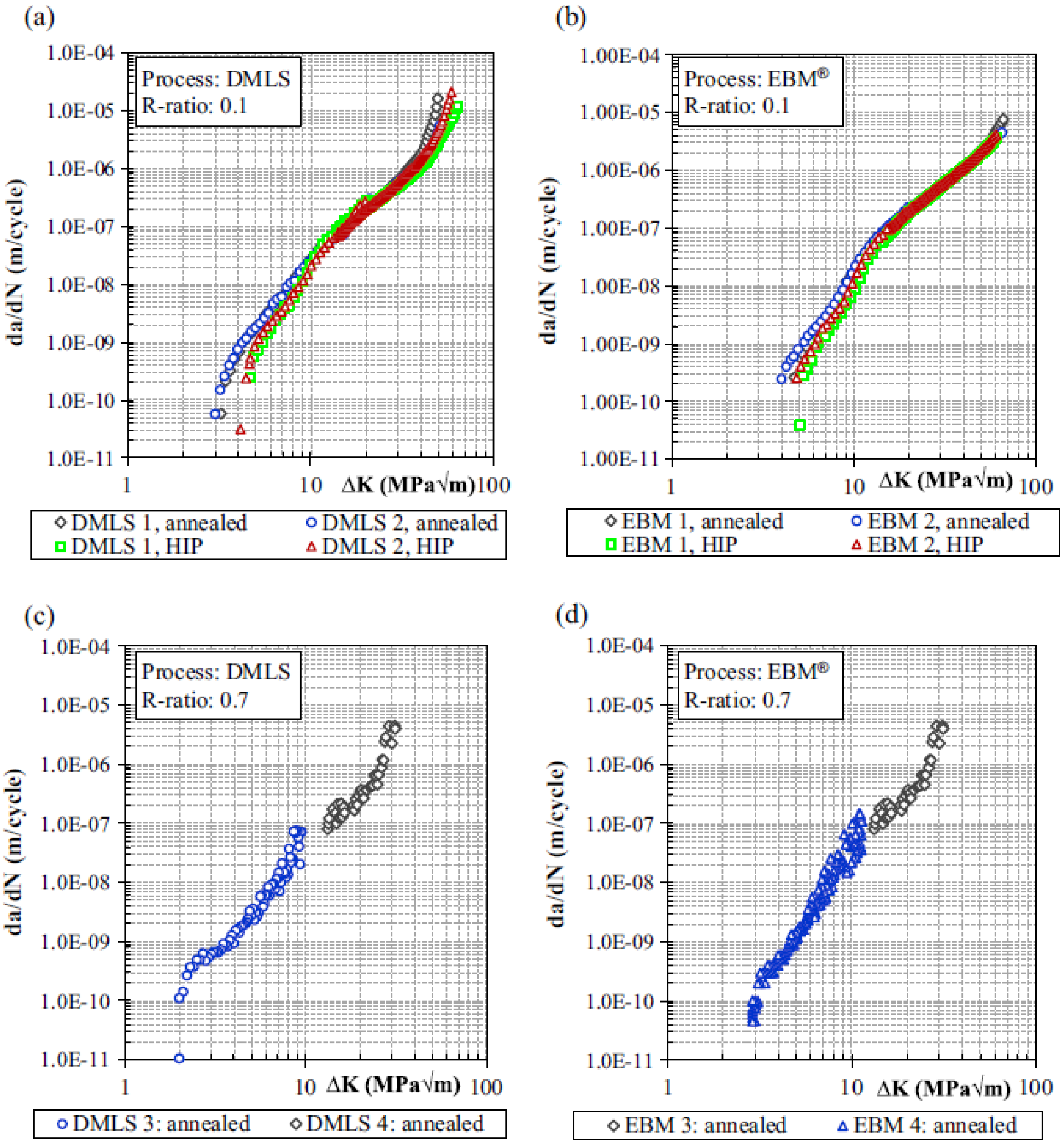

Figure 3.6. Fatigue crack growth properties of SLM and EBM Ti-6Al-4V, a) SLM annealed & HIPed R = 0.1, b) EBM annealed and HIPed R = 0.1, c) SLM R = 0.7, and d) EBM R = 0.7 [26].

Under high cycle fatigue conditions, no differences were observed from as-fabricated test specimens that had been annealed compared to HIP even though HIP reduces the size and quantity of internal defects. Fractographic analysis shows that cracks primarily originate from the surface, which then makes sense that SLM specimens with a lower surface roughness showed a higher fatigue limit than EBM by ~50 MPa. Milled specimens however show improved fatigue performance after HIP compared to the annealed condition with less scatter. This is due to microstructure inhomogeneity for the HIP conditioned material, while defects dominate the annealed material. The HIPed SLM Ti-6Al-4V material fracture toughness also shows significant improvement from annealing because the martensitic microstructure is removed and the alloying elements are forcibly dissolved by the HIP process. Consequently, no such improvement is seen in EBM processed Ti-6Al-4V because the higher processing temperature already reduced the martensitic microstructure and dissolved alloying elements [26].

When fatigue properties ΔK_{th} and K_{max} are compared graphically via Figure 3.7 (a), it can be seen that annealed EBM Ti-6Al-4V requires higher ΔK_{th} and K_{max} values for cracks to propagate than either as-fabricated direction. For design optimization purposes without any post processing the vertical crack propagation direction requires higher ΔK_{th} and K_{max} values than the horizontal crack orientation. Physically, this also means that the roughness-induced closure is small if the stress ratio is above the critical value for any condition. A correlation of ΔK_{th} and the stress ratio in Figure 3.7 (b) is useful since one can estimate the threshold behavior at various stress ratios, especially if experimentally there are only a limited number of test specimens available [19].

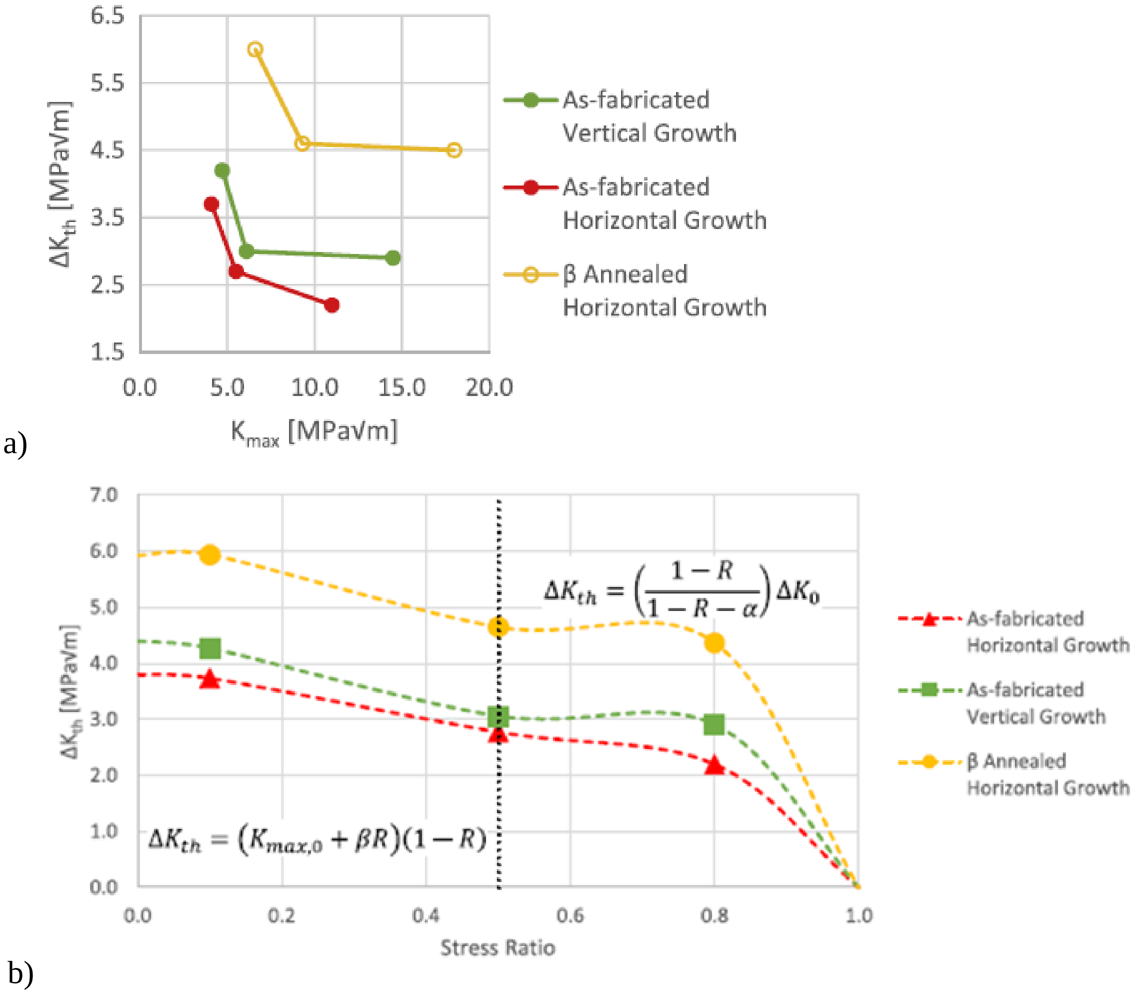

Figure 3.7. ΔK_{th} and K_{max} diagram of EBM Ti-6Al-4V (a), and ΔK_{th} and Stress Ratio correlations for horizontal and vertical crack propagations (b) where α and β are parameters in MPa√m that were determined experimentally and vary based on build direction and post process condition [19].

A few studies have reported fracture toughness even though their samples did not meet the ASTM criteria to ensure plane strain conditions were met. The ASTM F42 committee is actively working to provide updates to orientation designation scheme for fracture toughness and fatigue crack growth. This makes it difficult to compare and come to any conclusions but a summary is shown in Figure 3.8 from the values obtained in Table 3.1 [27]. Despite the scatter it shows that the fracture toughness in as-built SLM ranges from 16 to 86 MPa√m, which is then improved with subsequent post process stress relieve, heat treat, or HIP. For EBM the fracture toughness ranges is higher from 65-110 MPa√m with no improvement after HIP. The EBM Ti-6Al-4V as-fabricated fracture toughness decreases with stress ratio from 56.6 MPa√m to 17.7 MPa√m, and is lower in the vertical direction than in the horizontal by about 14%. These results clearly indicate some degree of anisotropy in the as-built material. EBM Ti-6Al-4V β annealing can increase the fracture toughness by 65%, though it also lowers the yield strength [19].

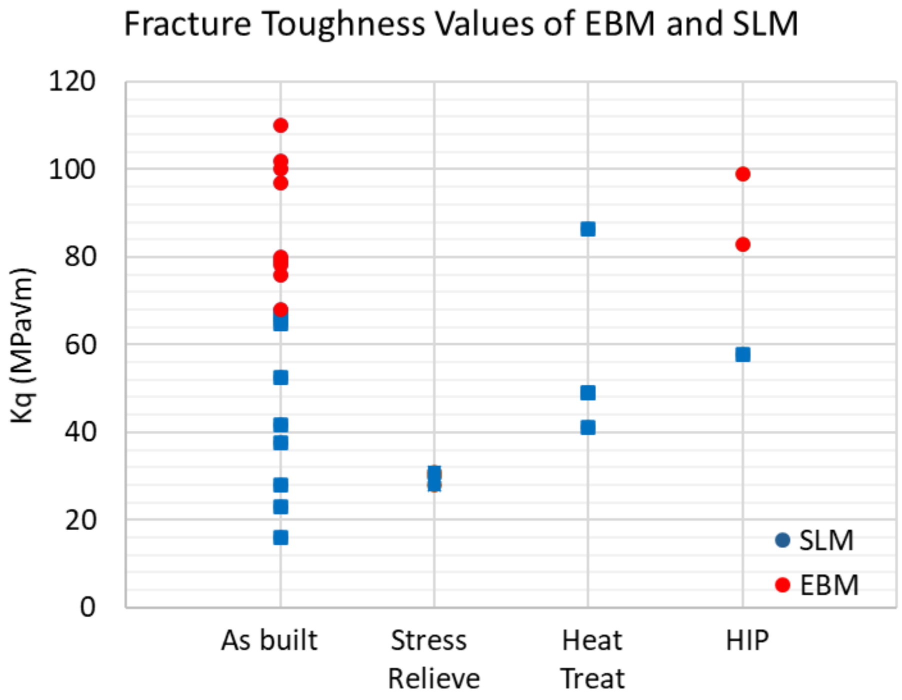

Figure 3.8. Comparison of fracture toughness values of EBM and SLM as reported in Table 3.1 from different machines, process parameters, and specimen orientations.

Table 3.1. Fracture toughness summary of EBM and SLM Ti-6Al-4V [27].

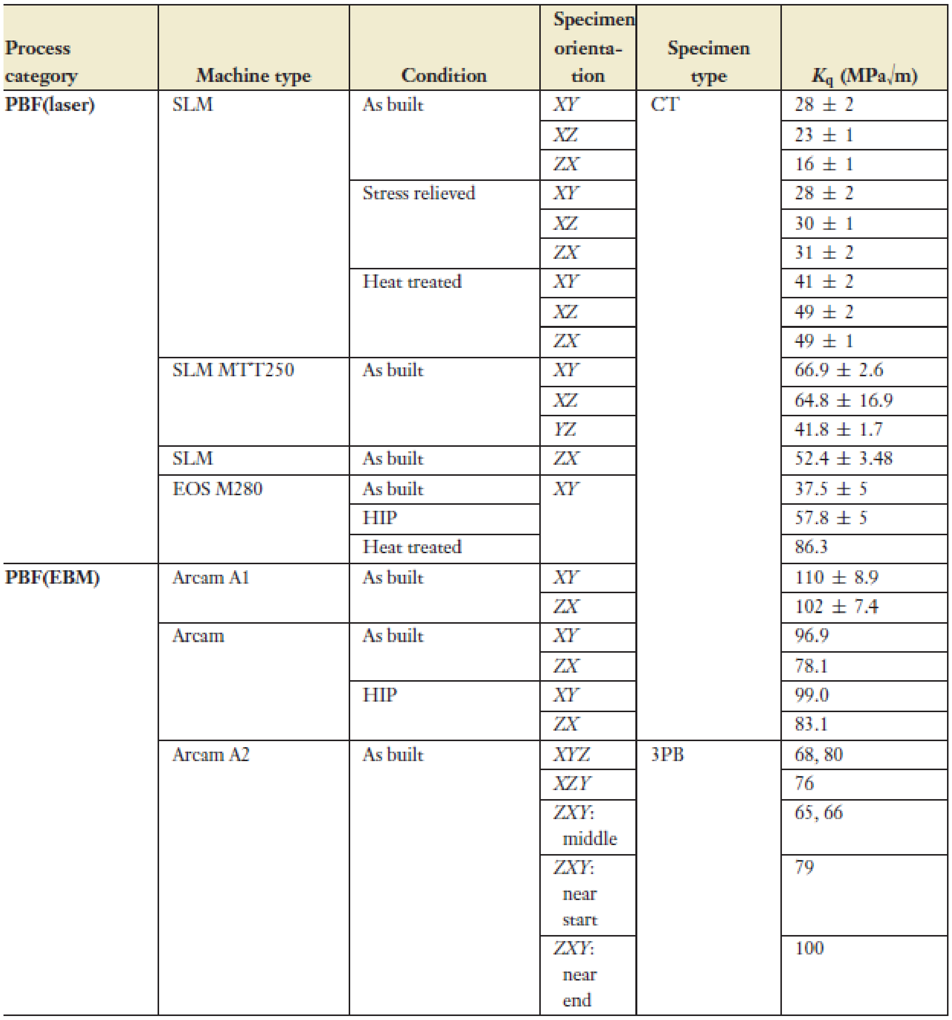

Process category	Machine type	Condition	Specimen orientation	Specimen type	K_q (MPa$\sqrt{m}$)
PBF(laser)	SLM	As built	*XY*	CT	28 ± 2
			XZ		23 ± 1
			ZX		16 ± 1
		Stress relieved	*XY*		28 ± 2
			XZ		30 ± 1
			ZX		31 ± 2
		Heat treated	*XY*		41 ± 2
			XZ		49 ± 2
			ZX		49 ± 1
	SLM MTT250	As built	*XY*		66.9 ± 2.6
			XZ		64.8 ± 16.9
			YZ		41.8 ± 1.7
	SLM	As built	*ZX*		52.4 ± 3.48
	EOS M280	As built	*XY*		37.5 ± 5
		HIP			57.8 ± 5
		Heat treated			86.3
PBF(EBM)	Arcam A1	As built	*XY*		110 ± 8.9
			ZX		102 ± 7.4
	Arcam	As built	*XY*		96.9
			ZX		78.1
		HIP	*XY*		99.0
			ZX		83.1
	Arcam A2	As built	*XYZ*	3PB	68, 80
			XZY		76
			ZXY: middle		65, 66
			ZXY: near start		79
			ZXY: near end		100

These studies provide a good starting point to understanding how the EBM and SLM additive manufacturing process parameters affect the grain structure, and subsequently the material properties. The grain structure orientation, influenced by the build direction, affects the facture toughness and crack propagation behavior. This is useful for a designer to consider when figuring out how their parts should be oriented in the build chamber for damage tolerant design and manufacturing. Vertical crack propagation in EBM Ti-6Al-4V is more energy demanding and less likely than horizontal propagation given the prior β columnar grains increasing branching and the scanning layers increasing the tortuousness of the crack path. The EBM Ti-6Al-4V as-fabricated horizontal crack growth behavior was more ductile than the vertical direction, therefore the fracture toughness was higher.

3.2 PROCESS EXPERIMENTATION

All experiments in this work were conducted using an Arcam A2X electron beam melting powder bed fusion AM machine shown in Figure 3.9. Table 3.2 lists some of the machine specifications provided by the manufacturer. The A2X consists of a control cabinet on the left and a chamber cabinet on the right. Within the cabinets are a cooling system that distributes cooling media to cool the column coils, the vacuum turbo pumps, and feed heat exchangers that cool electronic components. The chamber door on the right cabinet seals the build chamber and contains an observation window that is protected from heat and metallization by a manually operated shield. The operator is protected from radiation based on the door thickness, the external shell plate and lead glass.

Figure 3.9. Arcam A2X electron beam melting powder bed fusion AM machine.

Table 3.2. Arcam provided A2X specifications.

Parameter	units	Value
Build Tank Volume (X/Y/Z)	mm	250/250/400
Build envelope (X/Y/Z)	mm	200/200/380
Model-to-part accuarcy, long range (3σ)	mm	± 0.20
Model-to-part accuarcy, short range (3σ)	mm	± 0.13
Surface Finish (vert/horz)	µm	25/35
Beam Power continuously variable	W	50-3000
Beam Spot Size (FWHM) continuously variable	mm	0.2-1.0
Electron Beam Scan Speed	m/s	< 8000
Build Rate (Ti-6Al-4V)	cm^3/h	55/80
Number of Beam Spots		≤ 100
Vacuum Base Pressure	mbar	$< 1x10^{-4}$

In the control cabinet is a 60kV power supply that generates the power acceleration needed for the electron beam. Electrons are emitted from the top column above the build chamber which holds a filament that consists of lanthanum hexaboride. The printing was conducted according to ‘optimized’ default parameters provided by Arcam shown in Table 3.3. These parameters include a beam speed of 4530 mm/s and speed function of 45, a beam current of 15 mA with a max current set to 20 mA, and a focus offset of 25 mA. The default theme preheat temperature was set to 650 °C.

Table 3.3. The default ‘optimized’ process parameters for the melt theme provided by Arcam.

Parameter	units	Value
Beam Speed	mm/s	4530
Beam Current	mA	15
Max Current	mA	20
Focus Offset	mA	25
Speed Function		45
Snake		TRUE
Line Order		1
Line Offset	mm	0.2
Randomiszed Hatch		FALSE
Hatch Depth	mm	0.05
Speed Factor	mm	1.5
Thickness Factor	mm	0
Exponent Factor	mm^{-1}	0.5

A series of three experiments were conducted for this work and are detailed in the following chapters. The first experiment is called the Line Build which consisted of printing single melt lines on sintered powder in different directions. The Line Build was conducted twice, the first would only use the melt theme, while the second would only use the wafer (support) theme. The single melt lines for each build were then to be optically measured to analyze their topography, as well as their dimensional accuracy and variation. That experiment provided a fundamental understanding of the resulting melt combined with a set of process parameters (theme). Learnings from this experiment were carried forward into the following two experiments.

The second experiment was a progressively scaled version of the first experiment going from manufacturing a 1D melt to two dimensions and subsequently the layering 3D melt. This experiment is called the Step-Ramp build because the specimens were designed as either discrete 2 or 4 layer steps, or as ramps with a shallow enough slope to capture the staircase effect of the layering process. The primary idea behind this experiment is to analyze the geometric distortion and how it relates to increasing thermal mass (thickness). In addition, with every layer exposed with an area, the intra-build layer surface topographies can be analyzed for surface roughness and hatching scan quality. The set of 4 specimens, two steps and two ramps of 700 and 1400 µm in total thickness, would be repeated 3 times at different build heights for a total of 16 specimens per build. Their as-built configuration was compared to each other and the original CAD model to characterize the geometric deviation from nominal and from parts that should be identical.

The final experiment scaled from the previous two to manufacture an actual part component as a test specimen. The component would be a topology optimized cantilevered tapered box beam that is printed in two pieces and assembled. Learnings from the previous experiments would be incorporated in the upfront design of the build and the analysis. Two complete beams, four sections, were printed simultaneously. Their geometric distortion was to be measured by 3D scans of the resulting assembled beam surfaces. Three of these builds were carried out in series to not only compare part to part within a single build, but to characterize the stability and repeatability of the manufacturing process from build to build. Tensile specimens (ASTM-E466 9 mm diameter) were included in each build alongside the beams in order to get an idea of the strength of the material that makeup the beams. Future work will include physical strength testing of the beams to ultimate load in order to characterize the failure modes, strengths, and microstructures.

3.3 PROCEDURES

Metal powder, particularly titanium, is dangerous because of the high surface area and burn temperature so it is necessary to follow strict procedure and care in powder handling. In addition, the powder is expensive such that filling the powder hoppers of an Arcam A2X can cost upwards of $10,000 so any waste of powder with build failures or contamination is unacceptable. For these reasons all experiments were carried out by carefully following the instructions for machine operation and powder handling provided by the Arcam A2X operators manual. All handling of powder was conducted wearing proper personal protective equipment such as gloves, safety glasses, and respiratory masks.

Each experiment described in this work utilized a Grade 5 Titanium alloy (Ti-6Al-4V) produced via gas atomization and supplied by Arcam, and the powder had been used in many previous builds and experiments by this author and others at the university. The exact number of uses of the feedstock powder is unknown. No chemical analysis was ever performed on the powder, but it likely follows the trends described by S. Ghods et. al. [30] which meticulously tracked changes in EBM powder feedstock over the course of 30 builds. It is assumed the powder used in this work exceeded 30 builds of reuse. After a build, the sintered powder is reclaimed through the Arcam Powder Recovery System (PRS) while loose powder is vacuumed using a special vacuum designed for minimizing the risk of static discharge and explosion. Any powder thought to be contaminated with other materials, dust, or dirt was segregated and disposed of. Power reclaimed from the PRS and the vacuum was run through a sieve with a 120 mesh in order to remove any particles above 125 µm effective diameter. Once sieved the powder was either stored in sealed metal buckets, or returned to the hoppers withing the A2X build chamber.

Setup of the Arcam A2X followed the procedure detailed in the operator’s manual. This first involved loading the build file and selecting the proper start plate size which then sets the start plate size specific preheating process parameters. Next the process parameters are set for each layer that will include selecting a preheating, melt, and wafer (support) theme. The themes are a collection of preprogrammed process parameters that control the beam functions. Models defined in the build file are then loaded for each theme so the machine can process supports and parts differently. From there, the manual calibration procedures are executed for leveling the build plate and setting the layer powder fetching quantity before installing the heat shields, cleaning the door and seals and initiating the vacuum. Once the vacuum is set, the electron beam is switched on and calibration continues for the center point and beam focus.

Completion of a build also followed the A2X operator’s manual for extracting the powder cake and the build plate and moving them to the PRS to extract the parts and remove sintered powder. All specimens were handled carefully with gloves and taken for post processing and/or metrology. The desire for this work is to better understand the as built condition since post process heat and surface treatments add time and cost to an end product. It would be optimal if parts manufactured via additive could be net shape and functional right out of the build chamber. The Line experiment received no post processing and all measurements were conducted while the specimens and sintered powder were attached to the build plate. The Step-Ramp experiment removed the specimens from the sintered powder and start plate via the PRS, but the supports were not removed. In the final tapered box beam experiment, the specimens had the support structures removed and joint surfaces cleaned. To remove the support features they were initially trimmed from the specimens using manual cutters, however this still left behind small nubs at the attach points. The support attachment surfaces were then ground down and smoothed using a tungsten carbide rotary tool.

3.3.1 *Optical Inspection*

Two experiments utilized a Keyence VR-3100 for the purpose of topological profile and surface measurement that is shown in Figure 3.10. The user manual describes the system as a 3D profile measuring macroscope that uses high-intensity LED light and a 4-megapixel monochrome CMOS to obtain a one-shot fringe projection image. Fringe projection allows the instantaneous measurement of height, length, angle, volume, etc. of a portion of an object. With fringe projection, height differences are distorted and calculated using triangular ranging. The system also contains a telecentric lens which allows the image size to not change despite varying focal positions making it ideal for measurement.

Figure 3.10. Image of a Keyence VR-3100 wide-area 3D measurement system.

3.3.2 *Geometric Scanning*

Where the Keyence VR-3100 excels at measuring the topology of small flat specimens, the tapered box beam specimens were too large and curved to be measured with that system. Therefore, the beam specimens were sent to Digital Scan 3D to be professionally 3D scanned. The scanning device used was a Kreon Ace measuring arm with a Skyline 3D scanner. Each specimen was placed on a table with the calibrated scanner, while the operator manually manipulated the scanner by hand sweeping along the surface of the part without contact. This scanner employs a blue laser and HD camera which is capable of measuring reflective materials like titanium. A dense point cloud is generated to accurately capture the surface topology with a laser scan speed of up to 600,000 points per second. After several passes with the scanner along the beam, the specimen is rotated and scanned again to capture additional surfaces. That procedure is repeated several times until as much of the surface possible is mapped with a 3D point cloud. Software is used to assemble the various point clouds into a single geometry map which is then converted into a .stl file. Figure 3.11 shows the configuration of the measurement arm and scanner.

Figure 3.11. Image of a Kreon Ace arm with a Skyline 3D scanner.

3.3.3 *Powder Handling*

The Arcam user manual describes a suggested powder recycling routine for Ti-6Al-4V to keep the oxygen content within approved limits even with a large number of reuses; although, it does not state any particular number of reuses. It requires the tracking of three different powder batches that are labeled A, B, and C for this example, and directs fresh Extra-Low Interstitial (ELI, i.e.

higher purity) powder with a target oxygen content of 0.08% to be blended with the used powder at the production site. The goal of the mixed powder is to obtain homogeneous powder properties while keeping the powder quantity constant.

The initial powder, described as Powder A with an oxygen content of 0.08-0.17%, is used by itself for an initial build. Once complete, the sintered build is extracted and should be weighted before it is placed in the PRS. The manual says that prior to cleaning, an equivalent or slightly more in weight quantity of ELI powder, Powder B, should be added to the PRS and that the cleaning process will efficiently mix the two batches. This new mixed powder is now labeled as Powder C which should be emptied from the PRS and stored in a steel container with a lid. This process is to be repeated until all of the initial Powder A is consumed at which point it is stated that the accumulated quantity of the mixed Powder C will be similar to the original quantity of Powder A.

Then the mixed powder is to be sieved, followed by an Inductively Coupled Plasma (ICP) analysis for metallic elements and a LECO combustion analyses for oxygen, nitrogen, carbon and hydrogen. Once properties are determined, the mixed powder is to be relabeled as Powder A and the process as described before is repeated so long as the oxygen content stays below the desired levels (0.22%) and the various elements remain within Ti-6Al-4V specification. It is suggested that the quantity of Powder B being added to the PRS after each build be adjusted as necessary to keep the recycling loop going. It is also suggested that a record be maintained of the weight of new powder being added, the weight accumulation of the mixed powder, and the properties from the chemical analyses.

The manual concludes that monitoring other powder properties is not necessary and that Arcam’s experience has shown that if a new powder works well, it will perform better after recycling. There is no mention of the damage that occurs to the powder in the PRS as shown in S. Ghods et. al. [30]. A final statement addresses a hypothetical situation in which Powders A and B need to come from the same batch for validation reasons. In that case Arcam recommends starting with a large batch of ELI powder and separating out 40-50 kg to be labeled Powder A and the rest Powder B. Then Powder A is to be used exclusively until the oxygen content rises to the desired level before starting the mixing routine. The manual does not state where the oxygen is introduced into the powder, nor does it state the approximate number of times Powder A should be used prior to the beginning of mixing.

The implications of running this powder handling procedure is that a standard powder is only purchased once at the beginning, and all recurring powder purchases will be for ELI powder. Therefore, it is important to know the cost difference between standard and ELI powder when calculating the recurring cost of operating this machine with that procedure, as well as the cost and processing time of the chemical analysis.

3.4 ROCKET MOTOR COMPONENT BUILD CASE STUDY

Prior to conducting any experiments, a case study was performed to attempt to manufacture various rocket motor components. The purpose of this test build was to exercise the entire manufacturing process by learning how to setup a build with multiple parts, how to properly operate the Arcam A2X machine, and understand the powder handling process. The material loaded in this build was previously used standard Ti-6Al-4V powder supplied by Arcam. The parts to be built were selected based on models provided by the UW Aeronautics and Astronautics SARP team, but were not ordered or purchased. Of the models there were two particularly interesting parts, one of a small rocket nozzle with internal cooling channels, and the other was an injector plate with a range of holes of different sizes, shapes, and angles. 3D printing rocket propulsion components is a big area of interest in the industry since they tend to be highly complex and expensive to manufacture by traditional methods. It is speculated amongst industry experts that any company that is not printing their thruster components will be out of business in 5 years.

Common practice in the metal additive manufacturing world is to anchor all parts to the build plate either directly or with supports to prevent them from shifting in-process and causing a build failure. While this build was merely for familiarization purposes, some additional value was obtained by testing the EBM process capabilities of nesting parts vertically. Two nozzles were placed within the build envelope, but one was oriented above the other and in the opposite direction. Beside the nozzles were two injector plates and eight other much smaller components to fill in the envelope. Once the electronic build file was prepared and sliced, it was loaded into the machine along with the powder. All setup calibrations were performed per the Arcam User Manual and in person training. After the build was fully completed, it was extracted and processed with the Arcam PRS.

3.4.1 *Build Preparation*

Four different models were chosen for this trial build, a rocket nozzle, a rocket injector plate, a tap test, and a UW Fan Blade trinket as displayed in Figure 3.12. A quantity of two of each model was placed in the build envelop using Materialise Magics software. Due to the size of the nozzles, the 210 x 210 mm build plate was selected and a minimum of 5 mm vertical distance was maintained between the build plate and the parts. One nozzle was located near the baseplate with the bell pointing down and supports along the bottom edge tying it to the build plate. To the side of the first nozzle, two injector plates were placed, and were tilted on end and located higher above the build plate to fit within the envelope. The injector plates were also tied to the build plate with much taller supports. The two tap tests and six UW Fan Blade trinkets were also located near the plate and tied to the build plate with supports, tilted slightly forward by 5 degrees. Nested above the other models was the second nozzle which was printed inverted with the bell pointed up. Supports were placed round the edges along the underside at the base of the part and the underside of the bell at the top. The supports on the upper nested nozzle extended 20 mm into the powder bed below, but were not tied to any other models or the build plate.

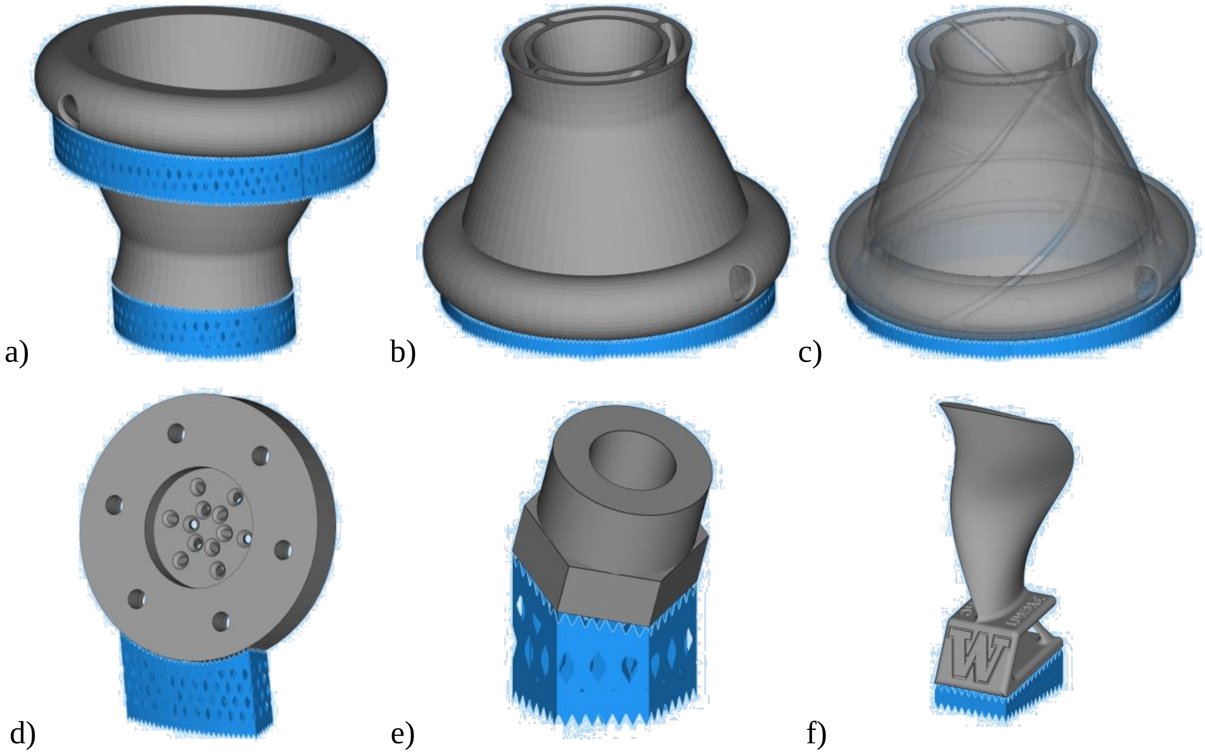

Figure 3.12. Models (not to scale) printed with support features: a) upper nozzle, b) lower nozzle, c) lower nozzle transparent to show cooling channels, d) injector plate, e) tap test, f) UW Fan Blade trinket.

The same support feature geometry was chosen for all locations and can be seen in detail in Figure 3.13. For this build, only block supports were used which was based on industry experience, guidance from Materialize, and success of other builds on other machines. It is assumed that fewer supports are needed for EBM versus SLM processes due to the sintering of the powder prior to the melt scans, however supports that resemble fin type heat sinks are still needed to aid in the dissipation of heat from the melt area. Another key aspect of this build is that while all the parts had some flat or planer surfaces, none of them were placed parallel to the build plane. All parts were tilted to some angle (5 degrees minimum) off of the build plane normal direction. It was hypothesized that doing this will obtain a more uniform surface finish on all sides of the part, whereas direct up skins, side skins, and down skins come out with very distinctly different surfaces.

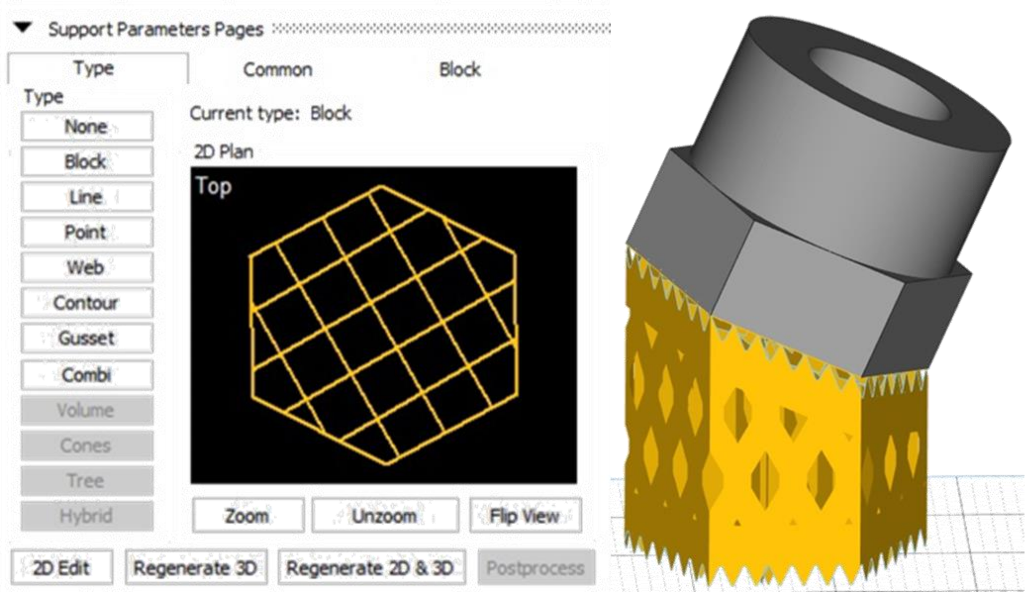
Current type: Block

Figure 3.13. Detailed image of support geometry.

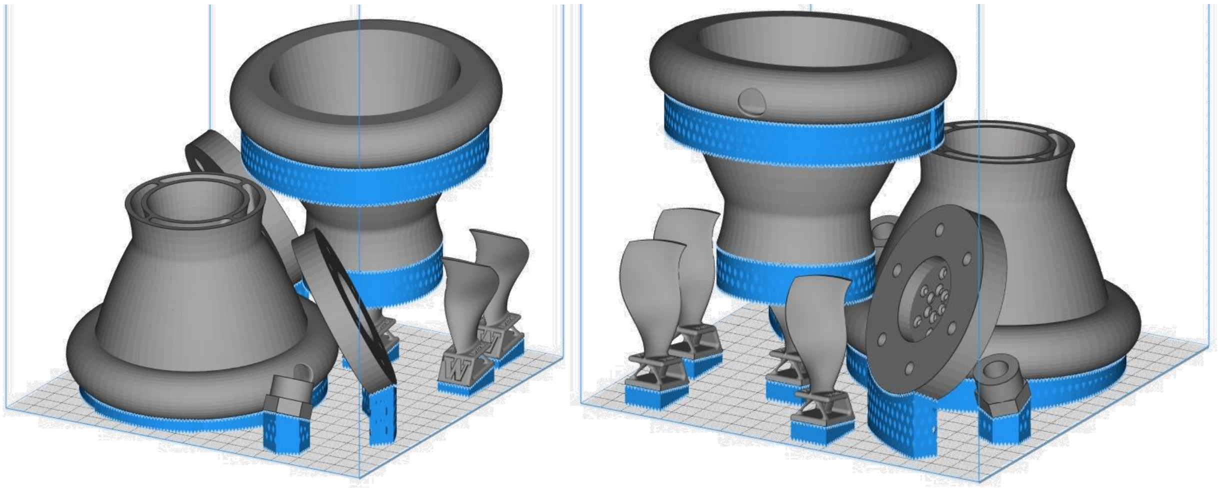

Figure 3.14. Build setup with all models located in build volume.

Figure 3.14 shows the finalized build setup, and from there the support geometry and parts were exported and saved as separate .stl files. A build plate .stl model called ‘box’ was copied from a previous build. All of the models were uploaded to the Arcam Build Assembler software per directions provided in training materials. One issue that was a source of delay was that initially the build was not properly centered when loaded into the build assembler. When loading the models, it is necessary to define the “Origo” meaning origin. This is enabled by selecting the Origo check box which will then populate a drop-down list with all the loaded models to pick from. Selecting the build plate called ‘box’ will then center the build in the software. The build was sliced using the default settings and the information saved as an ABF (Arcam Build File). That file was copied to a USB flash drive and loaded into the A2X machine computer.

3.4.2 *Machine Setup and Build Processing*

The build setup procedure was accomplished by recalling notes that had been taken during training and following the Arcam A2X manual instructions. The safety precautions employed were that nitrile gloves to be worn at all times, lab coats and respiration masks were worn while handling powder and machine equipment. The powder that was loaded to the machine hoppers was previously used Ti-6Al-4V powder from Arcam of unknown pedigree and stored in unmarked 20 kg cans. Plate leveling, rake fetch calibration, beam centering, and beam focus calibration were all completed successfully, and the build was initiated.

The build completed with no major issues. At a build height of 105 mm an arc trip warning was issued and identified as a recoverable error. Also, there were warnings about model clipping occurring as it was detecting some models were too close to the build envelope. That warning is not well understood since the build envelope used for the setup in Magics was 200 mm by 200 mm and none of the models exceeded that envelope. Upon completion of the cool down it was observed that the top layer was not perfectly flat and powder appeared to be lacking around the edges of the build envelope most notably on the right side. The cause of this was a lack of powder being fetched by the rake from the right hopper, this hopper was discovered to be empty once the build chamber was opened. The left hopper had some powder remaining in it but it was close to empty. Nonetheless, the parts within the build appeared unaffected by the powder supply running low.

Removing the build was accomplished by following the step-by-step instructions from the Arcam user manual. Placing the sintered powder cake into the trolley was difficult since the build was very heavy (~30 kg) and physical access is awkward. Despite not being heated directly by the beam, the powder under the build plate had been sintered as well which made carefully digging out the thermocouple quite tedious and time consuming. The trolley was then wheeled over to the PRS and the build was placed inside where the sintered powder could be blasted away by the combination of pressurized air and titanium powder in order to expose the parts buried inside. The build plate separated from the cake and parts very easily and early in the process, without any direct effort.

3.4.3 *Results and Observations*

Upon observing the build plate, it was evident from the heat discoloration pattern that the plate was rotated with respect to the build chamber by ~5 degrees as seen in Figure 3.15. This highlights the manual operation of build plate placement and the dependence upon the skill of the operator. It would be best to use a straight edge as an alignment feature when initially placing the build plate to not only check for it being centered in the build envelop but also square with the edges. If the build plate had been further rotated and parts had been placed in the corners, the beam would have missed the plate and possibly initiated a build failure. It does not appear that reusing the build plate without refinishing it had any impact on the success of this build or the parts that were printed. Given the previous model clipping errors, no affects due to this error were discovered.

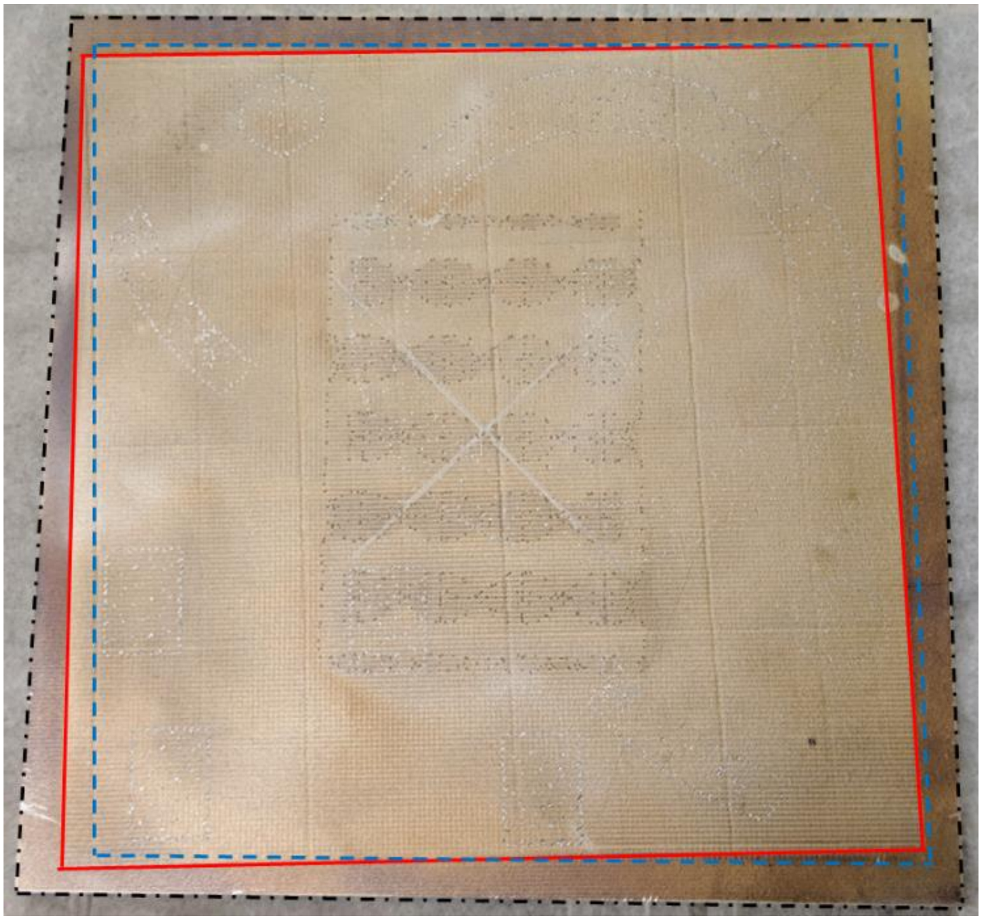

Figure 3.15. Build plate after build completed, edge of the build plate (black outline), prior build (blue outline), SARP build (red outline).

The parts themselves did have some immediately noticeable geometric defects. The UW Fan Blade trinkets had some warping upwards along the thin rear edge corners that can be seen in Figure 3.16. This was from a lack of supports in this area that would have helped dissipate the heat better into the powder below. Past prints of this model contained some very minor supports in this area and there were no visual defects. The small angle downward enabled the text on the top to be of better visual quality and easier to read.

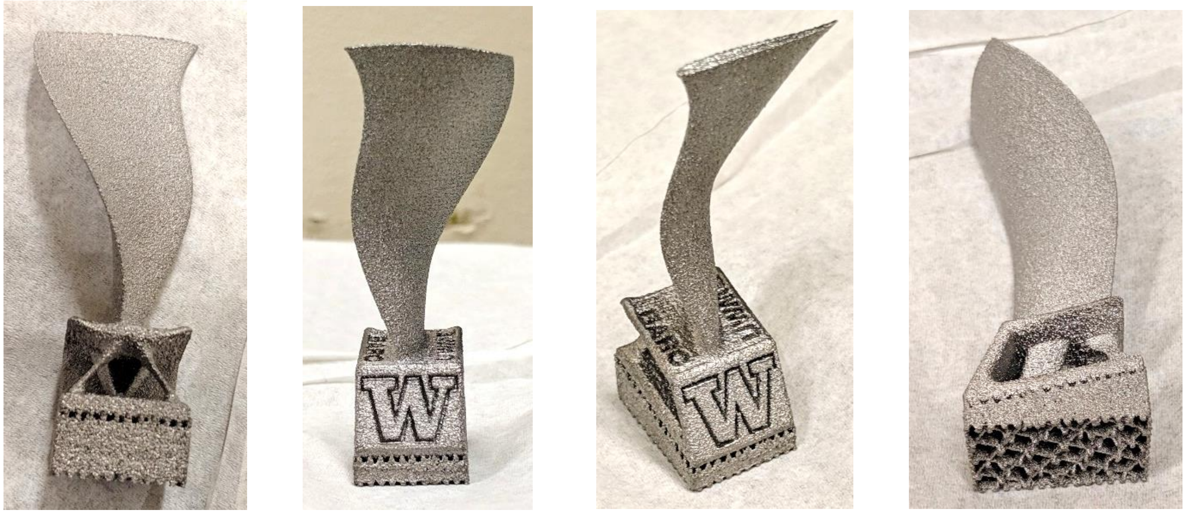

Figure 3.16. UW Fan Blade Trinket with warped rear corners.

Another part that had noticeable geometric defects were both of the injector plates in Figure 3.17. From the way they were angled in the build, just beyond where the supports ended, the downward facing edge is missing until a certain layer height when the edge began printing correctly again and finished without further defects or a more serious crash. This defect began immediately after the supports ended on a downward edge, was mirrored on the opposite side of the injector plate, and the other injector plate looked identical, all indicating this edge required additional support. For the larger holes, they were noticeably not circular with the top of the holes flattening out. The small angled holes in the middle and the large center ring on the one side were also not circular.

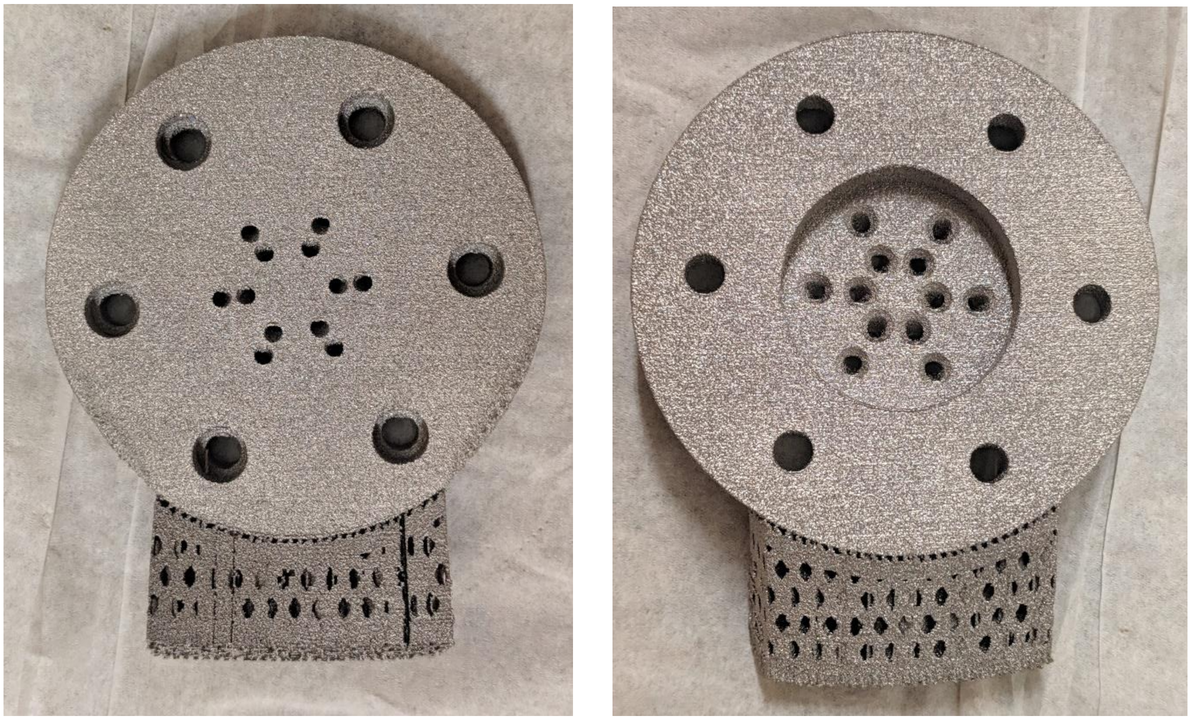

Figure 3.17. Resulting injector plate part with supports.

The tap test models in Figure 3.18 were not complex geometries, nor oriented in a unique way, just 15 degrees off the build plane, and they contained no immediately observable defects. One thing to note though is that the layers are very noticeable on the top surface, also that the upper regions of the edges have a protruding lip while the lower region edges appear slightly filleted. The lower and upper nozzles in Figure 3.19 also appear to have no significantly noticeable defects. These nozzles however have some internal cooling channels which made powder removal in the PRS quite difficult and time consuming. Without some form of non-destructive evaluation like x-ray or CT, it may be impossible to determine if any residual sintered powder is still trapped inside.

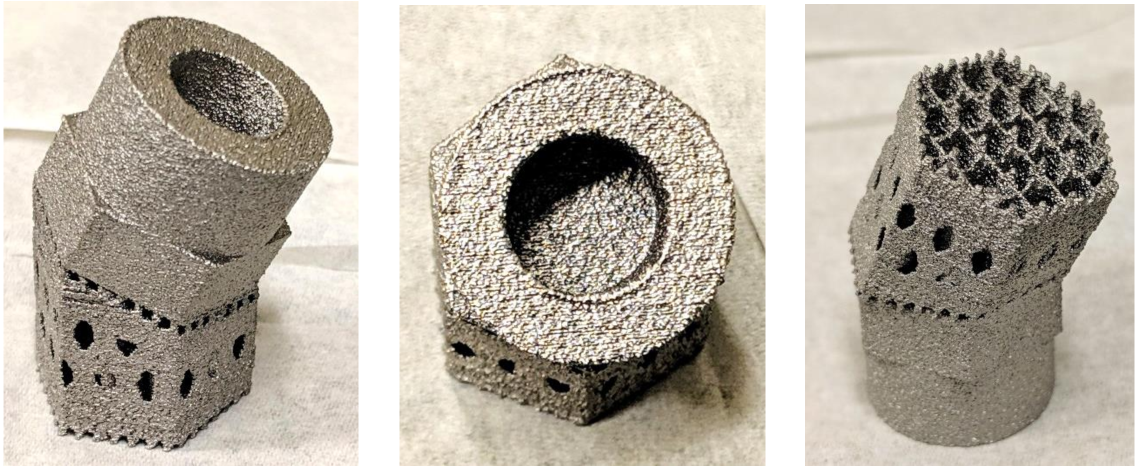

Figure 3.18. Resulting tap test part with supports.

Figure 3.19. Resulting lower nozzle (left) and upper nozzle (right) parts with supports.

From the resulting parts depicted, it is obvious that the as-built surface roughness is quite poor on all surfaces. While all the parts were oriented to prevent any flat faces from being parallel with the build plane, there was still a visually noticeable difference from up skins, side skins, and down skins. The up skins on the lower nozzle were still shinier and smoother than the side skins. Most down skins had supports making them difficult to compare directly, but the underside of the fan blade was unsupported and despite being not being parallel to the build plane was much rougher than any side skins. Therefore, slightly angling the parts in the build volume does make the overall surface more uniform than not angling them, but there is still a visually noticeable difference between up, side, and down, skins. If post process surface smoothing is required there will be different levels of energy required for smoothing different sides.

In regions where supports were located, there was little to no geometric distortion. The observed geometric defects were clearly from a lack of support placement. There is still much to be understood on where supports should be placed, but currently there is no analytical method for properly locating them to provide either structural or thermal support. The strategies currently available to an engineer or operator are guessing, trial and error, tribal knowledge, or software automatic generation. The software automatic generation is extremely crude, Magics (the industry leading build preparation software) simply looks for downward facing triangles in the .stl model and places a variety of different types of supports on those surfaces. From shared tribal knowledge, some of the automatic supports can actually cause build failures or be impossible to remove; therefore, current software automatic support generation is to be used as a guide, but not to be completely trusted to provide good solutions.

In this particular build, Figure 3.20 shows how the support geometry selected was difficult to remove. The size of the teeth touching the part were too small, or non-existent, and that did not allow for manual cutters to be inserted to cut away the support material. The vertical cross hatch spacing of the support structure was also too narrow to allow the insertion of pliers that easily could rip the supports away. Support adhesion to the build plate was apparently enough for the build to be successful; in SLM systems residual stress has been known to pull supports from the build plate or tear supports apart to cause cracks in the parts or complete build failures. The higher build chamber temperatures in the EBM system clearly help reduce residual stress since the rocket nozzle showed no issues despite its larger thermal mass. As far as removing powder from the middle of the supports, this was possible, but it could have been less effort by making the size of the diamond perforation larger. This leads to a typical operator dilemma, where supports of this particular geometry were placed the parts were successful, but the supports were difficult to remove. If changes are made to make supports easier to remove, the risk is potentially increasing that the build or parts may not be successful.

Figure 3.20. As-built support structure manufactured during SARP build.

Table 3.4 below qualitatively summarizes the forms of geometry an EBM machine prints well or fails to print well based on the results of this case study. When designing or selecting a part for the EBM additive manufacturing process, it is advised to avoid geometric features that the machine struggles to produce.

Table 3.4. Qualitative geometry assessment for EBM process.

Geometry that prints well	Geometry that should be avoided
Curved surfaces	Flat surfaces
Smooth transitions	Circular holes
Thick walled structures	Circular edges
Text	Unsupported corners
Support features	Smooth as-built Surfaces

3.4.4 *Discussion*

The ability to additively manufacture metal rocket propulsion components is a big benefit to the industry since they contain complex surfaces to satisfy the physics, but expensive to traditionally manufacture. This leads to designers having the make compromises with the performance to ensure it can be fabricated economically. This build demonstrated the capability of the Arcam A2X electron beam melting machine to additively manufacture small rocket propulsion components in Ti-6Al-4V, in addition to providing a familiarization and learning test. Of the parts that were manufactured, the injector plates showed the most significant geometric defects due to improper support or poor alignment to the build direction. However, it is the opinion of this author that the part should be redesigned if it is to be manufactured via the EBM process so as to not contain geometric features common to traditional manufacturing. The vertically nested nozzle was successful in terms of evaluating the A2X capability to manufacture "floating" geometry, an aspect of the EBM process that SLM is not capable of.

One important lesson learned is that the support structures need to be redesigned to enable 1) removal with less effort, 2) faster powder excavation without compromising the parts they support, and 3) to reduce the quantity of powder consumed or becomes waste. The surface area of supports must remain large to act as heat sink fins all while spacing them further apart. The supports must serve two purposes, one is to prevent the part from shifting during the build, and the second to adequately dissipate heat from the melt pool to prevent significant distortion. There should be an analytical method developed to anticipate where supports are actually needed and how much surface area is required for a successful build. A deeper understanding of design and capabilities of the supports is necessary to fully understand the structural needs and capabilities, as well as the thermal transfer needs and capabilities.

Chapter 4. LINE EXPERIMENT

When analyzing the results of an Arcam A2X build, it is difficult to see the nuances of what is actually happening with the beam power and how the beam moves, especially since the melting happens so quickly. The desire for this experiment was to lay a single melt beam segment that was 4 mm long onto a powder bed. The effects of the start plate were not desired, so the line specimens were designed to be 3 mm (60 layers) above.

Jamshidinia, et. al. [31] produced a similar short single melt line in titanium powder to investigate the understanding of the effects of process parameters on the heat distribution using a moving EBM heat source. The supposition was that the Arcam algorithm selected melt theme would melt the specimen geometry with a continuous moving heat source. That work did not simulate the builds in what is believed to be the correct form by evaluating a moving energy source. It is thought that the referenced build actually used a stationary spot melt pattern to manufacture the line due to the Arcam contour melt theme.

This experiment conducted here-in used two different themes to demonstrate the differences in energy input and the resulting outputs. Each of the resulting melt specimens was compared with that of the referenced work by Jamshidinia, et. al. and some conjectures regarding their work were made based on the results of this experiment. The influences of different electron beam scanning themes are studied here, where the molten pool widths, depths and surface topographies are measured. Surface conditions are investigated and explained based on energy input. These characteristics can also be used to validate numerical models of the heat/energy application as it is associated with the observed build characteristics.

4.1 METHODS

In the Jamshidinia, et. al [31] study, there was a micro image of an approximately 4 mm long single melt line using titanium powder and an electron beam as an energy source as seen in Figure 4.1. Therefore, a build was designed to produce a similar result in an Arcam A2X electron beam additive manufacturing machine. The design was developed to mimic another diagram from that paper which showed the line being melted 3 mm above the 10 mm thick stainless-steel start plate. A CAD model was generated as shown in Figure 4.2 which contained 5 experimental lines surrounded by powder containment cylinders on a 210 mm by 210 mm start plate.

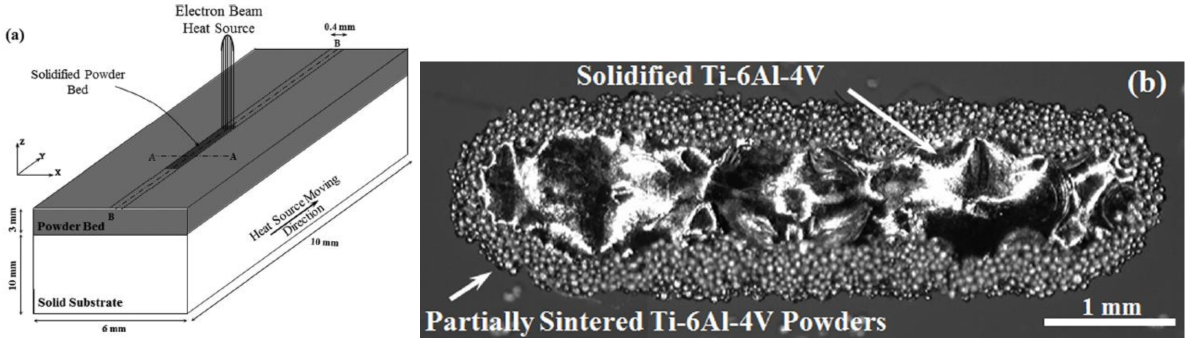

Figure 4.1. Diagram (a) and image (b) of a single melt line in titanium powder using an electron beam [31].

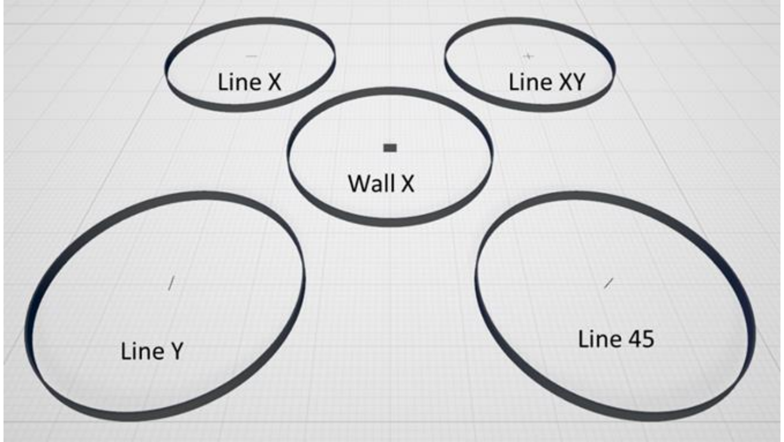

Figure 4.2. CAD model of experiment showing the position of each specimen and the powder containers.

4.1.1 *Specimen and Build Design*

This experiment would contain a single line oriented in the X direction (Line X), Y direction (Line Y), 45° (Line 45), a crossing of two XY perpendicular lines (Line XY), and a wall in the center of the build oriented in the X direction (Wall X). It was desired that each line be a single beam width, therefore the CAD model line specimens were configured to be 0.4 mm wide, 4 mm long, and 0.05 mm deep (the layer thickness). The wall model was the same geometry as the lines, except that it started at the first layer and continued up through the full build height of 3 mm.

Knowing that specimens of the designed size and thickness would be fragile, extracting the build without disturbing them or the powder around them until they could be imaged would be difficult. Powder containment cylinders were designed around all build articles at a distance of 30 mm radius and full build depth to control movement of the powder and specimen. That distance was chosen so the local sintering (preheat 2) around the containment cylinder would not extend into the center where the specimen would be printed. No support features were placed in this build. The centrally located wall specimen extended from the start plate to the top powder layer, and the line specimens were melted directly on top of the powder bed in the final layer. The powder utilized for all runs in this experiment was reused Arcam Ti-6Al-4V of unknown pedigree.

4.1.2 *Machine Setup*

This experiment was repeated twice, the first run was with the Arcam default “melt” theme selected and the second with the “wafer” theme selected. The entire build with all the specimens was designed as a single solid part model using CATIA V5 and then tessellated and exported as an .stl file. None of the specimens required support structures so the typical step of arranging the build and creating those support models using Materialise Magics was bypassed. The .stl model was sliced using the Arcam Build Assembler software, but this experiment ran into an issue with the themes.

Typically, the part files are loaded as “parts,” and the software automatically pulls in the support files that Magics creates. For this build with a single part file and no supports, all the components were loaded as a single part, sliced, saved as an .abf build file, and loaded onto the machine. The first build was setup on the Process tab of the Arcam A2X EBM Control to use the default “preheat” theme with no models and the default “melt” theme with the one model selected and without a “wafer” theme loaded. That build ran successfully without errors as seen in Figure 4.3. The second build was setup similarly with the same build file, and on the Process tab used the default “preheat” theme with no models and the default “wafer” theme with the one model selected and no “melt” theme loaded.

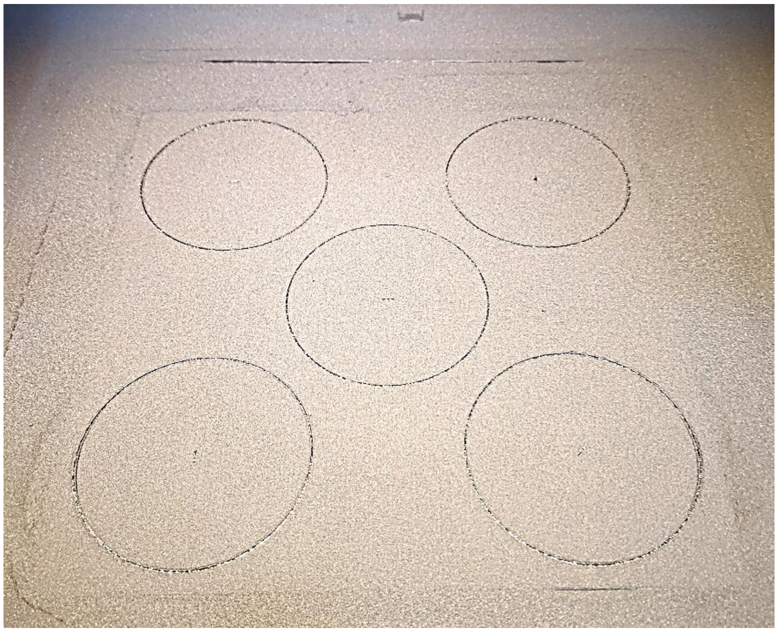

Figure 4.3. Image of completed Line build in the powder bed and ready to be extracted from the build chamber.

During the second run with the wafer theme, after the start plate preheating was complete, a problem was detected with the initial layers as no melting was taking place. The machine was merely going through the preheating and sintering phases without melting the powder containment cylinders or the Wall X specimen before it continued on to add the next powder layer. After several layers, the build was aborted and left to cool to 80° C. The reason for the lack of melting was hypothesized to be due to 1) the build file needed to be recreated with the part file loaded as a wafer, and 2) the EBM control software needed a melt theme to still be loaded even with zero models. Therefore, a second build file was created with the .stl file being loaded as a support rather than a part in the Build Assembler software, and on the Process tab of the EBM Control a "melt" theme was added with zero models.

Unfortunately, with this setup the machine refused to even start the build process, it signaled a "Analyse Failure" error, and directed the operator to check the log file. Once the log file was located and reviewed it indicated the error occurred because the melt theme was loaded with zero models. Clearly the second hypothesis was incorrect and the "melt" theme was removed from the Process tab. That restored the setup to the original setting with the default "preheat" theme with no models and with the default "wafer" theme with the one model. This time the second build with the "wafer" theme ran successfully which concludes that theme selection is initiated at the Build Assembler slicing stage rather than at the EBM Control Process tab stage. Each of the run's build time was fairly quick and the build only took about 30 minutes to complete.

4.2 RESULTS

Short videos of the experiment builds were recorded via cell phone (Pixel 3 XL) through the A2X observation port window. For each build a video captured the initial layers, followed by a couple middle layers, and then the last few layers; images of the final layers are shown in Figure 4.4. The scan strategy for the build was noticeably different from the two themes. The “melt” theme scan shown in Figure 4.4a moved around the build chamber in quadrants with numerous melt pools moving around the corner powder containment rings profiles while doing segments of the middle ring. By contrast the “wafer” theme scan used numerous melt pools that moved around the entire powder bed at the same time like the image in Figure 4.4b. There was also a visual intensity difference where the “melt” theme melt pools appear very bright and white, while the “wafer” theme melt pools appear dimmer and yellowish. This is an indication that the “melt” theme scan uses a higher energy beam than the “wafer” theme scan to obtain more complete melting and mixture with the layers below.

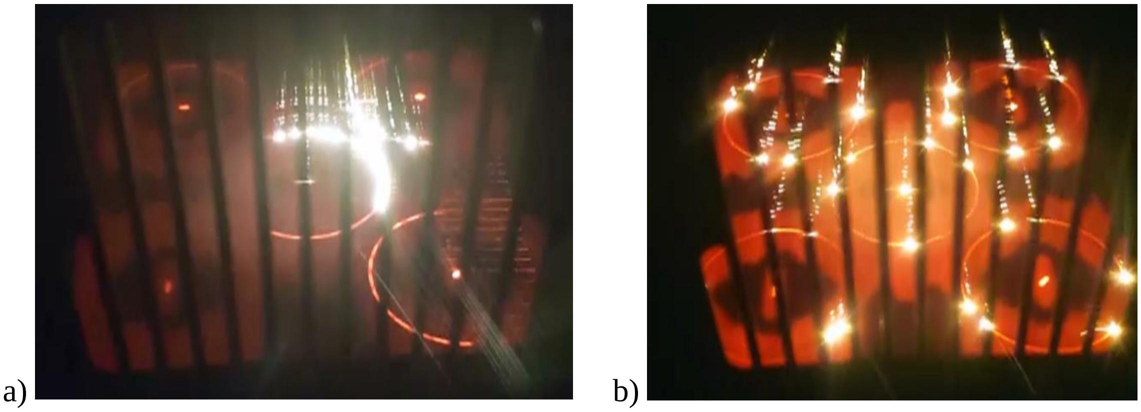

Figure 4.4. Image captured from video of the line experiment during the final layer of the melt theme (a) and wafer theme (b).

Once complete, each build plate had to be carefully removed to avoid disturbing the powder around the specimens, and the build plate with the specimens intact shown in Figure 4.5 had to be transported to a different lab for analysis. The specimen upper surfaces were imaged at 80x magnification with a Keyence VR-3100 using fringe projection to measure the surface topography. Due to the size and weight of the build plate with sintered titanium, the imaging platform could not adequately support the total mass so not all specimens were able to be sufficiently imaged and measured. The intersecting XY lines in particular were not able to be completely measured, and the image of the melt theme Line X specimen contains some blurred regions where the Keyence platform shifted slightly.

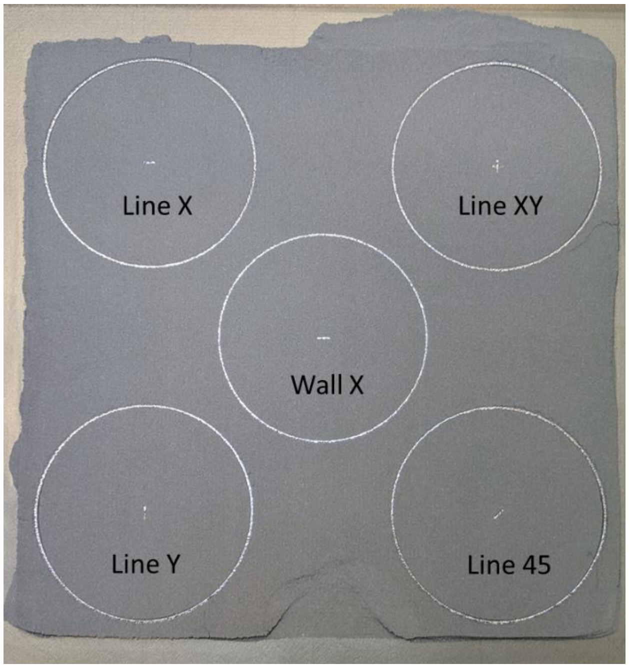

Figure 4.5. Image of successful melt theme build extracted from the powder bed and ready for imaging.

4.2.1 *Melt Topology*

In the following descriptions the melt theme specimens will be described first, followed by the wafer theme specimen as a comparison.

The Line X specimen is shown in Figure 4.6 and shows that the build contains what appears to be overlapping circular spots melted into the powder bed. At both extreme ends of the line are melted pockets containing unmelted powder. It is not certain, but this powder could have fallen in from the surrounding powder bed after the beam melting process had stopped. On top of some of the middle-melted areas are small powder particles that became partially melted into the surface.

At the edges of the melted circular spots are ridges that resemble oscillating waves, much like those created by a rock that is thrown into a still pond. The number of spots in this specimen are difficult to count due to the poor image, but there appears to be the shape of eight overlapping spots. The top of the melt surface is smooth and shiny, and the general shape is concave like a satellite dish. The edge of the melt area where it meets the sintered powder is very rough and not straight. The overlapping circular spots provide insight into why EBM parts have such poor surface finish as diagramed in Figure 4.7, if the Arcam slicer determines these lines are contours and utilizes a spot melting scan strategy then a smooth surface is far from possible.

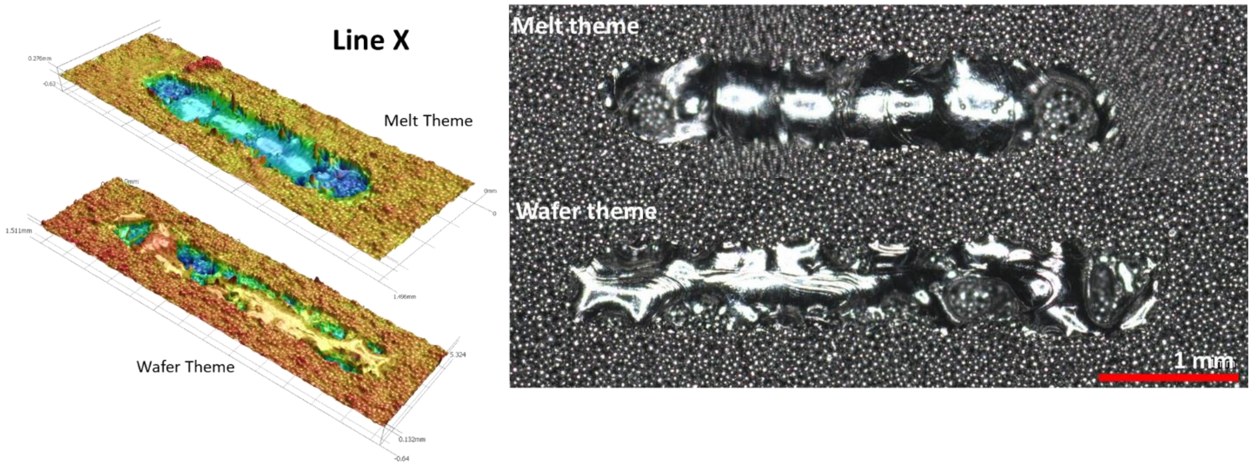

Figure 4.6. Image results of the Line X melt and wafer theme specimens.

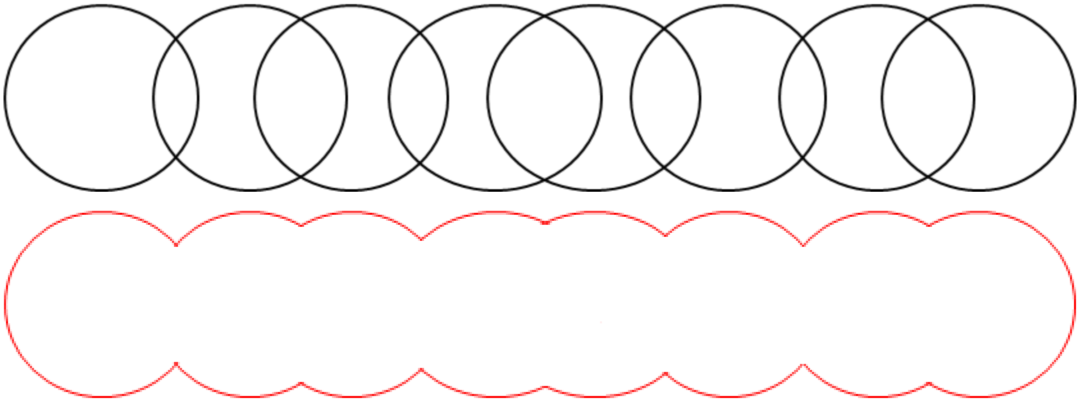

Figure 4.7. Diagram of observed spot melting pattern using the melt theme and the residual external side surface that this pattern creates.

With the melt theme, the melted line is sunk below the powder bed surface with an average depth of 240 µm along the axial line of the melt shown in Figure 4.8. The deep pockets on the ends appear to reach as low as 400 µm, but that cannot be determined since they were partially filled with unmelted powder. The bowl-shaped width cross section shows the edges reach up to less than 100 µm. For perspective, the layer thickness for this build is only 50 µm, revealing that the power of the electron beam is penetrating as many as eight layers deep into the powder bed. In the CAD model the target line length was 4 mm, but the measured length was only 3.717 mm. The CAD model width was purposefully undersized at 0.4 mm to ensure a single beam width, while the measured melt width was 0.691 mm.

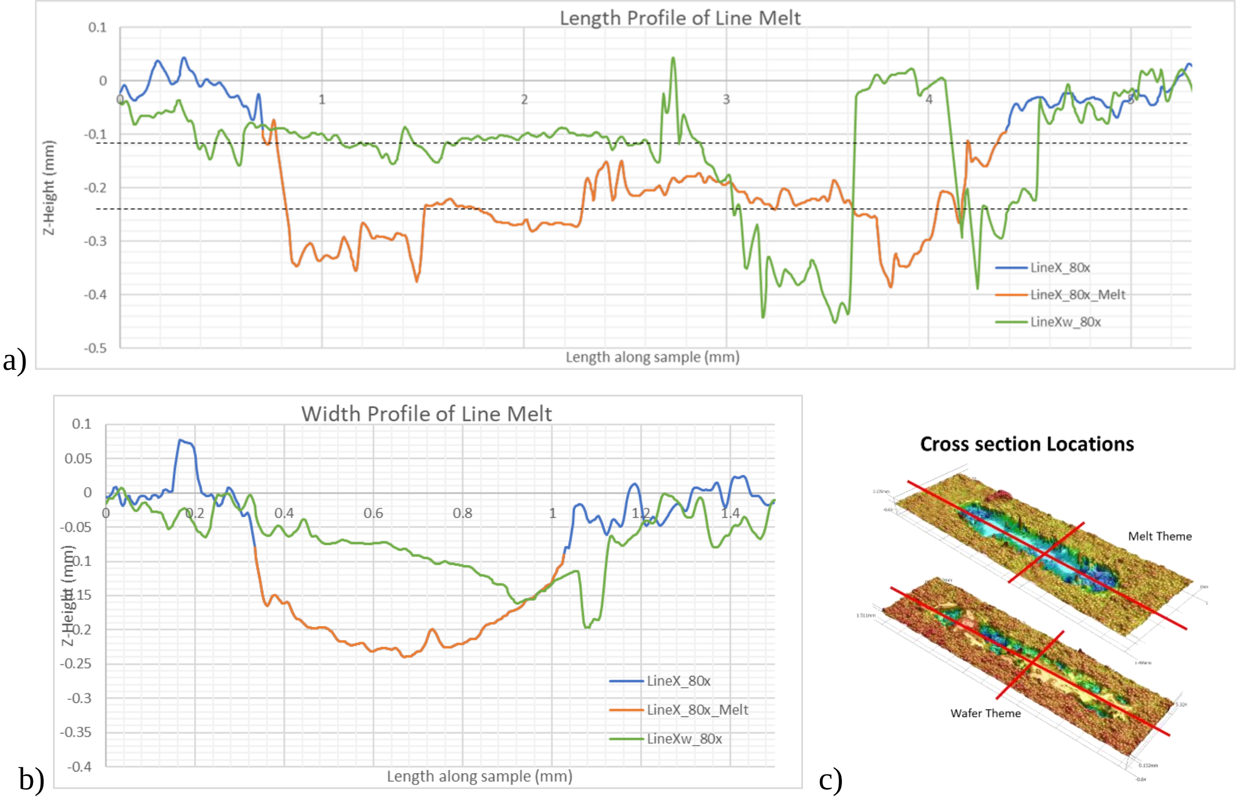

Figure 4.8. Line X cross section profile comparison of the melt (LineX, orange) and wafer (LineXw, green) themes in length (a), width (b), and cross section locations (c).

The specimen manufactured along the Y direction (Line Y) showed that there is very little difference from that of the Line X in terms of the appearance of both the melt and wafer themes as seen in Figure 4.9 and Figure 4.10. This melt theme specimen also shows the same over lapping circular spot melting pattern with two deep pockets, however the pockets are in the middle of the line and not on the ends like the deep pocket of Line X specimen. The average melt depth shown in Figure 4.10 was not as deep as the build depth of Line X at about 170 μm, though the pockets still reached as far as 400 μm below the powder bed. Similarly, the wafer theme melt in the Y direction was not as deep as the X direction measuring an average of 0.040 mm, or less than a single powder layer thickness. From the data collected it was difficult to determine where the melt began and ended due to the shallow melt depth. Geometrically the melt theme line was 3.765 mm long and 0.655 mm wide, while the wafer theme line was 4.232 mm in length and 0.616 mm wide. These values are very similar to the Line X geometric values.

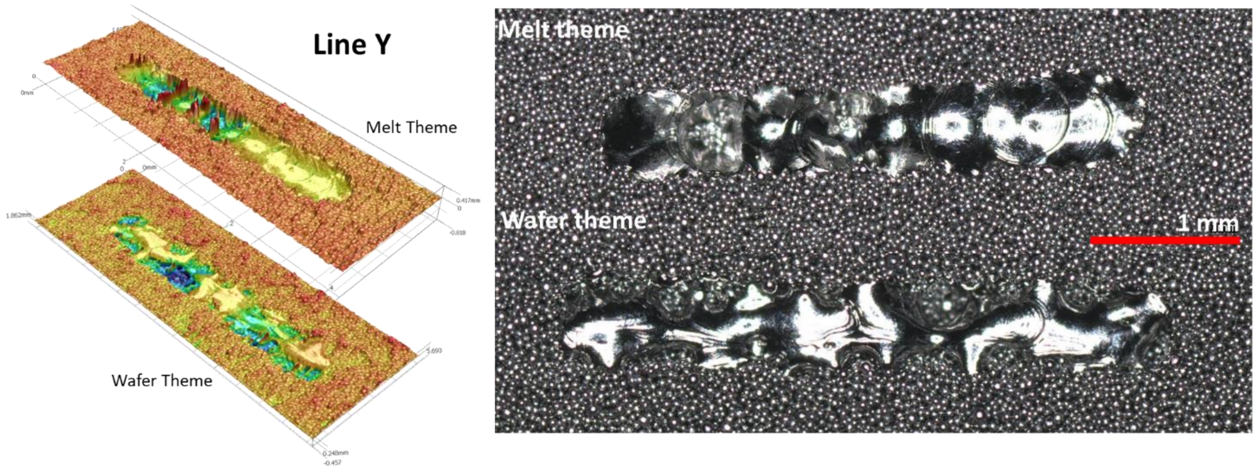

Figure 4.9. Image results of the Line Y melt and wafer theme specimens.

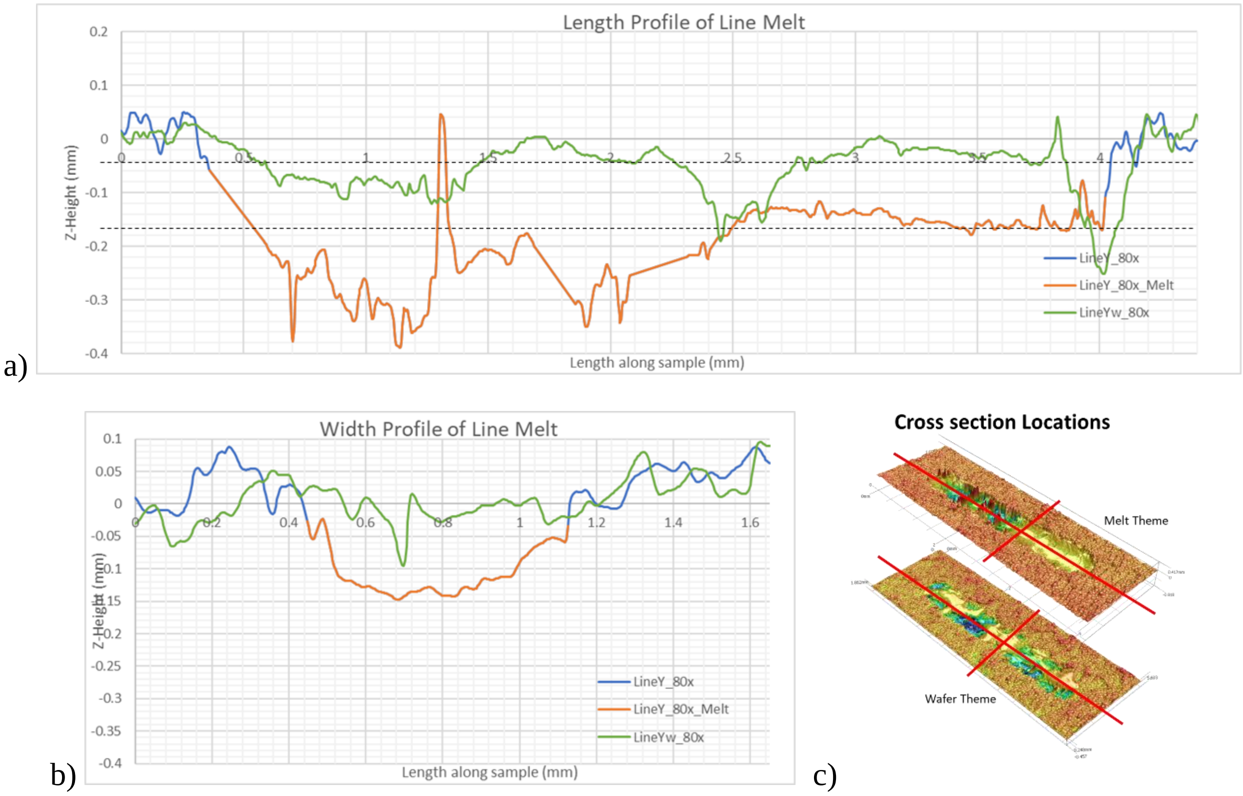

Figure 4.10. Line Y cross section profile comparison of the melt (LineY, orange) and wafer (LineYw, green) themes in length (a), width (b), and cross section locations (c).

Along the 45° direction relative to the X or Y lines, Figure 4.11 shows that there is very little difference in appearance to the other specimens. The melt theme line appears as overlapping circular melt pools with two deep pockets partially filled with unmelted powder. The locations of these pockets match the Line Y pockets as being nearer the middle of the melt line, rather than on the ends as in the case of the Line X. Ripples can also be seen along the edges of the melt pools which are concave in shape. The melt theme Line 45 measured 3.783 mm long and 0.691 mm wide, with an average depth at about 180 μm seen in Figure 4.12. For the wafer theme it appears as overlapping moving beam segments with ripples along the leading edge. Its overall shape is very irregular and almost random where the melt path seems to slightly meander. The melt depth is only about 50 μm, with a length of 4.105 mm and a width of 0.712 mm.

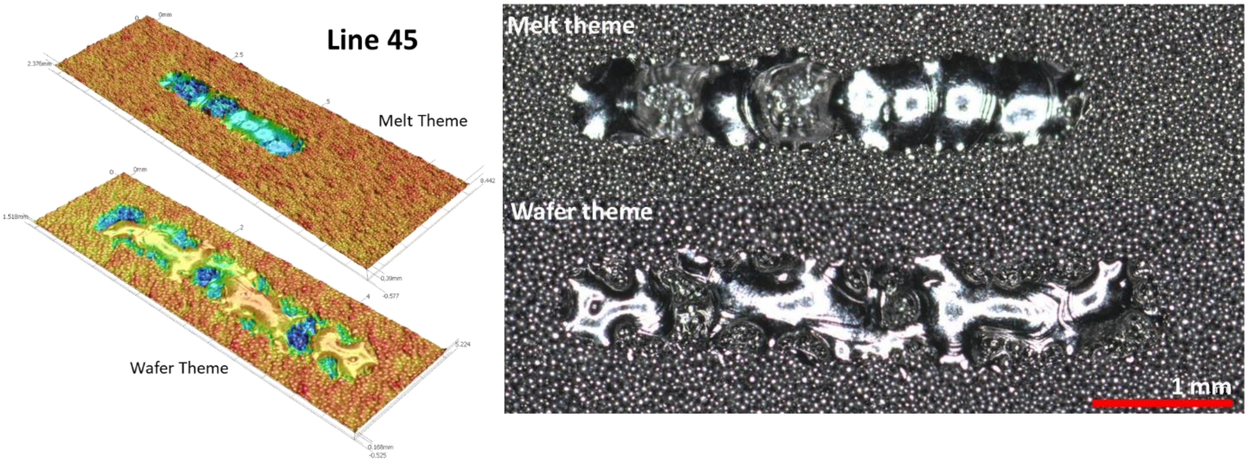

Figure 4.11. Image results of the Line 45 melt and wafer theme specimens.

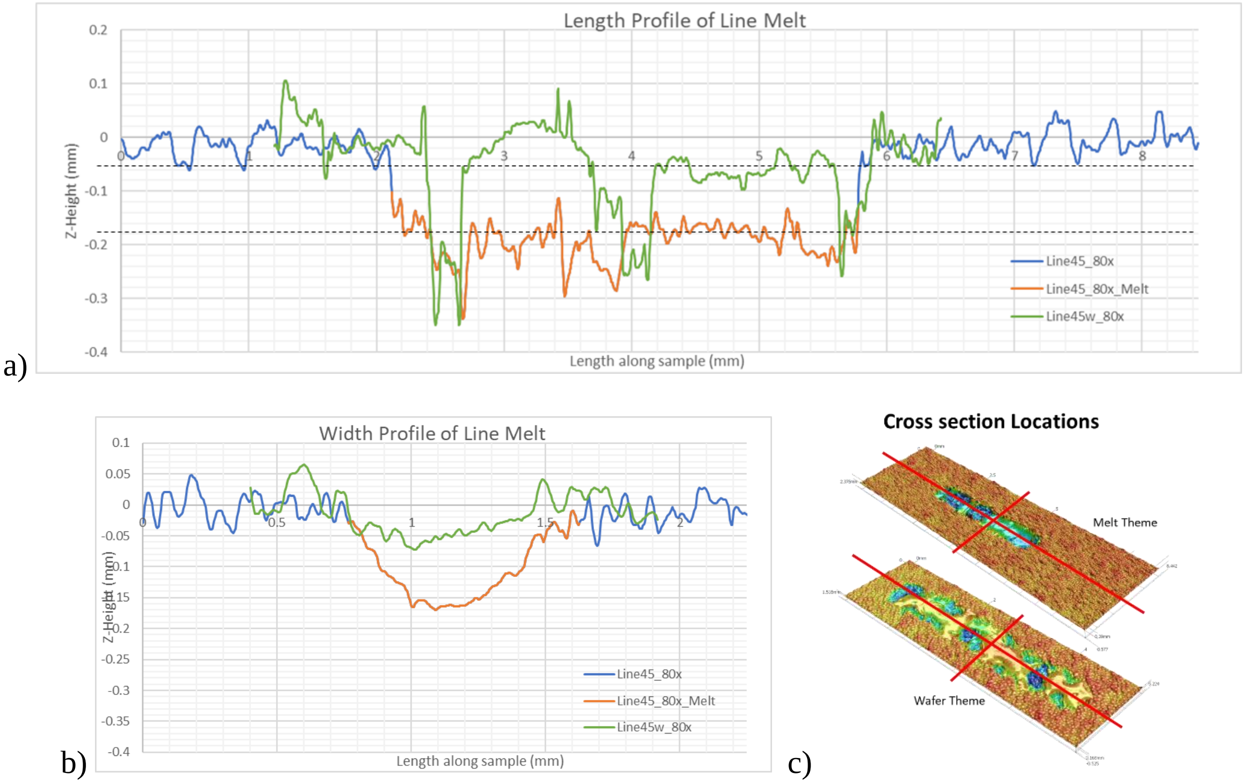

Figure 4.12. Line 45 cross section profile comparison of the melt (Line45, orange) and wafer (Line45w, green) themes in length (a), width (b), and cross section locations (c).

The melt theme for the Wall X artifact contained the same overlapping circular spot melt pools seen in the other specimens, however the definition is clearer than that of the single layer melt specimens and the wave-like ripples are much more pronounced and defined as shown in

Figure 4.13. Figure 4.14 shows the melt depth which has much less variation and lacks the deep pockets, while the profile measures essentially at the powder bed layer height, only about 0.025 mm deep. The topography is very flat and lacks the concavity shape of the single layer lines. This specimen measured the thinnest at only 0.603 mm wide with an average length of 3.758 mm.

The wafer theme for the Wall X specimen was also much more defined with less randomness in shape than the single layer wafer lines. The overlapping line melt segments show a good number of solidified ripples with some slight meandering. The depth of the line is nearly indistinguishable from the powder bed height at about 0.015 mm. The centerline of the melt path is raised enough that the edges drop off in a more convex width profile measuring 0.662 mm. At 4.357 mm, the wafer theme Wall X specimen is the longest of the eight specimens.

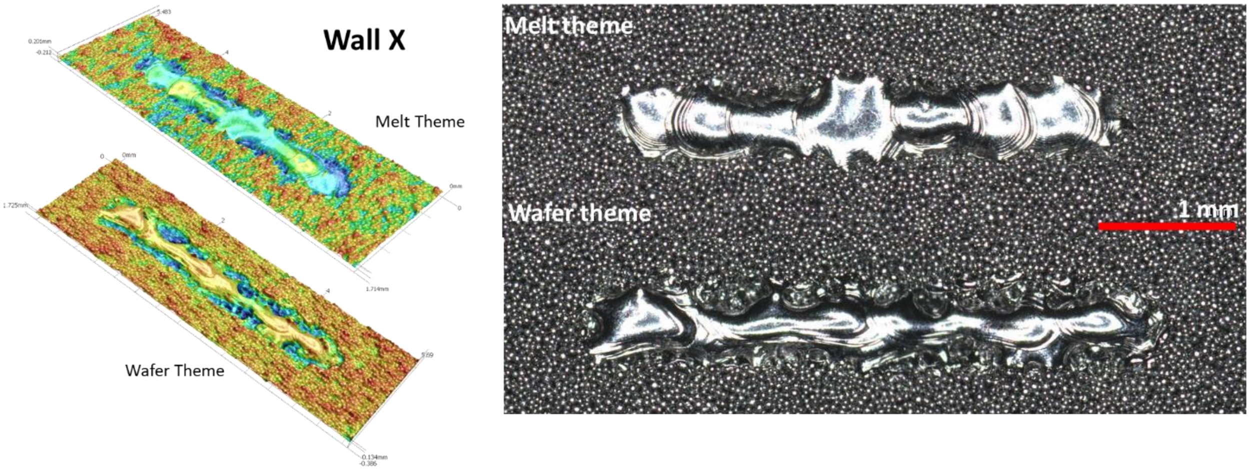

Figure 4.13. Image results of the Wall X melt and wafer theme specimens.

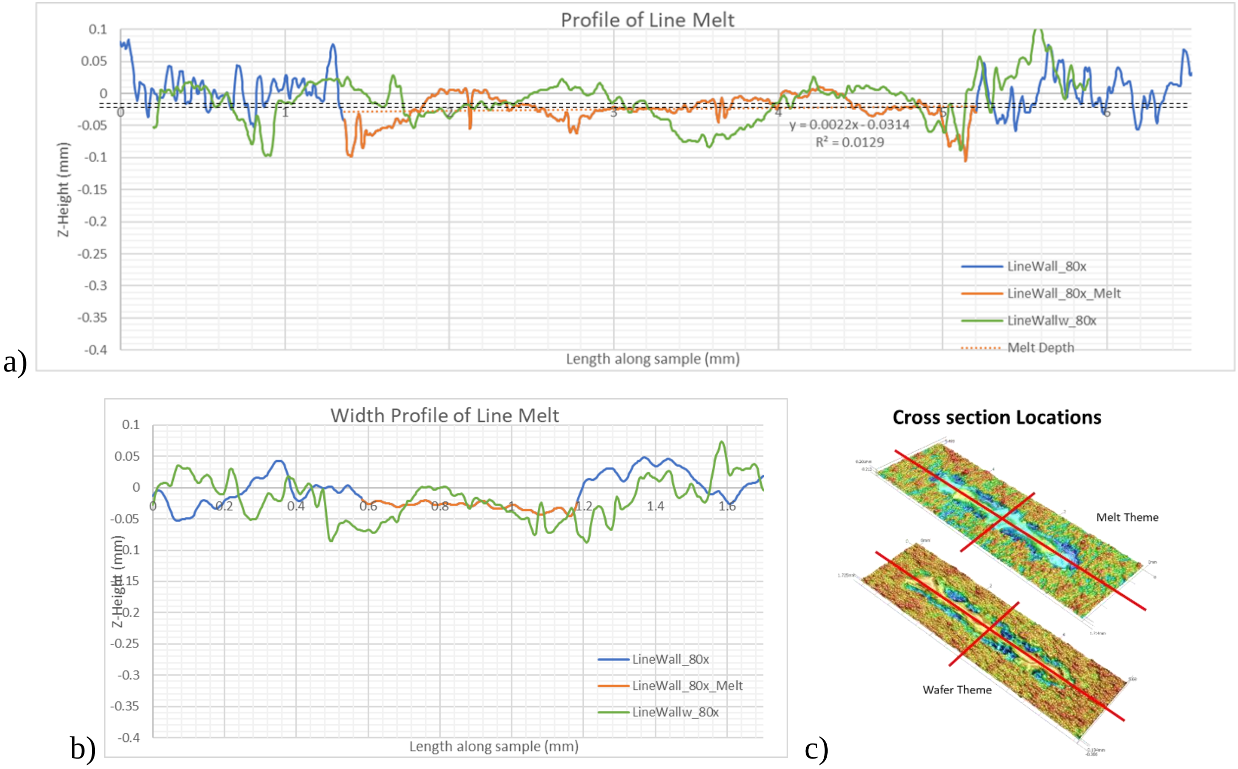

Figure 4.14. Wall X cross section profile comparison of the melt (LineWall, orange) and wafer (LineWallw, green) themes in length (a), width (b), and cross section locations (c).

The Line XY specimen for both the melt and wafer builds was not able to be adequately imaged, measured or analyzed. Despite it being successfully melted like the others, its position on the build plate relative to the Keyence imaging system platform made it so the plate was cantilevered in such a way as to be unstable for the imaging system; the platform was constantly shifting slowly as measurements were being taken. Nevertheless, one image was managed and show in Figure 4.15 but the quality of the topographical data was too poor to analyze. The single image was recorded of the central intersection between the X and Y lines from the wafer theme build. The center distinctly shows four overlapping line melts that continue off in their respective directions. The quality of the melted powder was similar to the other specimens which was very poor, even appearing to be discontinuous at one point with numerous pockets in both the X and Y melt lines filled in with unmelted powder.

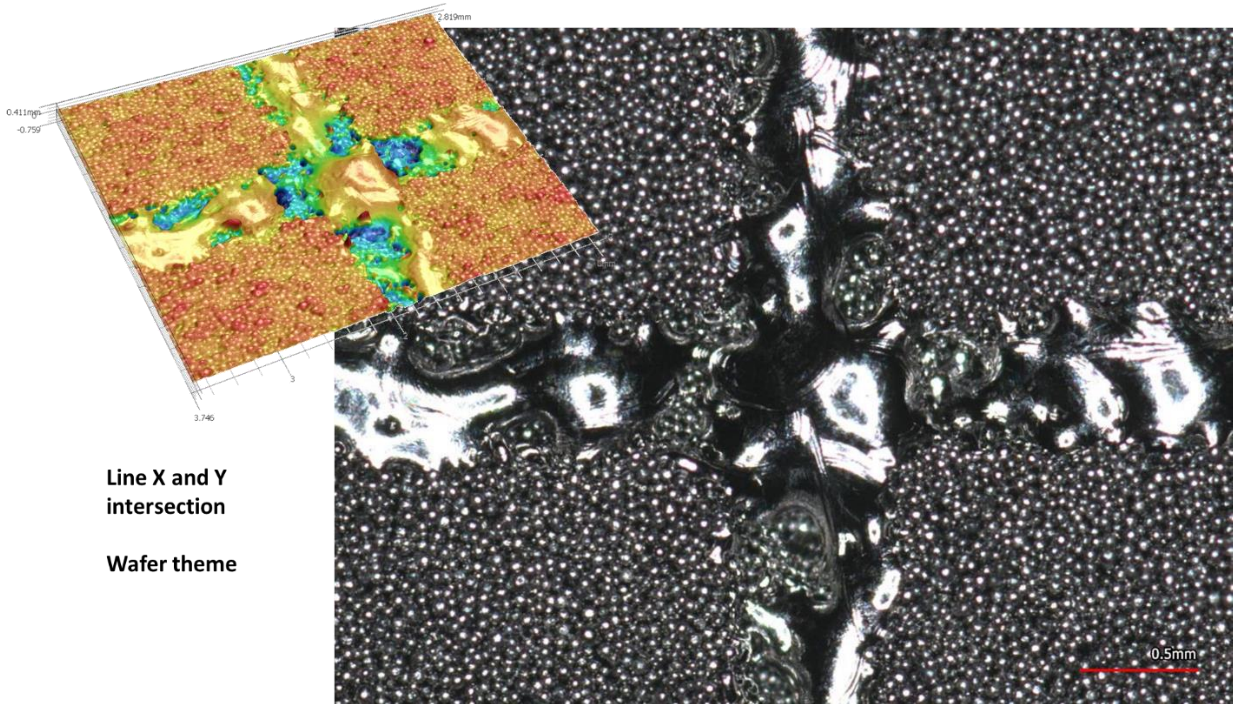

Figure 4.15. Intersection of Line X and Y with the wafer theme.

4.2.2 *Dimensional Accuracy*

When designing the CAD file, the assumption was that the melt theme would melt the specimen geometry as a moving heat source. What was discovered was a stationary overlapping spot melt pattern. The spots were identified and measured in Figure 4.16, this data is recorded in Table 4.5 for the Line Y, Line 45, and Wall X specimens (recall the quality of the Line X image was too poor); however, it is possible there were more overlapping spot melts than could be identified. It is not clear why a spot melting pattern was used for lines that employed the melt theme.

Table 4.5. Average spot melting dimensions by specimen.

	Line Y melt	Line 45 melt	Wall X melt	Global
# of spots	9	9	10	9
Avg Radius	0.289 mm	0.306 mm	0.248 mm	0.281 mm
Avg Spacing	0.385 mm	0.391 mm	0.344 mm	0.373 mm

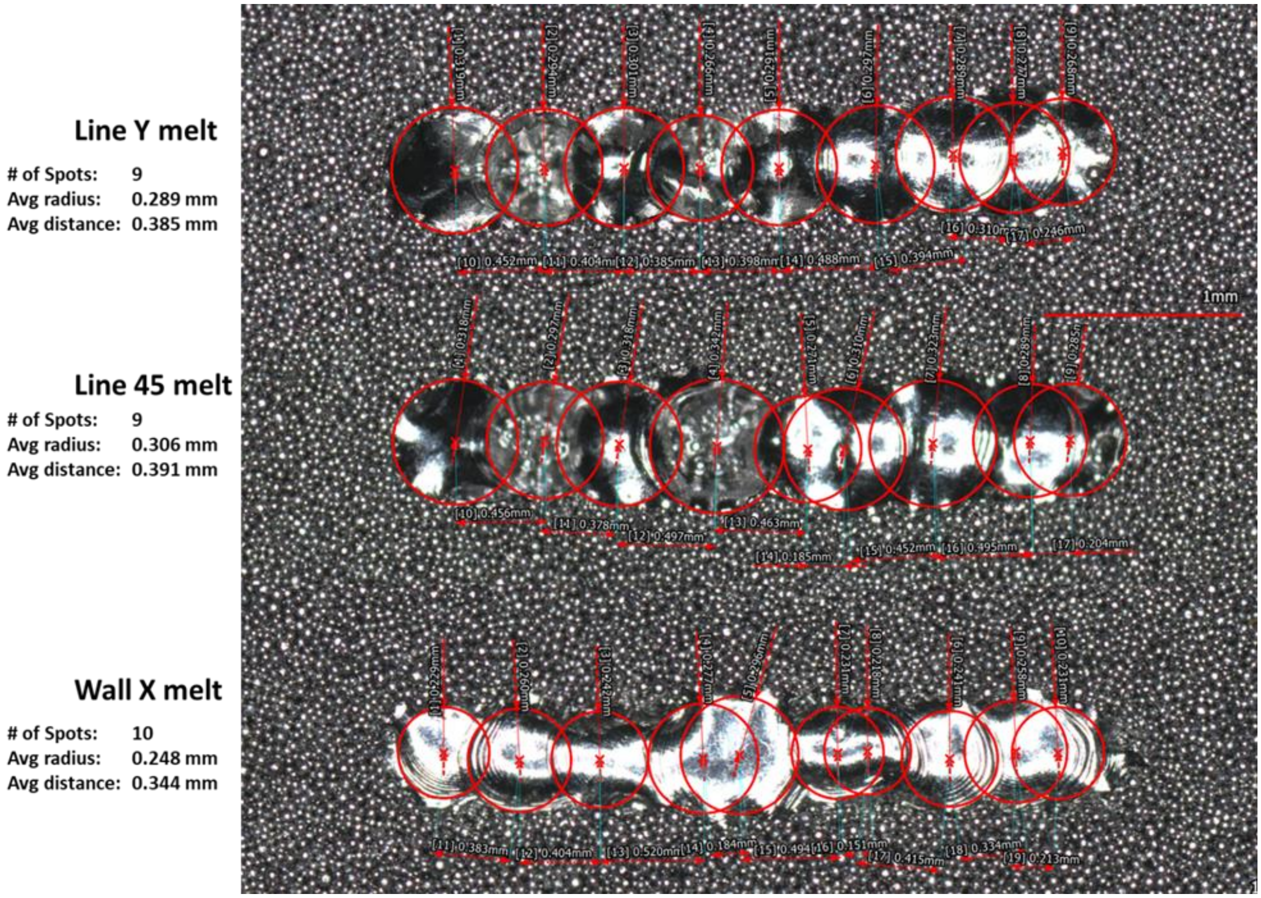

Figure 4.16. Spot melt size measurements.

The width and length of all eight specimens was measured and compared in Figure 4.17 and Figure 4.18 respectively. From the figures, the target line width and line length are denoted by the dotted and dashed lines respectively. It is clear from this view that for the line width, all of the specimens were greater than the 0.4 mm CAD specification which was expected since the CAD was undersized to ensure a single line melt. There was no difference between the melt and wafer themes in terms of melt width indicating that the smallest feature, a single bead melt, will vary from 0.6 to 0.7 mm. When it comes to line length there was a significant difference between the two themes. The melt theme lines were all under the specified 4 mm by at least 0.2 mm, while all of the wafer theme lines were over by a minimum of 0.1 mm. The wafer theme showed a wide variation in length from about 0.10 to 0.35. The scatter for the melt theme showed a higher degree of accuracy and control where the lengths were all within 0.10 mm of each other.

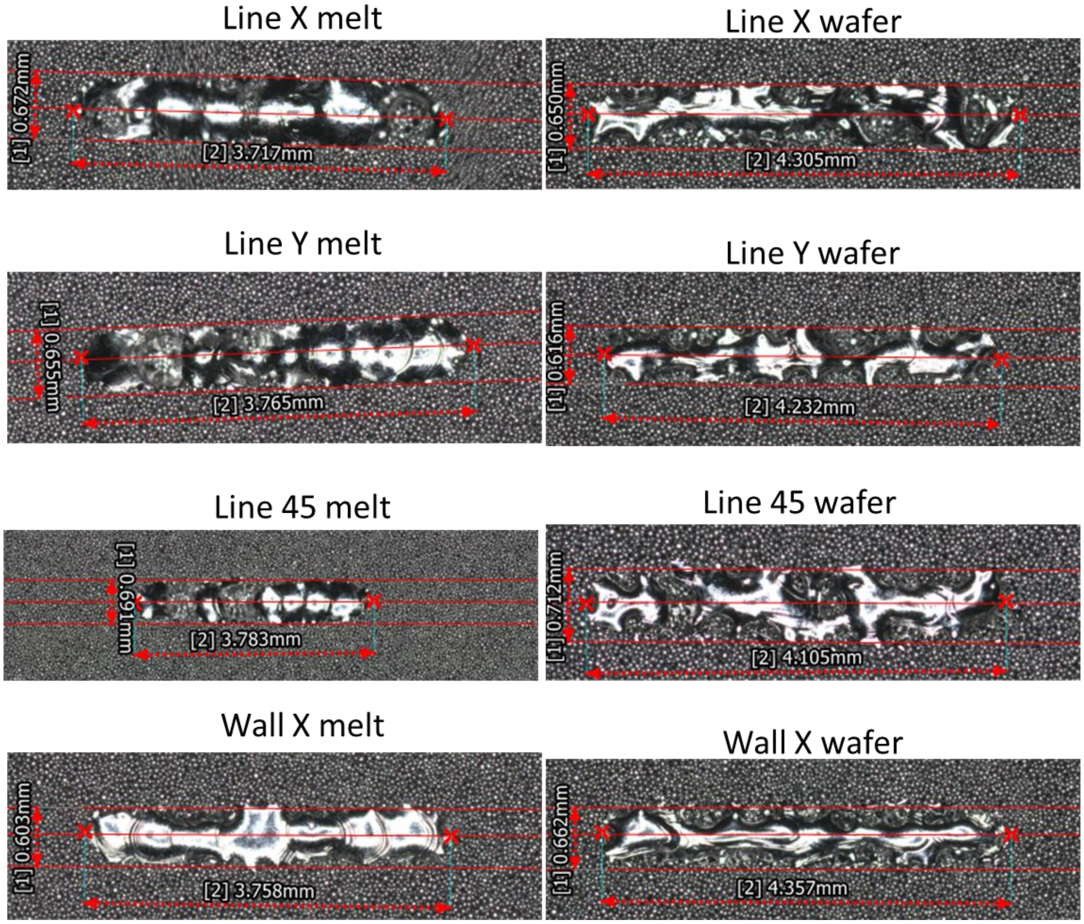

Figure 4.17. Measurements of length and width of the melt lines for the melt and wafer themes.

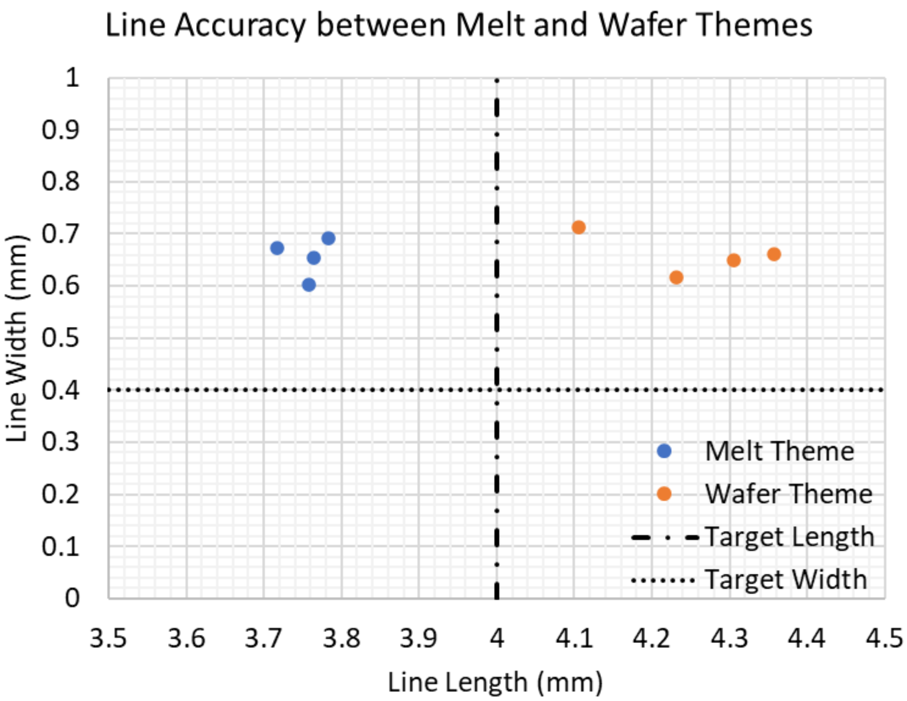

Figure 4.18. Comparison of the accuracy of each line melt in relation to the CAD model target.

4.3 DISCUSSION

Based on the comparison the two scan strategies, it is obvious that the default melt theme is using a spot melting pattern (stationary heat source) versus the line melting (moving heat source) of the wafer theme. Even the line melting wafer did not travel the full specimen, but was run in very short overlapping segments. This identification of spot melting is different than the initial hypothesis which specified a moving heat source. This should mean that a FEM analytical modelling of the melt theme should consider processing a simulation with a stationary spot melting heat source. The spot melting contour scan strategy also means an as-built smooth surface is impossible as was previously diagramed in Figure 4.7 and shown in Figure 4.19 from Sames et. al [1]. Under the microscope the boarders of both default melt themes with all specimens were very chaotic and random which is not an indication of optimized process parameters.

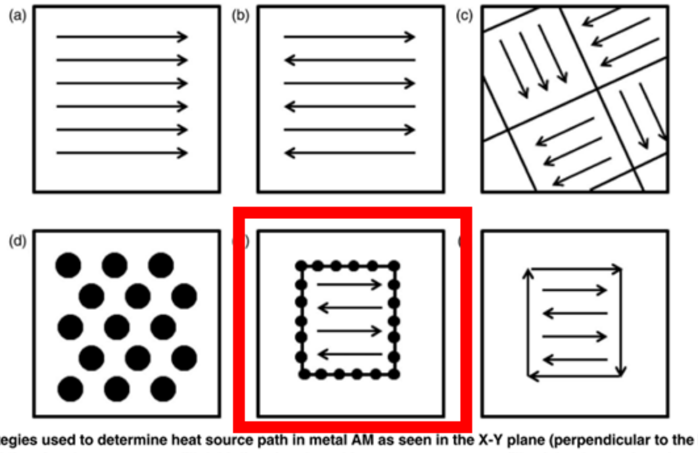

16 Scan strategies used to determine heat source path in metal AM as seen in the X-Y plane (perpendicular to the build direction): *a* unidirectional or concurrent fill, *b* bi-directional, snaking, or countercurrent fill, *c* island scanning, *d* spot melting, *e* spot melting contours with snaking fill and *f* line melting contours with snaking fill

Figure 4.19. Diagram of different scan strategies with the Arcam default melt theme strategy highlighted [1].

Another unexpected finding is the solidified ripples and waves in the melted areas where closeup images are shown in Figure 4.20. Arcam states that the beam spot size for the Arcam A2X is 0.25 mm, which is nearly 2.5 times smaller than the spot melt it creates. The ripples suggest a pulsing of energy, all of which happens in a fraction of a second and is captured in the specimen as a result of the rapid cooling of the part builds.

The different Line specimens represent what is happening on unsupported down skin areas. They reveal just how poor the melting results are with the default parameters and provide insight into sources of porosity and surface roughness. From this perspective, a designer will need to consider build orientation when analyzing whether any down skin surfaces are critical to the component, and if so either 1) provide generous support structures in the previous layers, or 2) ensure no critical loads are passing through that section of the part, or 3) provide additional thickness to compensate for the area that will contain increased porosity and reduced strength, or 4) plan to post process and remove a thickness of about 0.4 mm from the unsupported down skin surface.

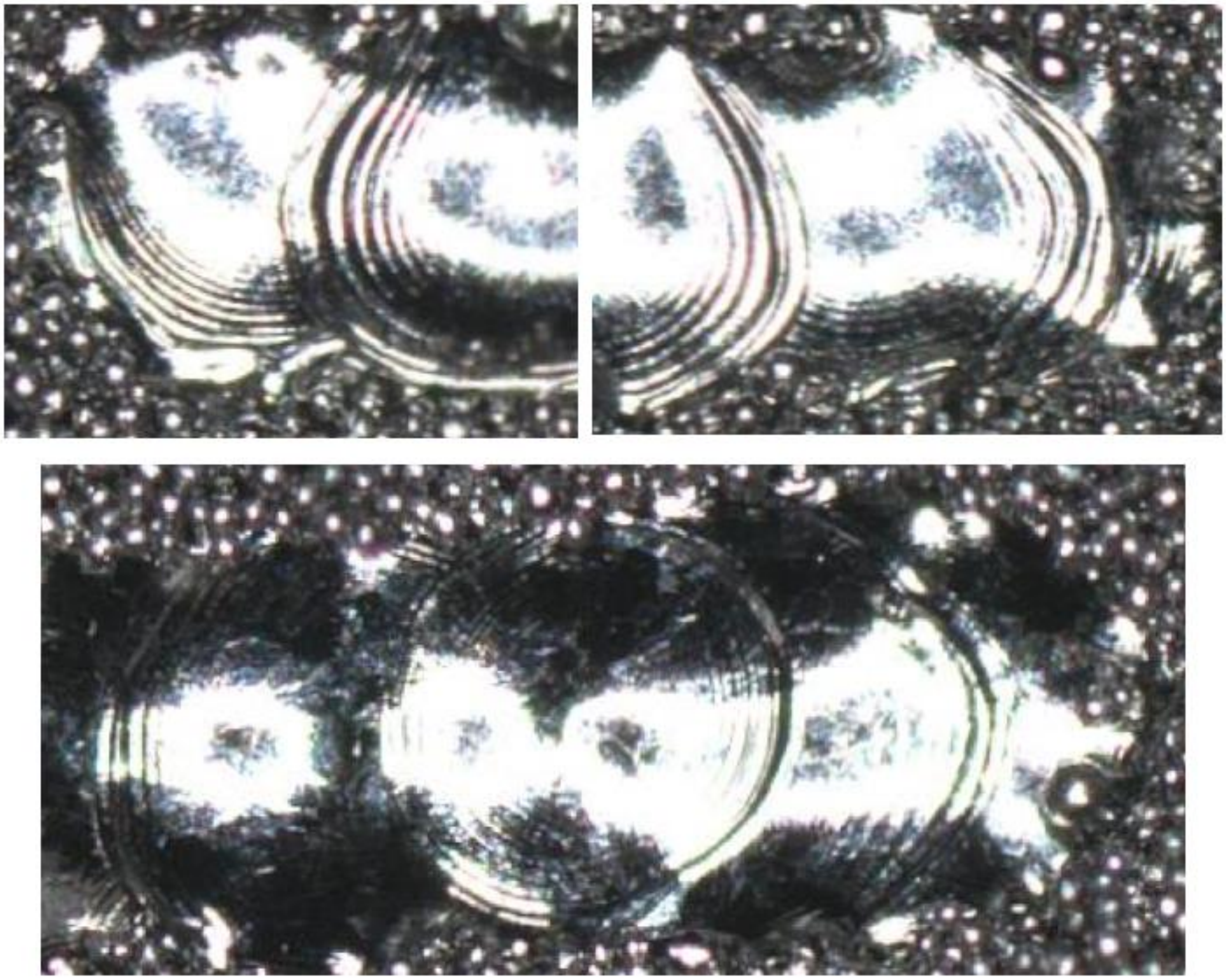

Figure 4.20. Images of ripples seen in various melt specimens

Chapter 5. STEP-RAMP EXPERIMENT

When additively manufacturing complex geometry with a metal PBF machine, the desire is for the process to be repeatable such that multiples of the same geometry will result in the same dimensions within some designated tolerance. Some level of variability, part distortion, and warpage, is anticipated during a metal AM build, regardless of whether the energy source is laser or electron beam. An experiment was conducted where a build contained a set of four different CAD geometries that were repeated four times throughout the build chamber for a total of 16 specimens. An Arcam A2X EBM machine was utilized to fabricate the step and ramp geometries shown in Figure 5.1.

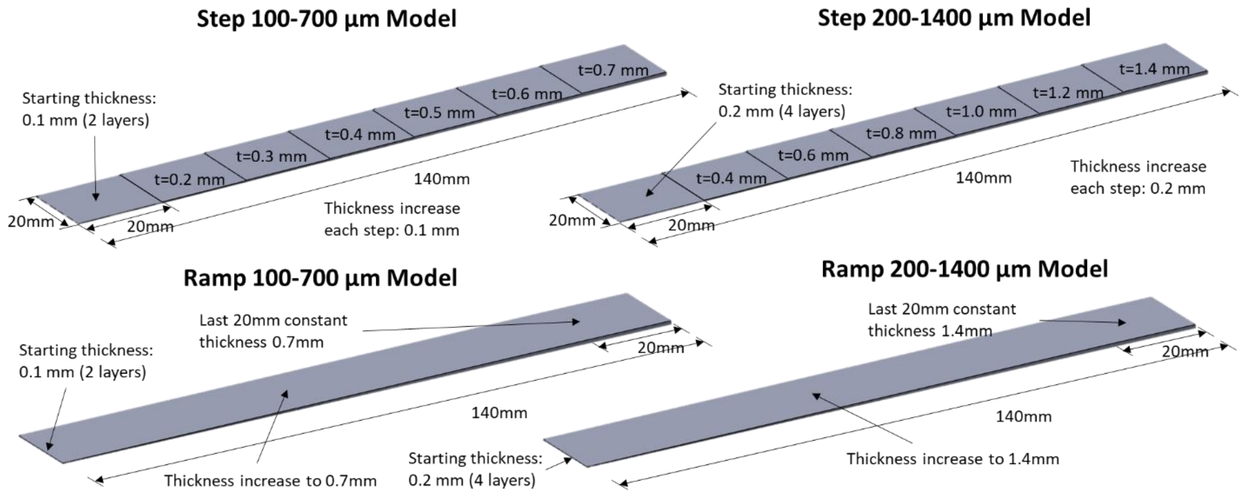

Figure 5.1. Design of Step and Ramp specimens.

5.1 METHODS

The CAD models consisted of four very thin specimens of non-constant thickness that were repeated four times at different X-Y locations and Z heights. In the corners two cones and two circular pyramids were also placed for other evaluations. Of the four different models, two resembled steps with discrete increases in thickness and the other two were ramps with a continuously variable thickness.

Each set of two steps or two ramps came in different thicknesses where the first Step-Ramp pair varied in height from 100 μm to 700 μm, and the second Step-Ramp pair varied in height from 200 μm to 1400 μm. The thinner ramp thicknesses continuously increased over the span of 120 mm until reaching 700 μm, while the step geometries were seven 20 x 20 mm square steps in thickness increments of 100 μm. The starting thickness values were selected because they are significant to the Arcam A2X machine which specifies a layer thickness of 50 μm, therefore 100 μm represents two printed layers. The thicker specimens spanned the same 140 mm total length, but increased their thickness by 200 μm (four layers) at a time.

5.1.1 *Specimen and Build Design*

The first set of four specimens were lined up side by side, located 5 mm above the 210 x 210 mm stainless steel start plate with downskin surface supports extending to the plate. That same model setup was repeated adjacently, but started at 7 mm above the start plate with supports extending to the start plate. That same pattern of eight total specimens was repeated at a higher location in the build, starting at 18.4 mm, rotated 90 degrees, and each specimen with supports extending 5 mm into the sintered powder below. The upper specimen supports did not extend to any other structures or the start plate so they were "floating" on the sintered powder. Extending the supports 5 mm into the powder was expected to not be enough to counter any thermal warping, however, it was chosen to be the same as the first set in order to highlight the differences in the result. The lower (L) specimens are numbered L1 through L8, while the upper (U) specimens are numbered U1 through U8. The odd numbers are Ramp models while the even numbers are Step models;

Figure 5.1 and Table 5.6 and specify the specimen designs nomenclature. Figure 5.2 shows how the specimens were arranged in the build chamber.

Table 5.6. Nomenclature for specimen identification

Lower ID #	Config	Thickness (μm)	Z start (mm)	Length (mm)	Upper ID #	Config	Thickness (μm)	Z start (mm)	Length (mm)
L1	Ramp	100-700	5	140	U1	Ramp	100-700	18.4	140
L2	Step	100-700	5	140	U2	Step	100-700	18.4	140
L3	Ramp	200-1400	5	140	U3	Ramp	200-1400	18.4	140
L4	Step	200-1400	5	140	U4	Step	200-1400	18.4	140
L5	Ramp	100-700	7	140	U5	Ramp	100-700	20.4	140
L6	Step	100-700	7	140	U6	Step	100-700	20.4	140
L7	Ramp	200-1400	7	140	U7	Ramp	200-1400	20.4	140
L8	Step	200-1400	7	140	U8	Step	200-1400	20.4	140

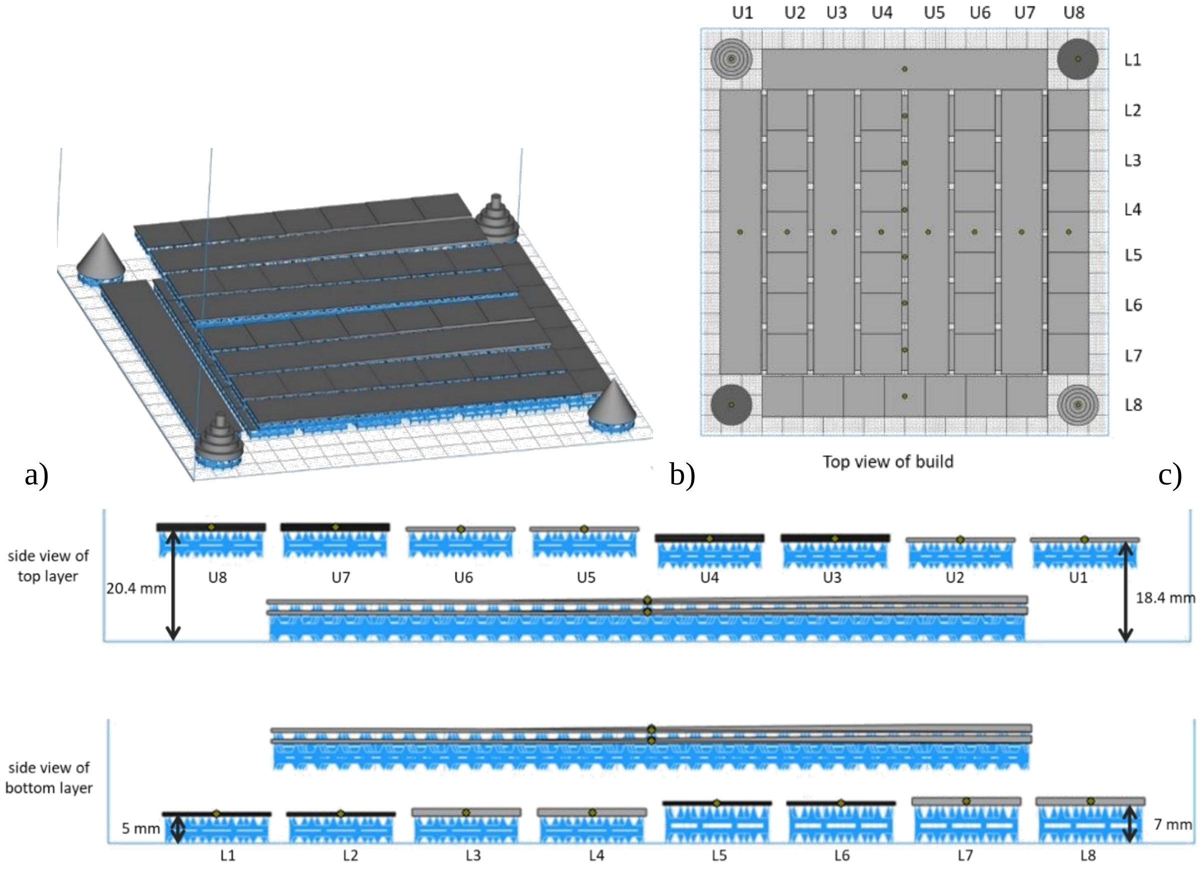

Figure 5.2. Isometric (a), Top (b), and side (c) views of the build configuration; The test specimens are shown in grey and the support structures are colored blue.

5.1.2 *Machine Setup*

The Arcam A2X was set up with used Ti-6-4 Arcam powder of unknown pedigree, and default Arcam themes for preheating, wafer supports, and melting parts. Total build height was 21.8 mm and the estimated build time was 3 hours 59 minutes. Despite initial expectations that printing such thin components might distort enough to crash the build, it did complete successfully. When melting was completed on the final layer, the time from initial heating to build complete was 4 hours 36 minutes with a 4 hour cool down to 80 degrees C. From the time the vacuum pumps were turned on to cooling complete the total process time was 9 hours 39 minutes, with 4 hours 6 minutes of melting followed by 3 hours 10 minutes of cooling to 100 °C as shown in Figure 5.3. The initial cooling rate was 6 °C/min and over time ended at a rate of 0.4 °C/min.

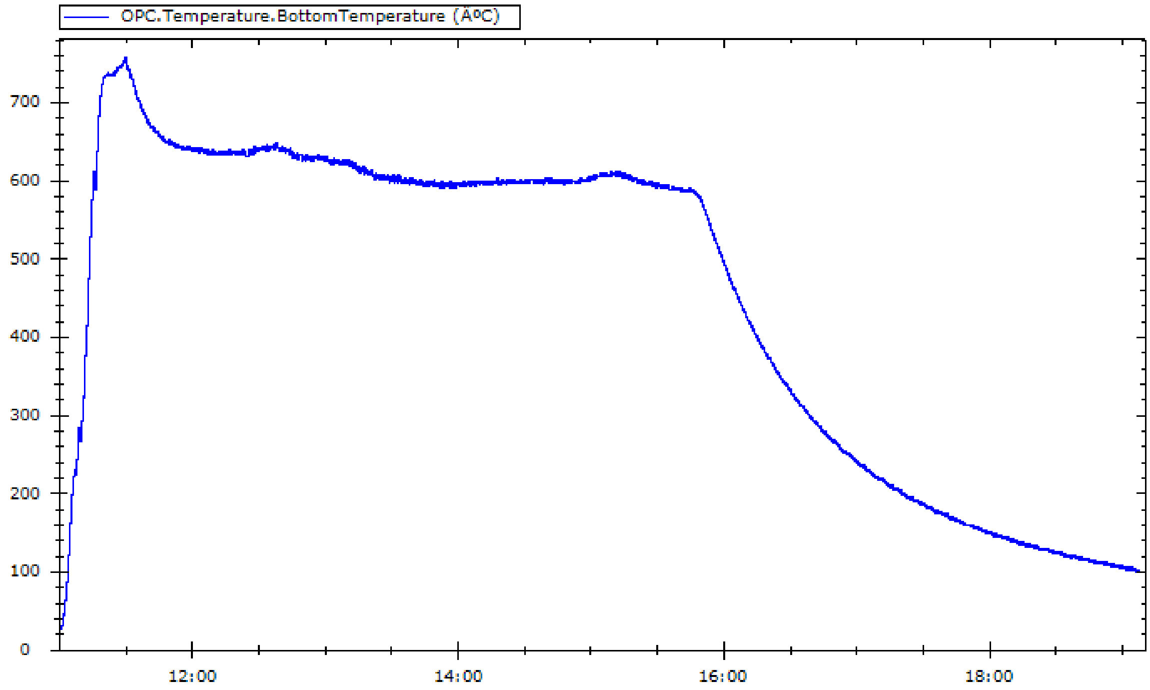

Figure 5.3. Temperature profile of Step-Ramp build as recorded by the thermocouple under the build plate.

5.2 RESULTS

Just prior to the build being extracted, it was observed that small portions of the last series of specimens were protruding out of the powder bed build plane. This is perhaps an indication that had the build continued to make more specimens, they might have eventually interfered with the powder distribution rake and caused the build to crash. Upon inspection no damage was observed to the rake teeth nor was the powder bed surface non-uniform. That could also indicate that the specimens did not distort out of the build plane while the build was at the elevated temperature, but instead distorted after the build was complete during the cool down cycle.

Once the chamber door was open, the sintered build cake was removed from the chamber, transferred to the Powder Recovery System, and the build chamber was cleaned all per the Arcam User Manual process. Care was taken to remove the specimens from the titanium powder cake so they could be labeled with their location identifier. A red Sharpie was used to place a mark on the upward facing surface just below the top layer of the specimen. It is well known that the software Materialise Magics which was used for the build setup can add labels that would be printed into specimens for identification; however, this was not done because the specimens were too thin and lettering would have disturbed the desired default contour and hatching process.

The specimen upper surfaces were imaged with a Keyence VR-3100 wide-area 3D measurement system that uses fringe projection to optically measure the surface topography. This not only takes optical images of the surface, but also measures the height for a three-dimensional view of the specimen. The specimens were too long to capture in a single image with this device, so they were meticulously handled in order to stitch several images together for a full picture of each one. There is still some question as to whether the stitching of the image data could be a source of some of the variation observed in the analysis.

5.2.1 *Visual Observations*

The first set of specimens L1 through L4 top surfaces were imaged and set side by side for comparison with the thickness of the layers indicated in Figure 5.4. Visually it appears that the ramp specimens L1 and L3 turned out very well with a shallow enough slope to be able to clearly identify the staircase effect of the layering process as well as the hatching pattern and angle of each layer. This is contrasted with the step specimens L2 and L4 that had large square melt areas. The thinnest areas of L1 and L2 which are only two layers thick show an enormous quantity of pores, many have partially melted or sintered powder inside which is seen in Figure 5.5. The thinnest areas of L3 and L4 have only a few pores because they are four layers thick and can be directly compared with the 200 μm levels in L1 and L2. Moving up in designed thickness random pores are still present in various specimens and layers. Often times these pores coincide with the stopping or starting of a hatching scan or more commonly exist at the intersection of the contour and hatch scans.

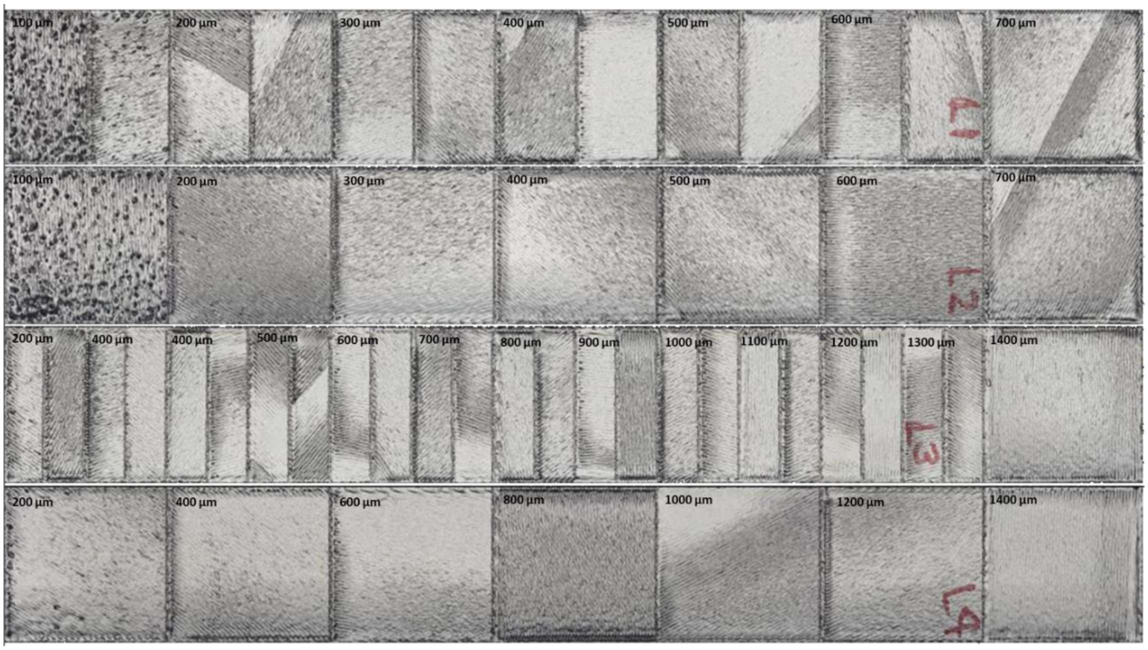

Figure 5.4. Set 1 of step and ramp parts, specimens L1 through L4 from top to bottom with the designed thickness indicated in black text.

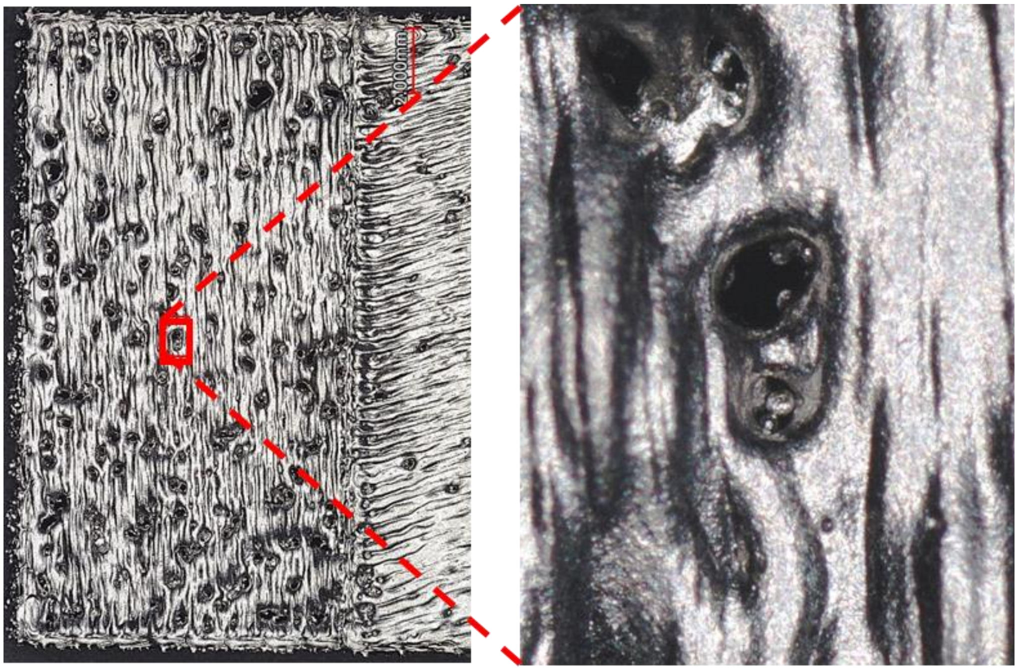

Figure 5.5. Image of L1 layer 1, 100 µm thickness, pore location (left) and 160x showing unmelted powder.

The contoured edges on all layers and specimens were raised slightly relative to the same layer hatching area. There is significant melt disturbance and number of pores around the intersection of the hatching and contouring melts on every layer. This is likely the cause for the well noted near-surface-porosity encountered in other literature [12]. There was also a lack of uniformity of the hatching pattern at every layer on every specimen. Some hatch lines appeared to be well melted and wide while a few millimeters adjacent the lines are so thin they appear to not even be touching the adjacent lines. A number of hatch lines are also not straight and tend to meander randomly.

Optically, the shading within any given layer reveals that very few appear to have a completely uniform melt despite a constant thermal mass. The 450 µm layer of L1 and L3 appear to have the most uniform melt. On other layers there exists a significant contrast in the hatch scan melt that appear as stripes. The ramp specimens L1 and L3 seem to have the most substantial striping and largest number of occurrences. At the 200 μm and 250 μm levels of L1 this effect is clearly visible, and again at the 400, 500, 550, 650, and 700 μm. Figure 5.6 shows a 40x optical image of L3 at layer 8 (550 μm design thickness) at the boundary of the melt stripe. It is not known why the change in melting is so distinct and random. The step specimens L2 and L4 show more gradual changes in shading without the obvious stripes, except for the 700 μm level of L2 that seems to have a continuation of the stripe identified at the same thickness on L1 which was immediately adjacent to it.

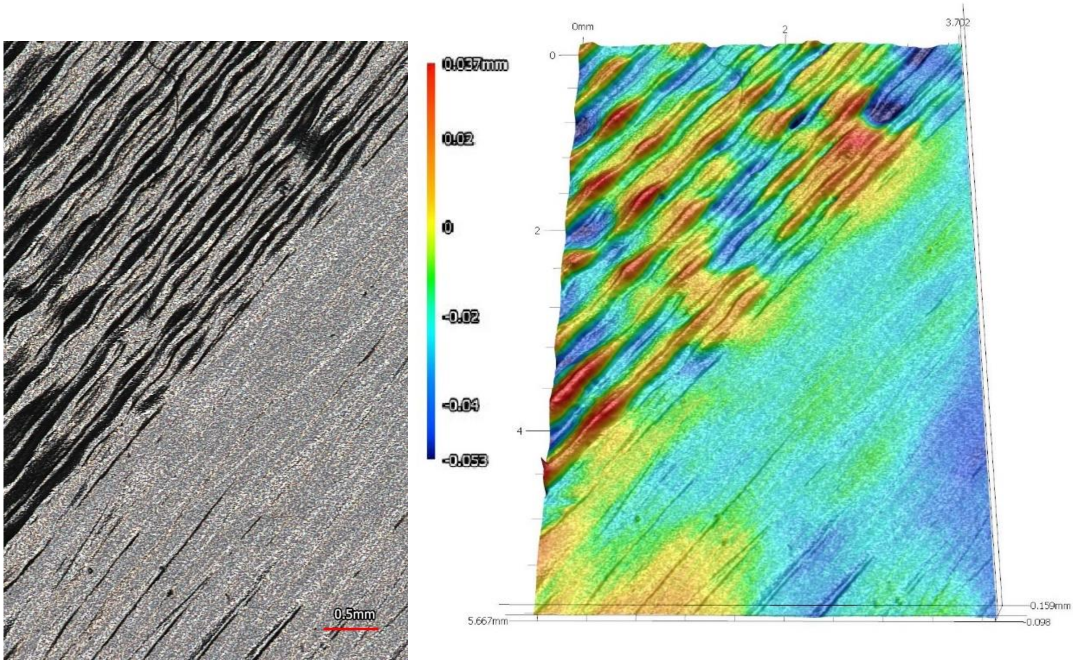

Figure 5.6. L3 Layer 8 (550 μm design thickness) 40x optical image (left) and 3D height data image (right).

An important observation to note is that the hatch angles between L1 and L2 at the 400 μm level appear to be perpendicular to each other. From Figure 5.2 those specimens were adjacent to one another on the start plate a few millimeters apart. Another significant difference in hatch angle can be identified at the 1200 μm level of L3 and L4, though the difference is not as big. Other intralayer hatch angle changes were observed on other specimens so this was looked at in more detail in Section 5.2.3.

Another hatching discrepancy appears as a change in the same hatch line of a layer, not just adjacent lines. For example, the 600 μm level of L1 and L2 goes abruptly from light to dark as the hatch lines go from left to right in the direction of the hatch. This implies that the beam parameters are changing rapidly depending on the location of the melt area. There is no difference in thickness across the layer, but perhaps this is an effect of additional heat interaction with the contour scan melt region.

When all sixteen specimens are compared some of the same trends are apparent. Figure 5.7 groups all the same CAD models together, e.g. all four of the thin ramps L1, L5, U1, and U5 are placed adjacent to each other. The major takeaway is that despite the CAD geometry being identical, the specimens are not. What one should see is a gradual change from blue to red in each specimen as L1 and L3 display in image (a), yet those are the only two specimens that exhibit that color scheme. The primary cause is thought to be the rotation of the hatching angle. This parameter, while meant to reduce residual stress and stress induced distortion, could be inducing its own distortion based on how it is implemented. This shows that even identical parts placed at different locations within the build chamber will not be the same, that each one is in fact unique with a different hatching angle history.

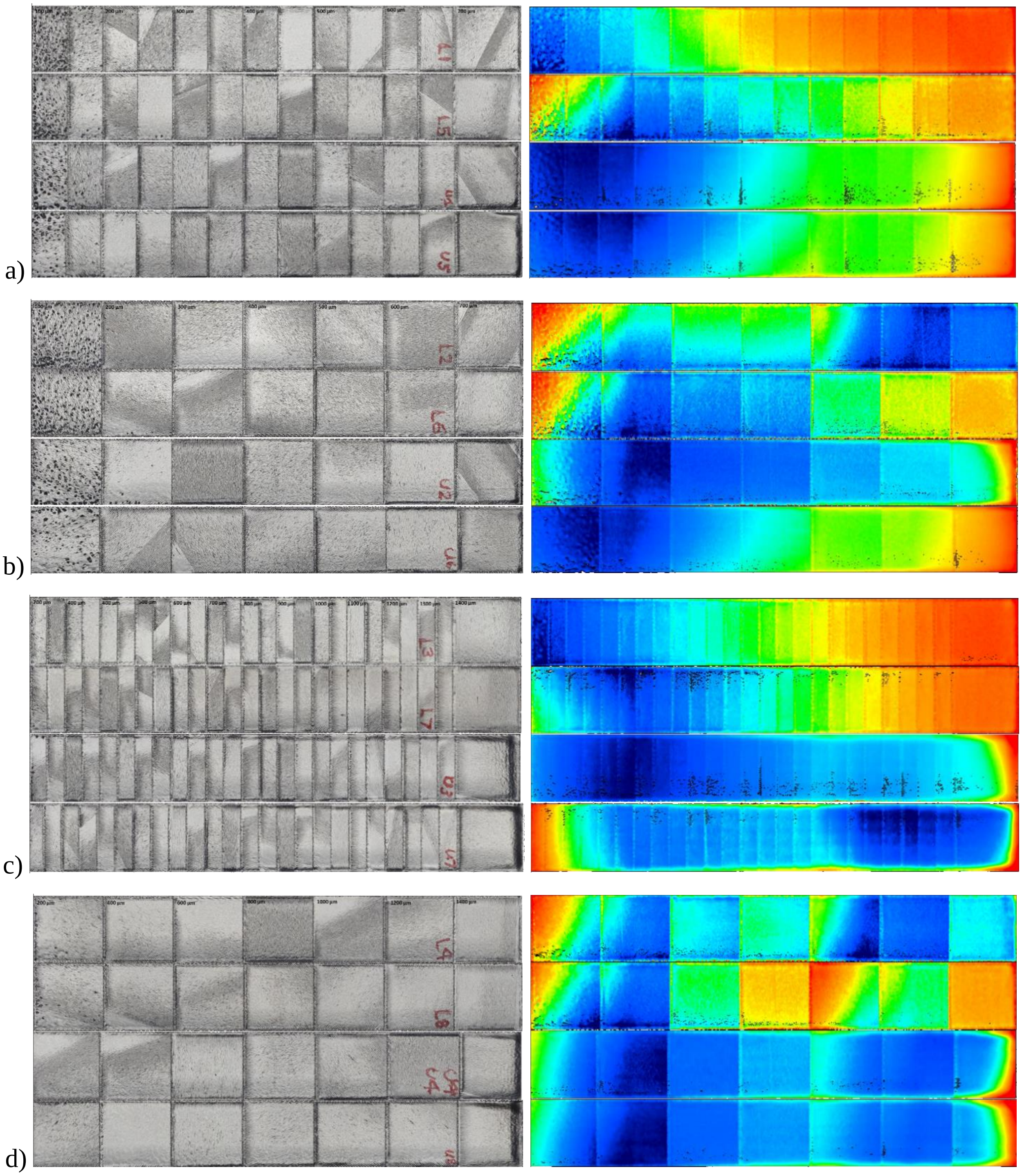

Figure 5.7. Optical (left) and height (right, scales not the same) comparison images of all four sets of specimens: thin ramp specimens (a), thin step (b), thick ramp (c) and thick step (d).

The high surface roughness of EBM components is well documented in literature [1,5-6,12]. An attempt was made to measure the thickness of the specimens by imaging and measuring the profile from the side. However, as Figure 5.8 shows the terrible surface roughness made such an endeavor impossible. The upper edge of the contour scan is so wavy it is like waves in the ocean crashing upon the shore. The lower surface appears as irregular as a mountain range. There is no value in measuring the side profiles of these specimens so they will be sectioned in future work. A notable feature of the surface is all of the partially melted powder particles stuck to the melt area.

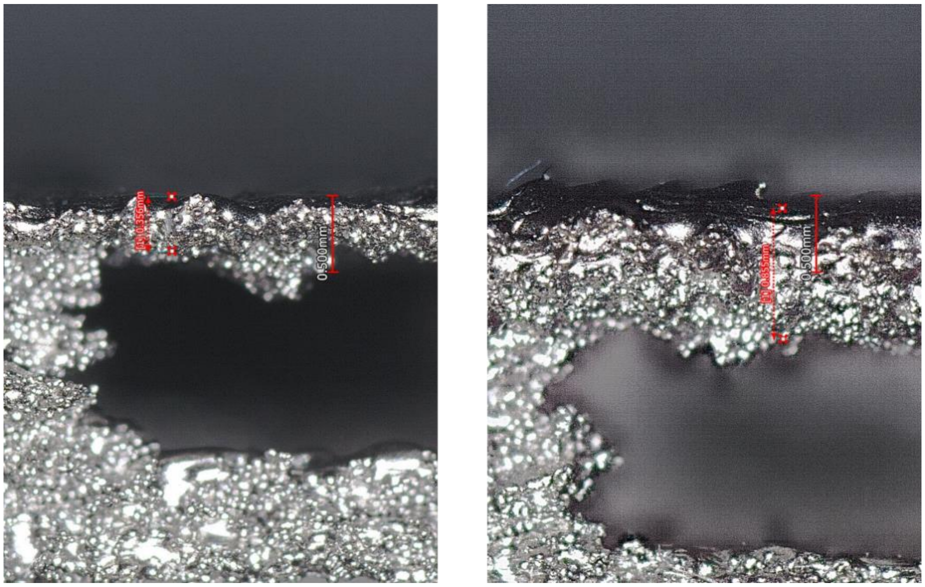

Figure 5.8. Side of L1 specimen thin end (left) and thick end (right).

5.2.2 *Topological Profile Analysis*

The image and height data was analyzed to extract a topological profile of the specimens along their length. The purpose being to compare the measured height with the CAD files to characterize the level of distortion. A difficulty encountered was that the specimens contained no perfectly flat regions with which to calibrate a zero plane. Several areas were attempted to see which calibration plane yielded decent comparisons for the various specimens. For the lower specimens L1-8, the top upper layer surface was used to calibrate a zero plane. The level of distortion in the same top layer regions of the upper specimens was too great to get an adequate zero, so for the upper specimens the 600 μm thickness layer was chosen as the zero plane for U1-8.

Some general observations of the traces are that the layer edges are denoted by a spike in height where the contour scan produces a raised ridge around the border of the melted regions. The spikes are very regular along the length X-Y directions of the parts indicating decent geometric accuracy for the location of the specimen boundaries. The specimens were all fairly distorted in the z-direction and the only one to closely match the expected CAD geometry was the lower thick ramp L3. From the profile traces and from the images, it was observed that the thinnest layers showed significantly more variation in the surface profile due to the lack of thermal mass, but that after the first couple layers the remaining layers were mostly uniform in the hatched regions.

The specimen profile traces are plotted relative to the expected CAD geometry. The specimen plot comparisons were segregated by thin and thick, and by upper and lower. From the lower thin samples in Figure 5.9 the worst deviation came from the step L2, however, there is a sharp angle on the 5th step that could be caused by measurement error. Without that deviation the profile would have probably been similar to the ramp L5 and step L6 which matched very closely to each other. Specimens L5 and L6 also matched the CAD geometry the best of the four, only deviating significantly in the first three layers.

The magnitude of the deviation is considerable, by as much as 800 μm, or eight build layers. Specimen L1 ramp distorted differently than the others and probably reflects the most accurate measurement data which contains no sharp slope changes. Nevertheless, for a sample that should have been only had a 600 μm difference between the thinnest upper surface to the thickest upper surface, it showed a difference of 1000 µm. Keeping in mind the sample was anchored to the start plate with supports, its top layer was the equivalent of 8 layers taller than it was designed to be.

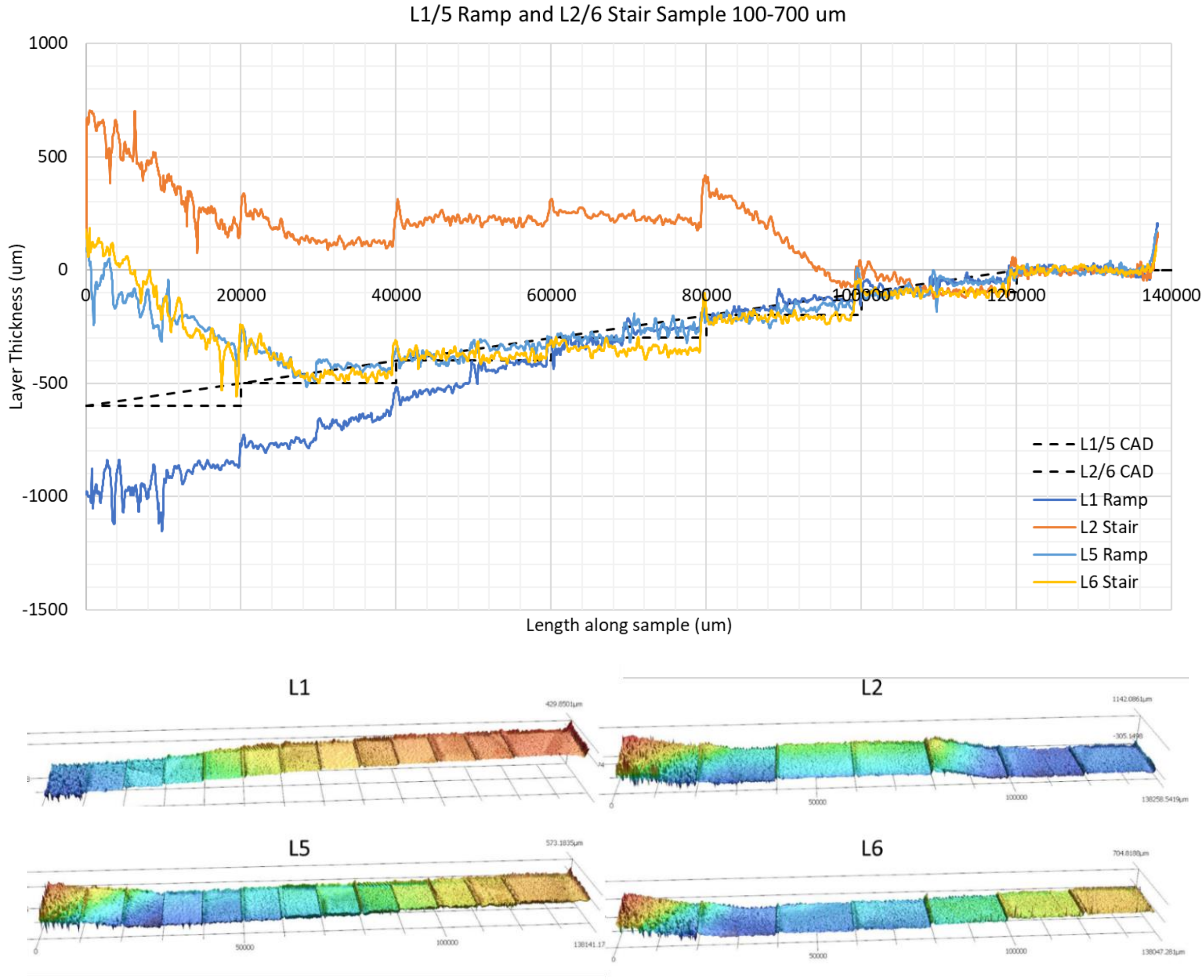

Figure 5.9. Upper surface profile plot versus the expected CAD geometry of the lower thin ramp and step specimens.

Upon examination of the lower thicker specimens in Figure 5.10, it is clearly noted that the L3 ramp very closely followed the CAD geometry with only about 100 µm deviation at the lowest thickness. Intriguingly, the L4 and L8 step specimens show the same sharp deviation at the 5th step as did the L2 step. The L7 ramp shows a similar deviation as the L5 ramp. It is interesting to note from these samples that the ramps more closely followed the CAD geometry than the steps, and the magnitude of the stepped deviations is seemingly equivalent to the thickness of the specimen. Very thin samples are prone to more dimensional deviation and is therefore not a good idea to try to print horizontal components below a certain thermal mass, even if it is supported and attached to the start plate.

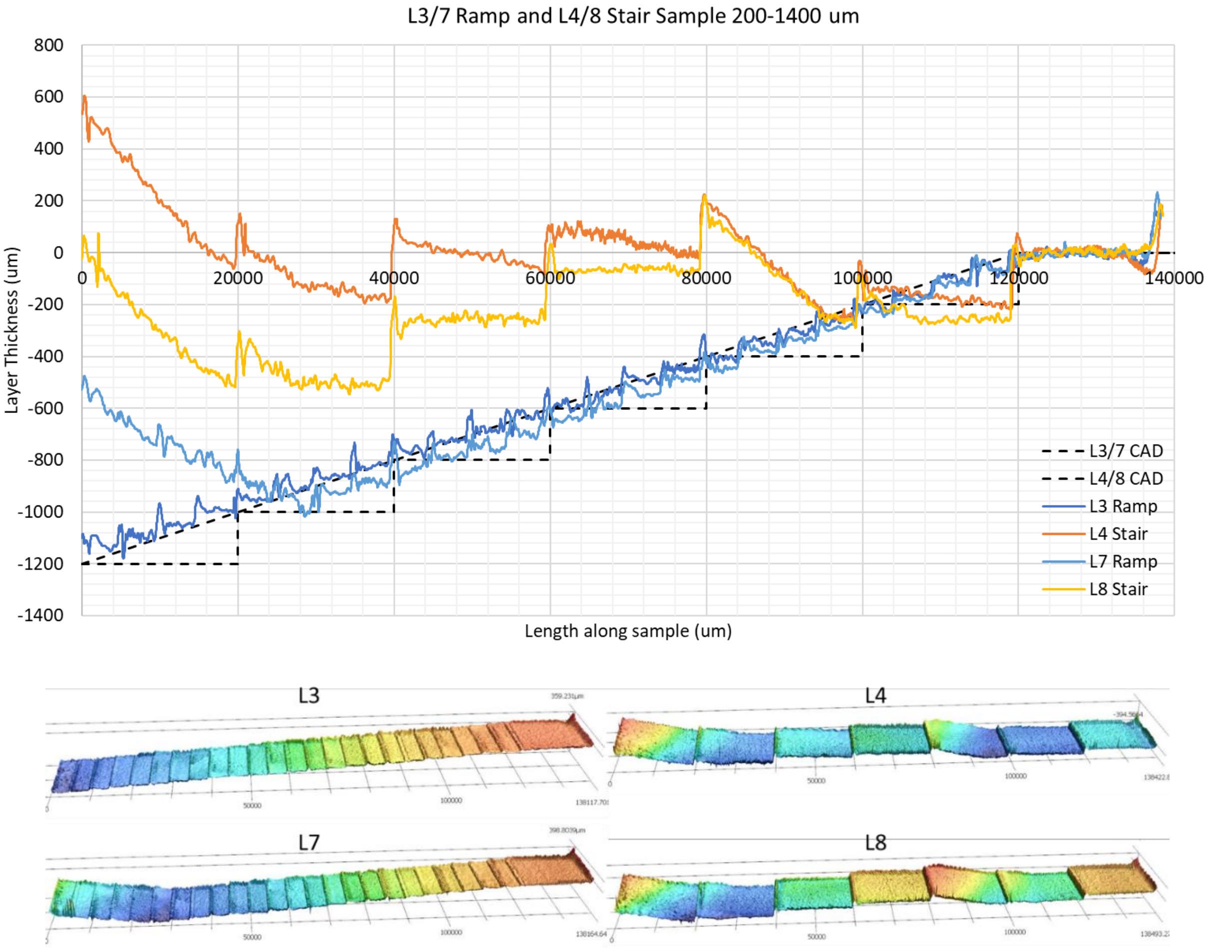

Figure 5.10. Upper surface profile plot versus the expected CAD geometry of the lower thick ramp and step specimens.

The upper thin specimens shown in Figure 5.11 and Figure 5.12 displayed even more significant divergence from the CAD geometry. The worst being the U1 ramp which varied by 4 mm in height from one end to the other. Contrasting with the lower specimens, the U2 step most closely matched only deviating from the designed profile at the thinnest and thickest layers. The deviation pattern with the U5 and U6 specimens falling between the U1 and U2, appears similar to the L1/5 and L2/6 plot. Examination of the upper thicker specimen profiles continues to show massive distortion from the CAD geometry, further emphasizing the need for more significant support structures. Another conclusion is that distortions are typically worse with large flat areas that are parallel to the build plane. In order to limit the distortion a best practice would be to orient any flat surfaces away from the build plane. It can be concluded that 5 mm of vertical support length beneath the specimens was not sufficient to root these small parts into the sintered powder.

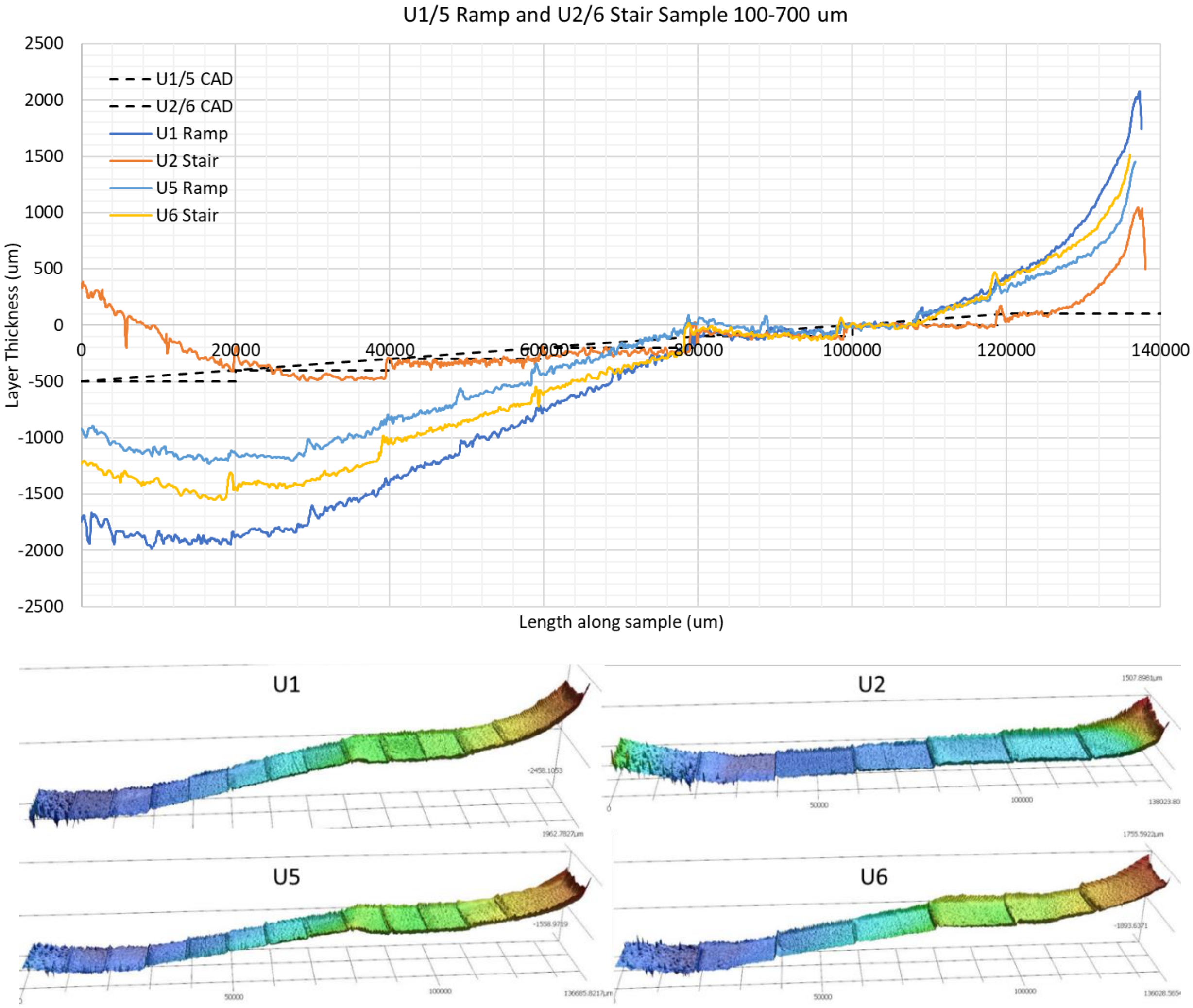

Figure 5.11. Upper surface profile plot versus the expected CAD geometry of the lower thick ramp and step specimens.

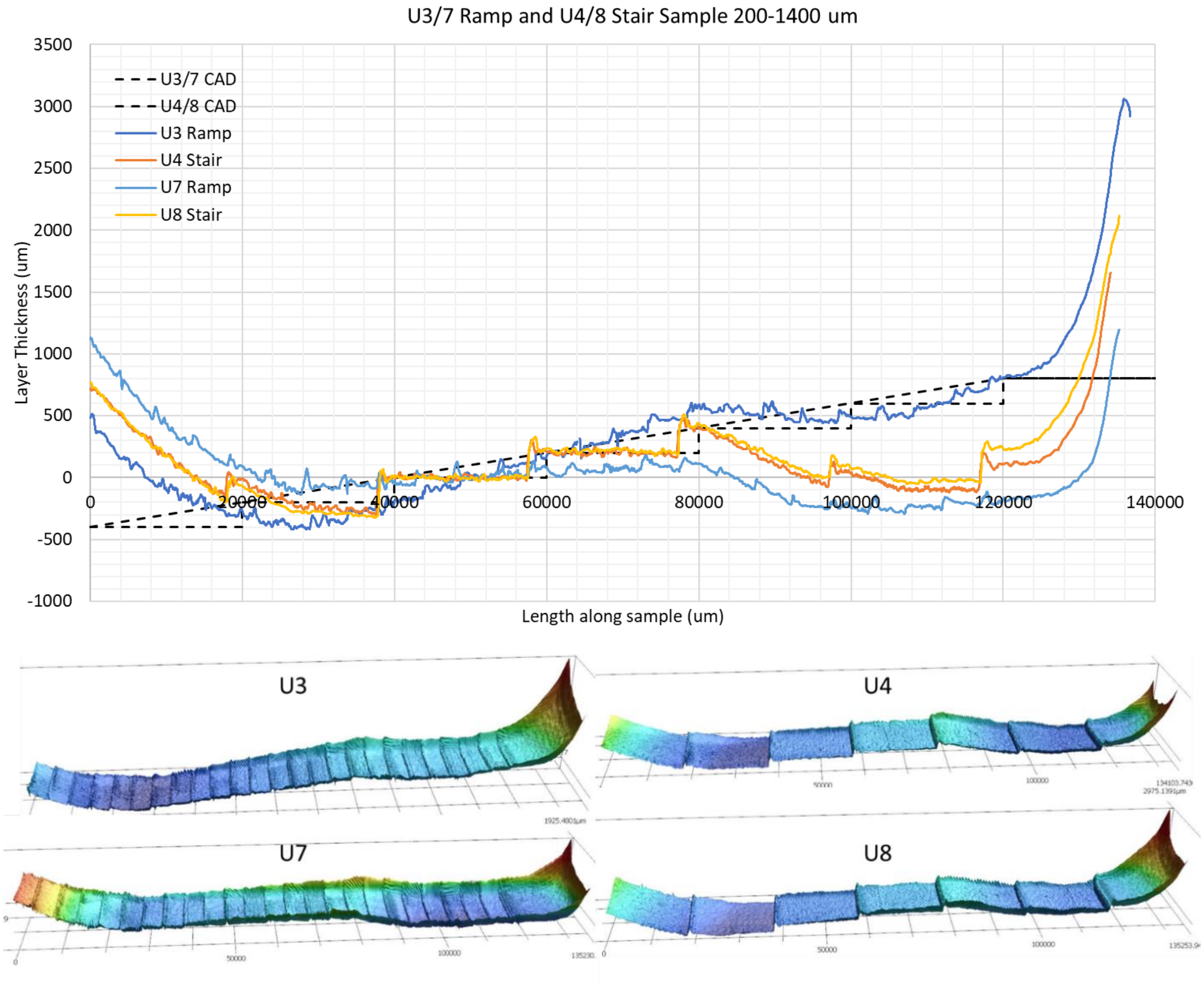

Figure 5.12. Upper surface profile plot versus the expected CAD geometry of the upper thick ramp and step specimens.

5.2.3 *Hatching Angle Analysis*

Shading differences in the upper surface topography made it immediately apparent that the hatching angle was different for every layer. It is well known that AM machines will rotate the hatching angle between layers as a way to reduce anisotropy in the material microstructure and reduce residual stress within the components. When the hatching angle was analyzed for each visible top layer surface it was expected that all of the hatching angles from specimen to specimen in a given layer would be the same.

Figure 5.13 shows that for many of the layers this was the case where for example in the first set of specimens, layer 4 at the 200 µm thickness, the measured hatch angle for L1, L2, L3, and L4 measured approximately 60 degrees from the width direction. However, when layer 8 at the 400 µm thickness is compared, the measured angle for the ramp specimens L1 and L3 measured about 148 degrees and the step specimens L2 and L4 hatching angle measured 52 degrees. Some measurement error does exist due to the accuracy of the visual inspection, but it cannot account for a discrepancy of about 96 degrees. For some reason at this layer the Arcam software chose to melt the ramp specimens which were not next to each other at a vastly different angle than the step specimens despite the specimen thicknesses being the same.

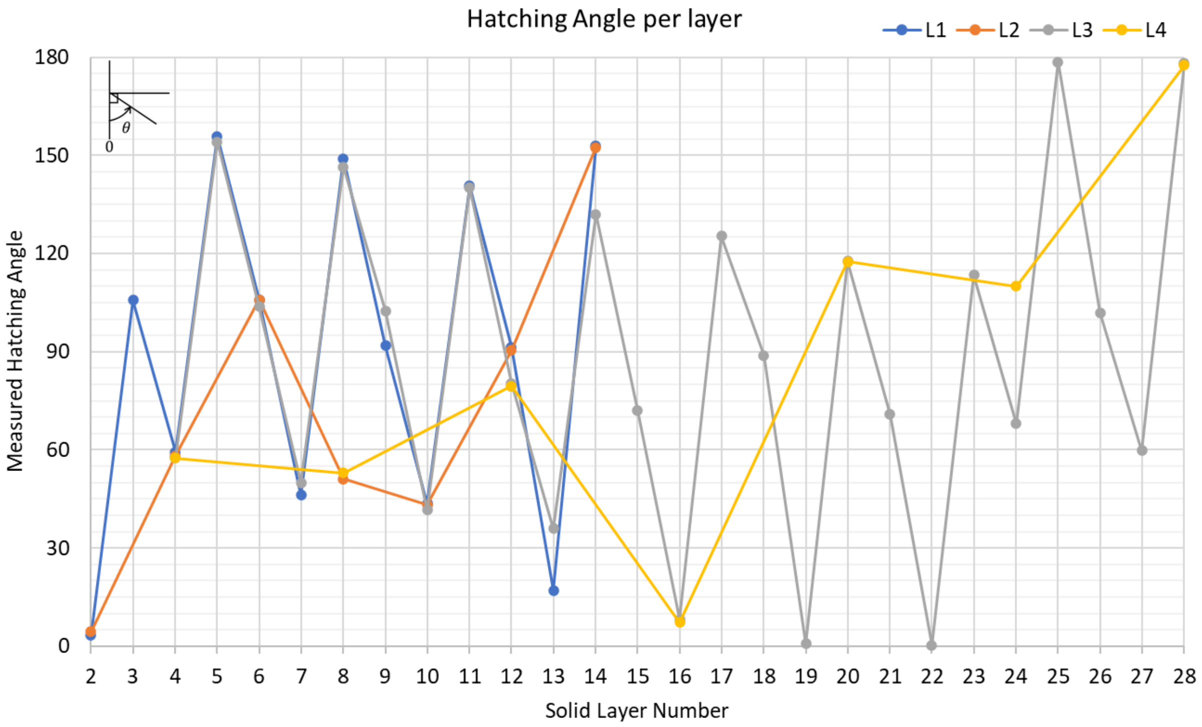

Figure 5.13. Set 1, specimens L1-L4 hatching angle compared.

A sawtooth pattern for hatch rotation angle for the thick ramp specimen L3 is apparent which seems to be mimicked by the thinner ramp specimen L1 until it reached its full height at layer 14. However, while most of the measured angles agree for these two in particular, layer 9, 13, and 14 stand out with measured angle differences greater than 10 degrees, well outside of visual error. It is unclear why the step specimens L2 and L4 sometimes match the hatch angle of the ramp specimens while other times the difference is significant such as at Layers 8, 12, and 24. The measured hatch angles for the second set of lower specimens L5-L8 depicts similar features. While the angles are different, the pattern appears similar to that of the first set. Unfortunately, the changing of the hatch pattern angle does not appear to be consistent enough to derive a function that may predict the next hatch rotation angle. The upper nested specimens of sets 3 and 4 display the same behavior with different angles.

When considering the hatching angles between the same specimen geometries in Figure 5.14, e.g. the thick ramps L3, L7, U3 and U7, the hatch angle histories are not the same. These differences can be the source of variability in distortions. The same part, printed at different z heights and locations within the build chamber, will not necessarily come out the same because the scanning pattern of the parts throughout the layers are not the same. The hatching history is therefore akin to weld sequencing for a large weldment assembly. A proper weld sequence will minimize distortion of the overall assembly, whereas a change in the weld sequence will affect how the weld assembly distorts. A randomized weld sequence will result in further dimensional deviation such that no two assemblies will be identical which was the case for the samples in this experiment, and that is not desired for repeatability.

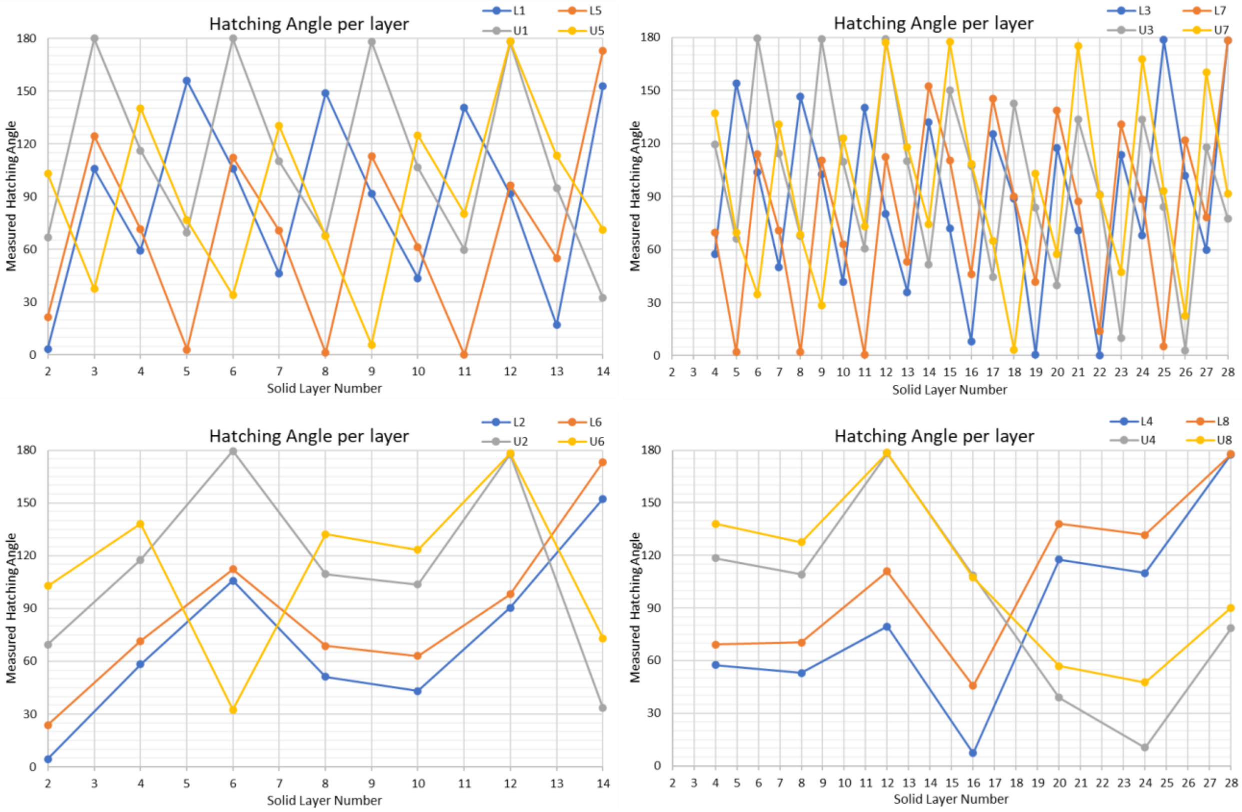

Figure 5.14. Hatching angle comparison of all four sets of specimens grouped together with the thin ramp (upper left), thick ramp (upper right), thin step (lower left), thick step (lower right).

5.2.4 *Hatching Spacing Analysis*

From the optical images in Section 5.2.1 Figure 5.6 there appeared to be a distinct change in hatch spacing with differences within the same layer. Four samples were selected to identify if there were any changes or variation in the hatch spacing parameters and they are shown in Table 5.7. The samples were selected based on appearance and because the hatch lines aligned with the X or Y direction to make the analysis more precise. Initially the hatch spacing, also thought to be the process parameter “line offset” from Table 3.3, was attempted to be measured via visual inspection like the hatch angle. However, the optical images presented a challenge since the lines appearance meandered and varied in thickness.

Table 5.7. Average hatch spacing from four samples of three different specimens, (top left) L2 Layer 6, (top right) L3 Layer 16, (bottom Left) L3 layer 25, (bottom right) L4 Layer 7.

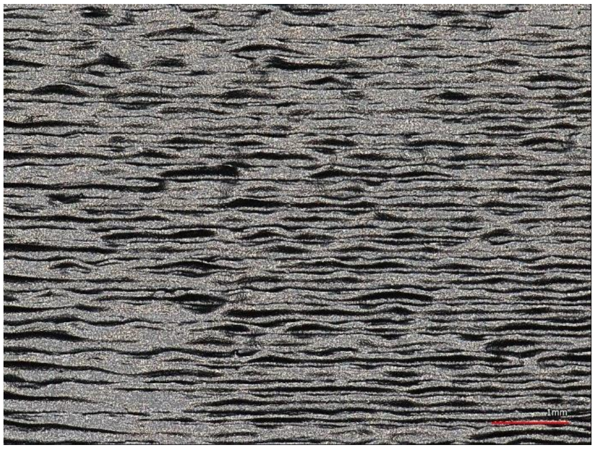	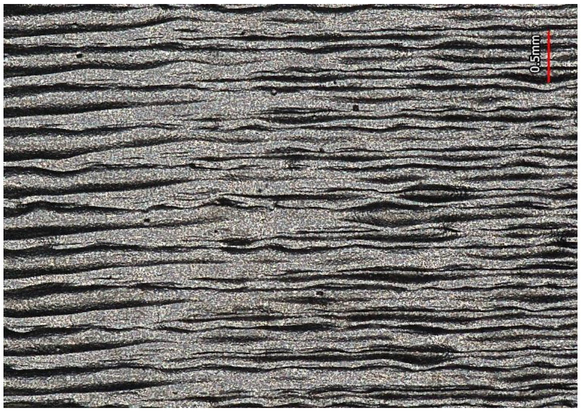
	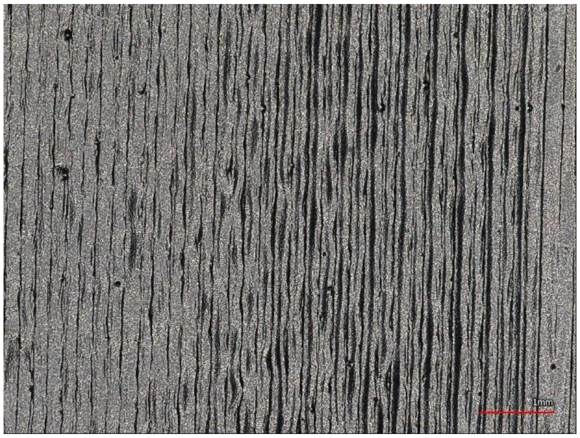

Therefore, the surface topology height data was measured using the Keyence VR-3100 on the superfine setting and extracted for analysis in MATLAB. For each of the samples, four cross sections perpendicular to the hatch direction were examined in two dimensional plots, an example is shown in Figure 5.15. The hatch lines show up as distinct peaks and valleys though there are no trends in height from one cross section to another or across the sample width. The height typically varied by ± 40 μm, or about the average size of an Arcam EBM powder particle. Despite the randomness in the magnitude of the peaks and valleys, they all closely aligned vertically making it easy to determine where the hatch lines were in the plot and count the distance between the peaks. Variation of the peaks vertical alignment is typically less than 5 μm, but does confirm the optical meandering.

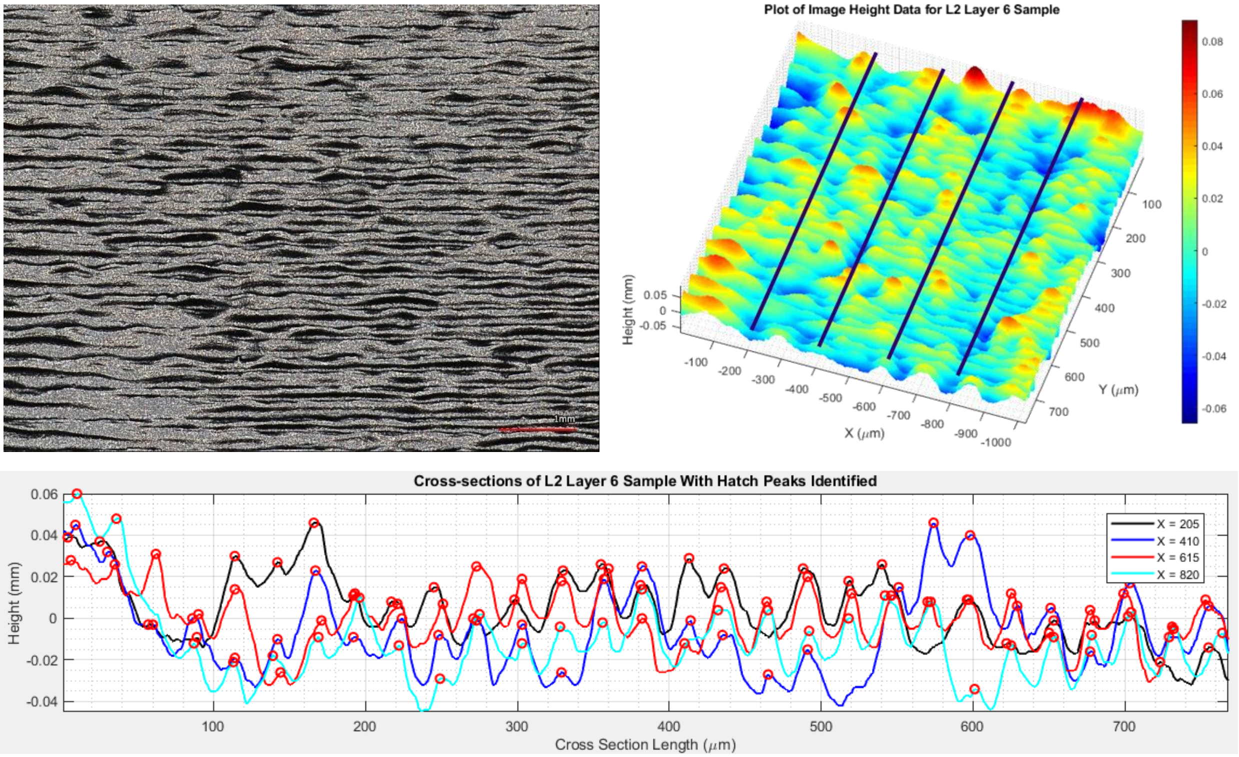

Figure 5.15. Image of L2 Layer 6 surface (top left), 3D plot of height data from image (top right), x-axis cross-sections of sample data perpendicular to hatch angle with hatch peaks identified (bottom center).

The number of peaks and the distance between them for each cross section were averaged because in some cases where a peak should have been there was a valley with no discernable peak. The effect of these missing peaks was throwing off the analysis to calculate the distance between peaks. It was also noticed that there was not a lot of variability in the measured spacing where an average was found to be about 29 μm in Table 5.8. This is nearly an order of magnitude smaller than the 0.2 mm specified by the "line offset" process parameter, indicating that value may not control the actual hatch line spacing. Only one sample, L3 at layer 16 (900 μm), displayed a trend since the hatch spacing shows high at one end and low on the other from cross section 1 to 4. Optically this can be seen as the hatch lines appear thick at one end and thin on the other. However, the ‘wide’ spacing was just due to a larger number of unidentifiable peaks due to the more even melting in that region. While optical observations gave the appearance of inconsistent hatch spacing, the numerical analysis determined this was only an illusion and that the spacing is very consistent between layers and parts.

Table 5.8. Average hatch spacing from four samples of three different specimens.

Cross Section	L2 Layer 6 (µm)	L3 Layer 25 (µm)	L3 Layer 16 (µm)	L4 Layer 7 (µm)
x1	28.88	29.25	39.62	27.14
x2	27.63	25.74	26.62	25.48
x3	26.68	26.23	25.95	28.29
x4	29.00	26.91	19.25	28.76
Avg Hatch spacing			**28.79 µm**	

5.2.5 *Surface Roughness*

Surface roughness is a popular topic in metal additive manufacturing because the as built surface is very poor by the traditional means of surface profile measurement defined by ISO 4287 which uses parameters R_a, R_q, R_{sk}, and R_{ku}. The mathematical expressions for most profile parameters are defined in ISO 4287 and are easily applied to surfaces, such as the root mean squared S_q (Eq. 5.2) being an extension of the R_q equation 5.1 where R_q is defined for a line and S_q for a plane or area.

$$R_q = \sqrt{\frac{1}{lb}\int_{lb} z^2(x)dx} \tag{5.1}$$

$$S_q = \sqrt{\frac{1}{A}\iint_{A} z^2(x,y)dxdy} \tag{5.2}$$

ISO 25178-2 provides definition of areal surface texture parameters that are more useful for the irregular additive surfaces than the corresponding profile measurements and denoted similarly as S_a, S_q, S_{sk}, and S_{ku}. The interlayer surface roughness can be defined by parameters known as Skewness (S_{sk}) and Kurtosis (S_{ku}) which are related to the S_q parameter by the third and fourth standard moment respectively shown in equations 5.3 and 5.4.

$$S_{sk} = \frac{1}{S_q^3}\left(\frac{1}{A}\iint_A z^3(x,y)dxdy\right) \tag{5.3}$$

$$S_{ku} = \frac{1}{S_q^4}\left(\frac{1}{A}\iint_A z^4(x,y)dxdy\right) \tag{5.4}$$

The Skewness represents the asperity, or the amount of bias, of the roughness shape meaning that an S_{sk} of 0 would mean that the height distribution of the peaks and valleys around the mean plane is symmetrical. If S_{sk} is less than 0 then the height distribution is skewed above the mean plane, or if greater than 0 then the height distribution is skewed below the mean surface plane. The Kurtosis measures how sharp the roughness profile is where an $S_{ku} = 3$ would mean a normal height distribution profile. Above a value of 3 would mean the distribution is spiked, and below 3 the distribution is more uniform without many outliers.

The maximum height (S_z) areal parameter is the sum of the largest peak value and the largest valley depth value within the area defined. For this experiment areal surface parameter S_z was measured for every visible top surface at each thickness and shown in Figure 5.16. The areas selected for measurement only contained the hatched area and did not include the edges where the contour scan and hatch pattern intersected. The step specimens (even numbered) only had 7 measurements, but a much larger area measured in comparison to the ramp specimens (odd numbered). The thick ramp specimens (L3, L7, U3, U7) contained the most thicknesses measured with the smallest areas available to measure. In this experiment the surface maximum height is compared with the design thickness at each layer. Also, the Kurtosis and Skewness of the surface areas were calculated.

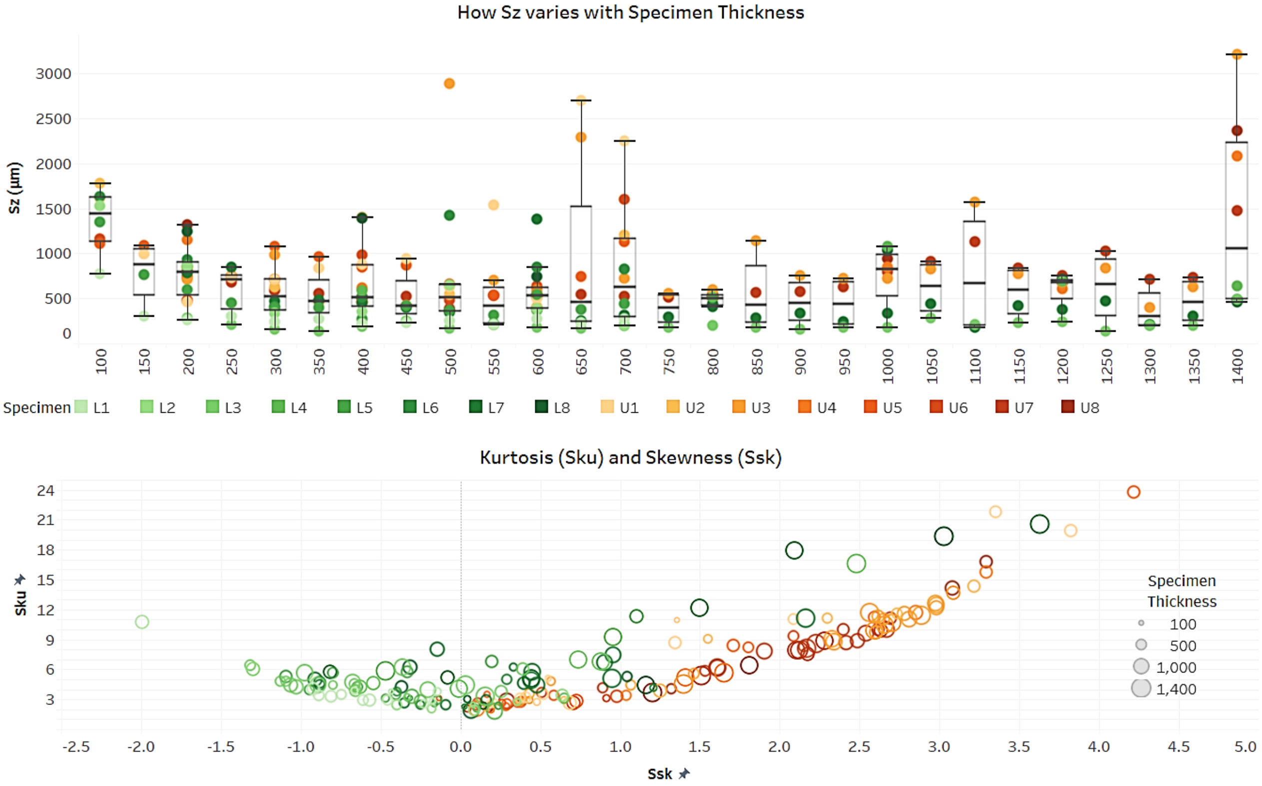

Figure 5.16. (top) Plot of areal surface parameter S_z versus specimen thickness, and (bottom) plot of kurtosis (S_{ku}) versus skewness (S_{sk}).

From the top plot in Figure 5.16 for the maximum height (S_z) measure certain trends are apparent when compared across the specimen thicknesses and build height. The lower specimens for example tended to have lower S_z values at any given thickness denoted by the green dots mostly lower than the orange dots. Specimens L1 through L8 start off at much higher S_z values on the thinnest areas varying between 750 and 1750 µm; however, as the thickness of the specimens increases, the S_z values drop mostly between 250-500 µm. The increase in thermal mass of the specimens tends to provide better surface stability with a more consistent melt.

That same parameter (S_z) does not reflect similar features on the upper U-specimens U1 through U8. While the surface roughness values were similar to the lower L-specimens at the thinnest areas they also showed the same general decrease with thickness, but did not drop as low staying in the range of 500-1000 µm. The variation was also much more significant with several excursions above 1500 µm. The difference is likely due to the insufficient supports below which is important to note. Nested parts with poor support features can drive additional variation as the layers stack up such that identical CAD models will distort differently.

The bottom plot in Figure 5.16 shows the Kurtosis on the y-axis and Skewness on the x-axis, while the thickness of each area sample is denoted by the size of the bubble and the color indicating the location of the specimen. All of the samples contained a Kurtosis of 3 or higher indicating a normal or spiked height distribution and there does not appear to be much correlation with specimen thickness or build height location. However, the Skewness shows significant correlation between the lower and upper specimens, where the lower mostly display values less than 0 and do not vary far from a typical normal distribution. Nearly all of the upper U-specimen layer surfaces are skewed below the mean plane with values above 0.

5.3 DISCUSSION

This experiment shows how well the Arcam A2X EBM creates four sets of the same geometry in different locations and heights within the build chamber. No two specimens were the same or matched the CAD geometry. Numerous inconsistencies were optically identified in the hatch scan line melting and the hatching angle: 1) the hatching angle sometimes changed within the same layer, 2) beam parameters changed within the same hatch scan causing non-uniform melting stripes. Therefore, the hatching scan history of each part is important for manufacturing repeatability and must be controlled such that it is the same for identical parts within the build chamber. In the welding industry for large assemblies this is more commonly known as weld sequencing and essential for product repeatability.

The initial layers contained heavy porosity that was mostly unnoticeable by the 300 μm layer (6 layers) indicating that this much of the down skin surface of all parts contain poor strength. Recall a similar depth was identified in the previous Line experiment. For a designer they must consider the build direction in their design such that up to 300 μm of any downward facing surface either be removed via post processing, or that amount of additional thickness is added and not expected to carry high stress.

The hatch spacing also appeared to be inconsistent, but the cross-section analysis showed this was an illusion since peaks still lined up. A question still remains as to why the measured hatch line spacing was 0.029 mm while the “line offset” process parameter is set at 0.2 mm. What the cross-section spacing analysis also revealed was the variation in the melt peaks means any given line may vary in height by as much as 100 μm. This is greater than the average powder particle size and twice that of the layer thickness. With variation in the top melt that significant it will certainly affect the next layer placed on top such that the beam is melting an unknown random thickness of powder that could be as much as 3 layers, or 150 μm.

From the surface roughness analysis, the better supported lower L-specimens showed much less variation in maximum height with the S_z curve in Figure 5.16 again pointing to the 300 μm layer thickness where the roughness became more consistent. The kurtosis and skewness provide insight into the interlocking effects of additive surfaces when placed in contact. There is a lot more variation in the upper specimens indicating that parts placed closer to the build plate are more repeatable than those placed higher in the build chamber.

Chapter 6. TAPERED BOX BEAM EXPERIMENT

The purpose of this study was to explore the application of an organically shaped topology optimized cantilevered tapered box beam structure in the place of a traditional cantilevered tapered box beam. The design space was scaled down to a reasonable volume, but not such that the structure could fit in the chamber of an Arcam A2X EBM additive machine as a single part. The required size meant that it must to be printed in at least two pieces that required assembly. A 3D topology optimized, organically shaped, asymmetric solution was generated, which was followed by a CAD design and finite element stress analysis to ensure the result would meet the application requirements.

An experiment was conducted in order to test the manufacturing repeatability of the design for additive manufacturing (DfAM) structure, where multiples of beam parts were printed out of gas atomized Ti-6Al-4V powder using default Arcam ‘optimized’ process parameters [32]. The beams were assembled to later be tested for ultimate load in both bending and torsion. The work flow of the optimization process, design strategy, manufacturing, and assembly will be presented. This serves as vital information for any additive manufacturing designer who must design for the additive EBM process and understand how repeatable the process is at manufacturing capable products.

6.1 METHODS

A design problem was introduced that required a cantilevered tapered box beam to be additively manufactured from Ti-6Al-4V. This was to be representative of a scaled down forward strut box of a commercial aircraft engine pylon using a typical fan case front mount configuration. The box beam design space was to be topology optimized using maximum stiffness criteria, before being redesigned to account for stress and manufacturing criteria. An Arcam A2X PBF EBM machine was available for manufacturing utilizing gas atomized Ti-6AL-4V powder. To demonstrate manufacturing repeatability, six beams would be printed and analyzed for dimensional deviation. The overall build preparation process flow that was executed is shown in Figure 6.1. This displays the steps taken from defining requirements to uploading the build file to the machine. There are a couple iterative loops at the optimization and design-analysis stages.

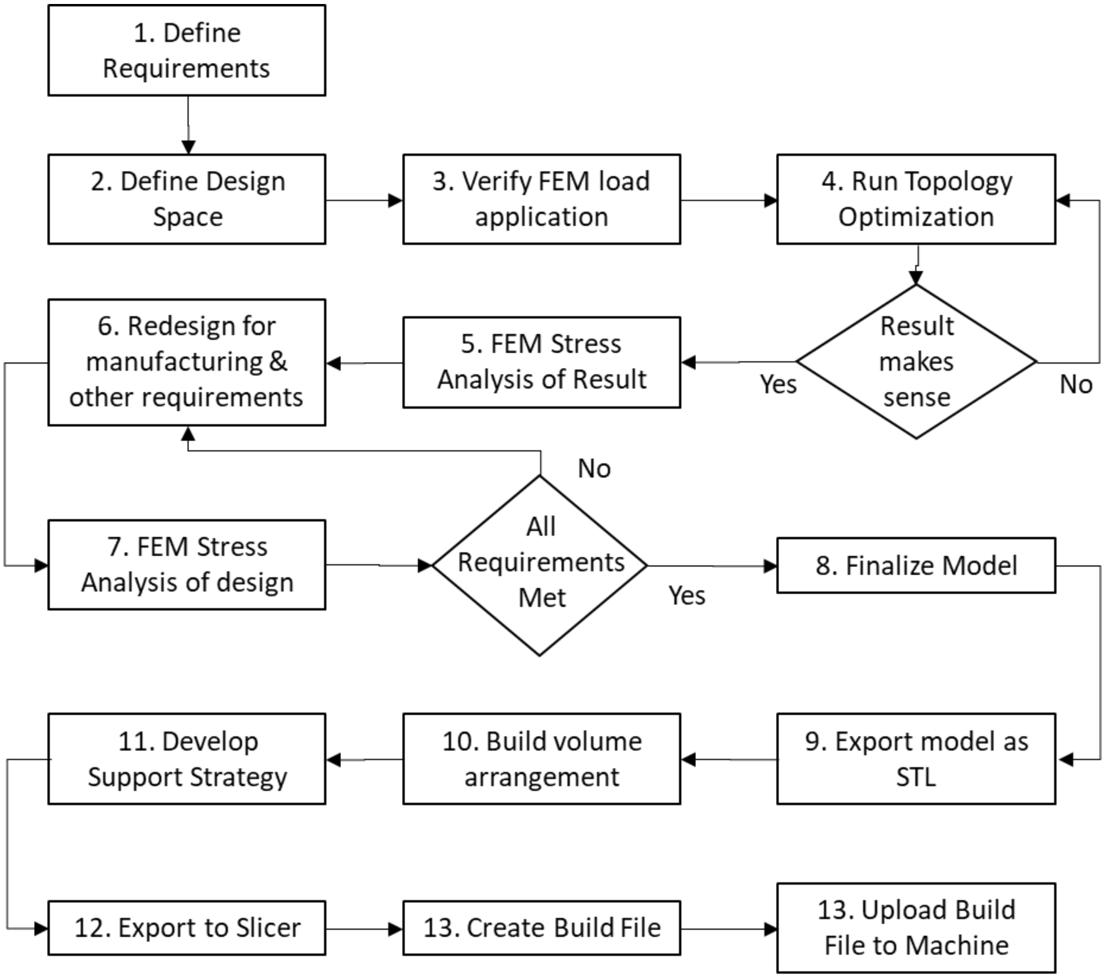

Figure 6.1. Process flow diagram for optimization, design, analysis, and build preparation stages.

6.1.1 *Topology Optimization*

The inspiration for the design in this study was the forward section of a commercial aircraft engine pylon. The engine uses the traditional fan case front mount and rear turbine frame aft mount configuration. At each mount is a titanium bulkhead machined from plate and spanning the distance between the forward and aft bulkheads is the forward strut box. This section of the pylon is typically designed as an assembly of chords, webs, and frames in the shape of a long, tapered box. Figure 6.2 illustrates the representative application design space.

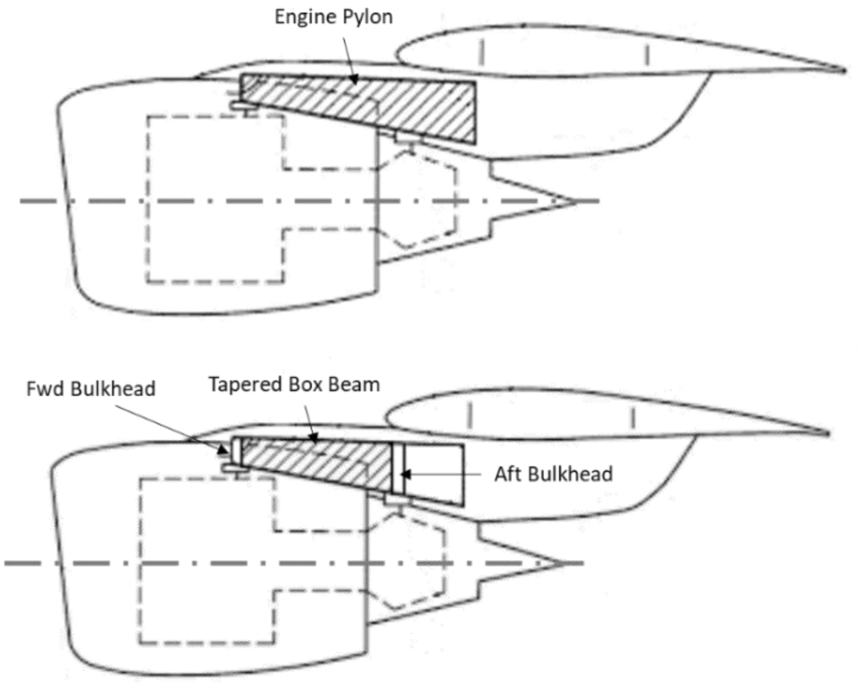

Figure 6.2. Illustration of a typical commercial aircraft engine fan case mount pylon configuration demonstrating the representative application space.

To keep the experiment to a manufacturable scale using an Arcam A2X, the design space was reduced to a small fraction of the full-scale application. In this regard, the specimen was sized by the 200 mm x 200 mm x 380 mm build volume, and Figure 6.3 shows the design space dimensions. At this scale it was still necessary to make the final specimen an assembly by splitting the model into two halves that had to be bonded and fastened together. The worst-case loading conditions for this application are assumed to be an 8G vertical and 3G side load applied individually at the center of gravity (CG) which is assumed to be located along the representative engine centerline, 171.4 mm from the bottom of the aft box section and 371.1 mm forward of that station location. The forward section of the pylon does not see any axial thrust loads because of this engine mount configuration. There are typically thrust links attached at the forward compressor case that carry the thrust loads to the aft mount and through the aft bulkhead. For this scaled investigation the engine weight carried by the front mount is assumed to be 45.4 kg (100 lbs.), making the vertical and side loads 362.9 kg and 136.1 kg respectively

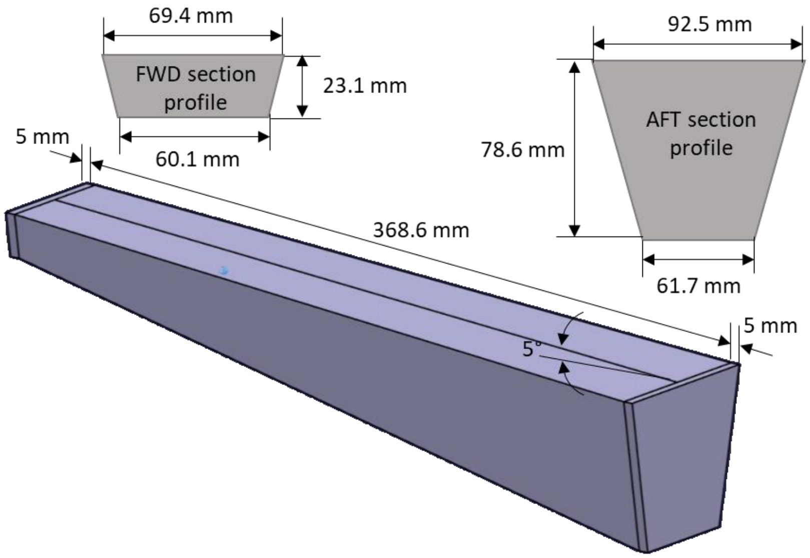

Figure 6.3. Design space dimensions for experimental manufacturing specimens.

Since a traditional forward strut box assembly would be manufactured using sheet metal or machined plate, the assumed material properties for the topology optimization and follow-on stress analysis were taken from AMS4911 where the Ultimate Tensile Strength is 920 MPa and the Yield Strength at 0.2% offset is 869 MPa. The requirement for the design is to avoid yielding at the maximum load conditions with the application of a 1.5 maximum principal stress factor of safety. That made the maximum principal stress allowed in the beam to be 579.2 MPa (84 ksi).

For the design space and loading condition described, the topology optimization problem was modeled as shown in Figure 6.4a. The solid design space included a 5 mm forward and aft constant extrusion to serve as the boundary conditions where the four exterior surfaces of the constant section represented the attachment locations at the forward and aft bulkheads. These locations were assumed to be rigid with the aft surfaces being fixed in 3-dimensions. The loads were coupled to the forward surfaces from the CG load application point. The vertical and side loads were applied separately in positive and negative directions. At a distance the side load produces a moment and torsional force on the forward end of the beam. A simulation performed on the design space used a finite element method (FEM) based approach with a simple linear TET4 mesh containing a total of 117,064 elements. A simple verification of the loading condition is shown in Figure 6.4b and c to ensure the conditions of the simulation are applied correctly.

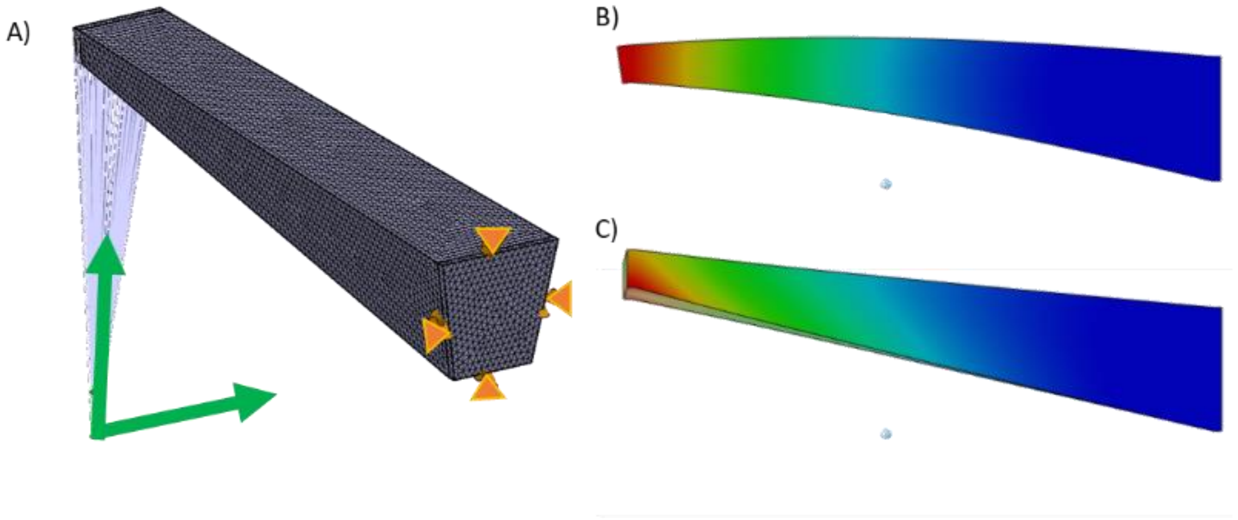

Figure 6.4. A) Topology optimization design space setup, B) Negative vertical bending load verification simulation, C) Positive side torsional load verification simulation.

Most commercially available topology optimization software applications offer a variety of controls that can be employed in an effort to consider the numerous limitations design engineers must take into account. Some of these that are qualitative in nature are extremely difficult to numerically program into an algorithm. The more controls that are utilized makes a convergence more difficult and less likely for complex three-dimensional problems. Therefore, knowing that the optimization result is more of a starting point than an end point, the constraints were kept simple.

A commercially available software (3DExperience) was employed that used a density gradient approach. Initially, an optimization run was conducted with a maximize stiffness criterion, mass target of 0.68 kg (1.5 lbs.) and an axial shape control set to 45 degrees. The axial shape control was an effort to take the expected additive manufacturing build direction into account in the earliest design phase. While the solution was able to converge, stopping at 57 of 60 iterations and resembling a truss-like structure, it was not a useful result because the final geometry contained various unconnected branches ending in space that were clearly incapable of carrying load. The second optimization run was further simplified by removing the shape control and only used the same maximize stiffness and mass target defined in the first run. That setup yielded a much more practical truss-like result that could be carried forward through the design and analysis phases. The optimization plots showing convergence on mass and stiffness for both runs can be seen in Figure 6.5.

Topology Optimization Run 1

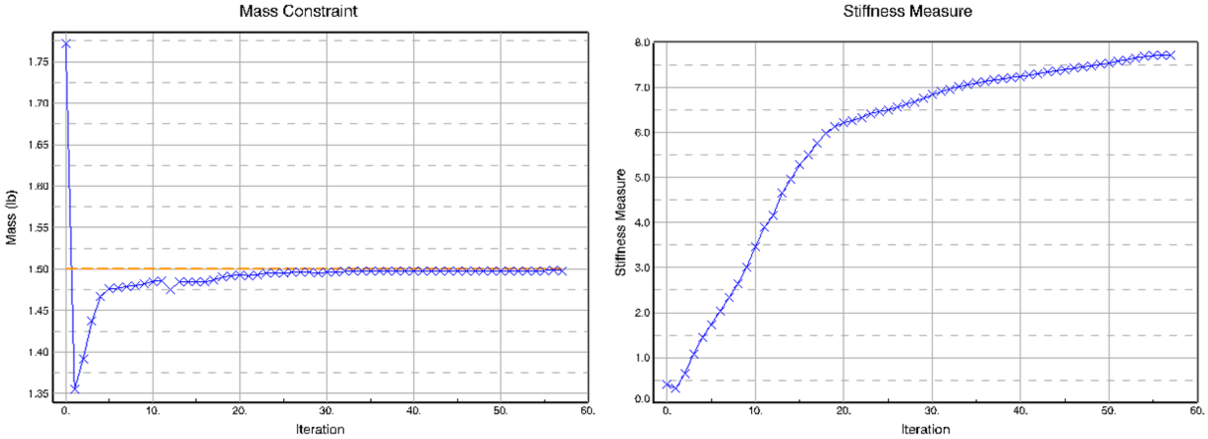

Topology Optimization Run 2

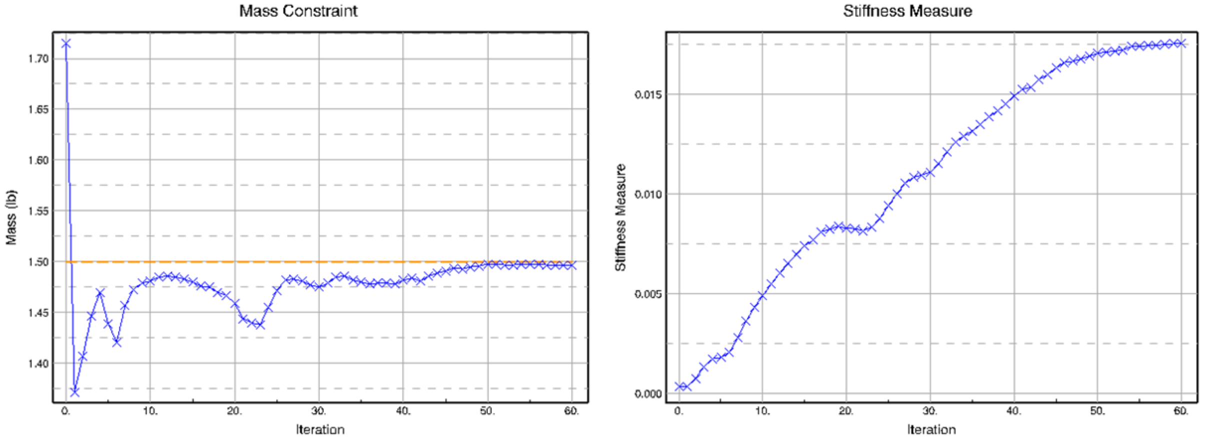

Figure 6.5. Target optimization plots for mass and stiffness versus the number of iterations.

The geometric results of both runs are displayed in Figure 6.6 and Figure 6.7. The images on the left depict various views of the density gradient based optimized shape. The primary load paths show as fully dense in red, with the lesser load carrying mass needing less density. To the right of the density color mapped shapes are the resulting FEM meshes, wrapped in a closed surface and solidified into a CAD model. The surface is run through a smoothing algorithm to remove rough edges. At first glance the two results appeared quite similar, the optimization algorithm determined a hollow truss-like structure would be the stiffest design to counter the bending and torsional loads in the simulation. In comparing the first run in Figure 6.6 to the second, it can be seen from the aft end where the shape control was forcing the axial angle of the truss members to be 45 degrees or greater, however at the front of the beam the shape control began to break down. This is where one can identify disconnected clumps of mass that would not carry any load and certainly not be optimal. In Run 2 shown in Figure 6.7, without the shape control the truss members appear more well defined with identifiable load paths. The Run 2 resulting solid would weigh 1.08 kg which is not the 0.68 kg weight specified by the topology optimization target. The reason for this is the optimization mesh is formed with elements of varying density. When it is wrapped with a smoothed surface and solidified into a CAD model, the entire structure becomes fully dense and the weight increases.

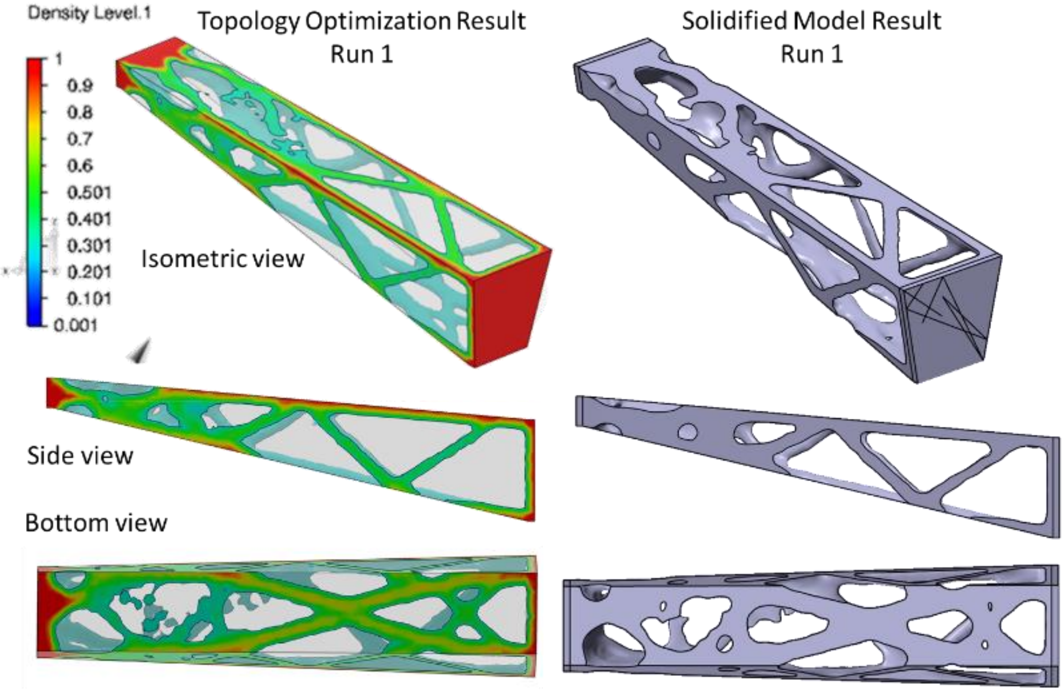

Figure 6.6. Topology optimization result for run 1 with shape control, maximum Stiffness, and mass target of 0.68 kg.

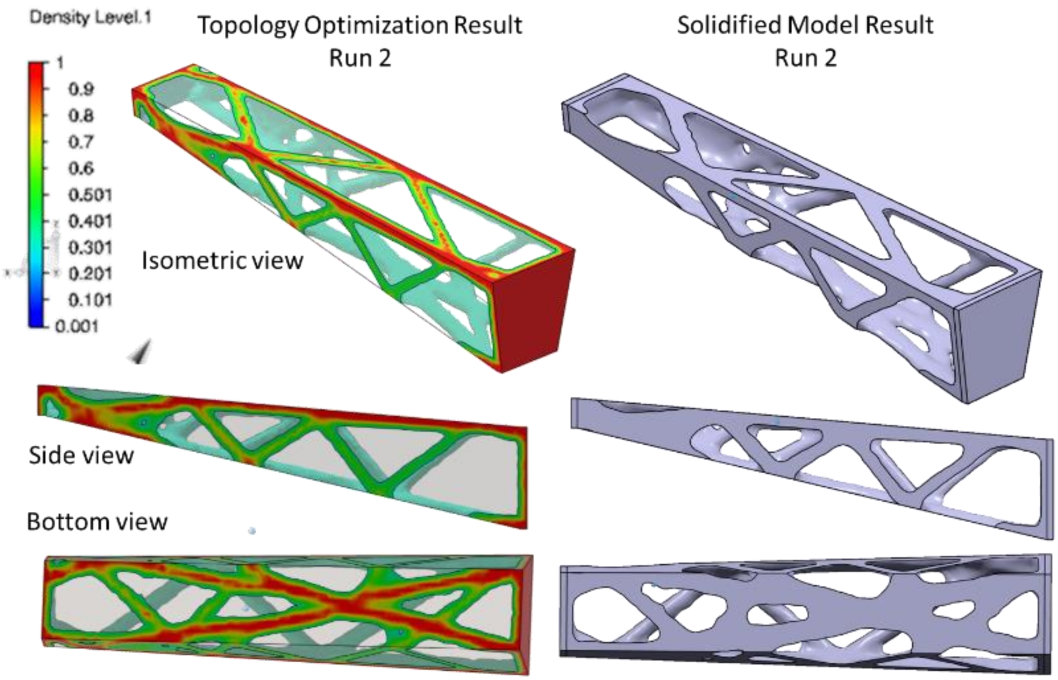

Figure 6.7. Topology optimization result for Run 2 using maximum Stiffness, mass target of 0.68 kg, without shape control.

6.1.2 *Specimen Design*

Despite the load cases being symmetric in direction and magnitude, the resulting shapes are asymmetric. The optimization maximized the cross-sectional area of the design space by only placing material along the external boundaries of the tapered box volume. While the fore-aft internal radii of strut intersections are well rounded to reduce stress concentrations, there are sharp edges at the design space boundary. The sharp edges are a deficiency in resulting solids because the regions would carry little to no load at the boundary and only serve as stress concentrations. Therefore, a further optimized shape would have rounded and smoothed boundaries, especially for manufacturing via additive PBF where sharp corners and edges are not desired. An experienced designer can take the preferred result from Run 2 and apply it as an exemplar by adjusting the design to account for additional criteria such as stress and manufacturing. One thing to note is that the topology optimization simulation can take into account stress criteria targets; however, it requires a much finer mesh of non-linear elements that dramatically increases the computation cost without necessarily providing a better result.

A new design for the tapered box beam was created, based on the example from Run 2 by resurfacing the truss structure. Initially the structure was closely duplicated with the edges completely smoothed over. Then a middle split plane was chosen, because the beam was too long to be manufactured in a single piece, and this forced some truss elements at the rear of the box to be shifted forward. Through the iterative design and stress analysis process detailed in Section 6.1.3 the overall structure was able to be reduced in weight by 7% to 1.0 kg. The final design and comparison to the topology optimization is shown in Figure 6.8. Significant deviations from the optimized result were done at the front of the box beam, as can be seen in comparing images a) and c), in order to reduce large solid cross-sections to a more porous system of truss elements. This modification then required the addition of a cross brace element on the top and bottom of the forward end depicted in Figure 6.8c due to the reduced stiffness, but in manufacturing terms by reducing the local thermal mass this would be better for additive manufacturing. The resulting design resembles and organic shape, symbolic of optimized structures designed for additive manufacturing that cannot be manufactured any other way.

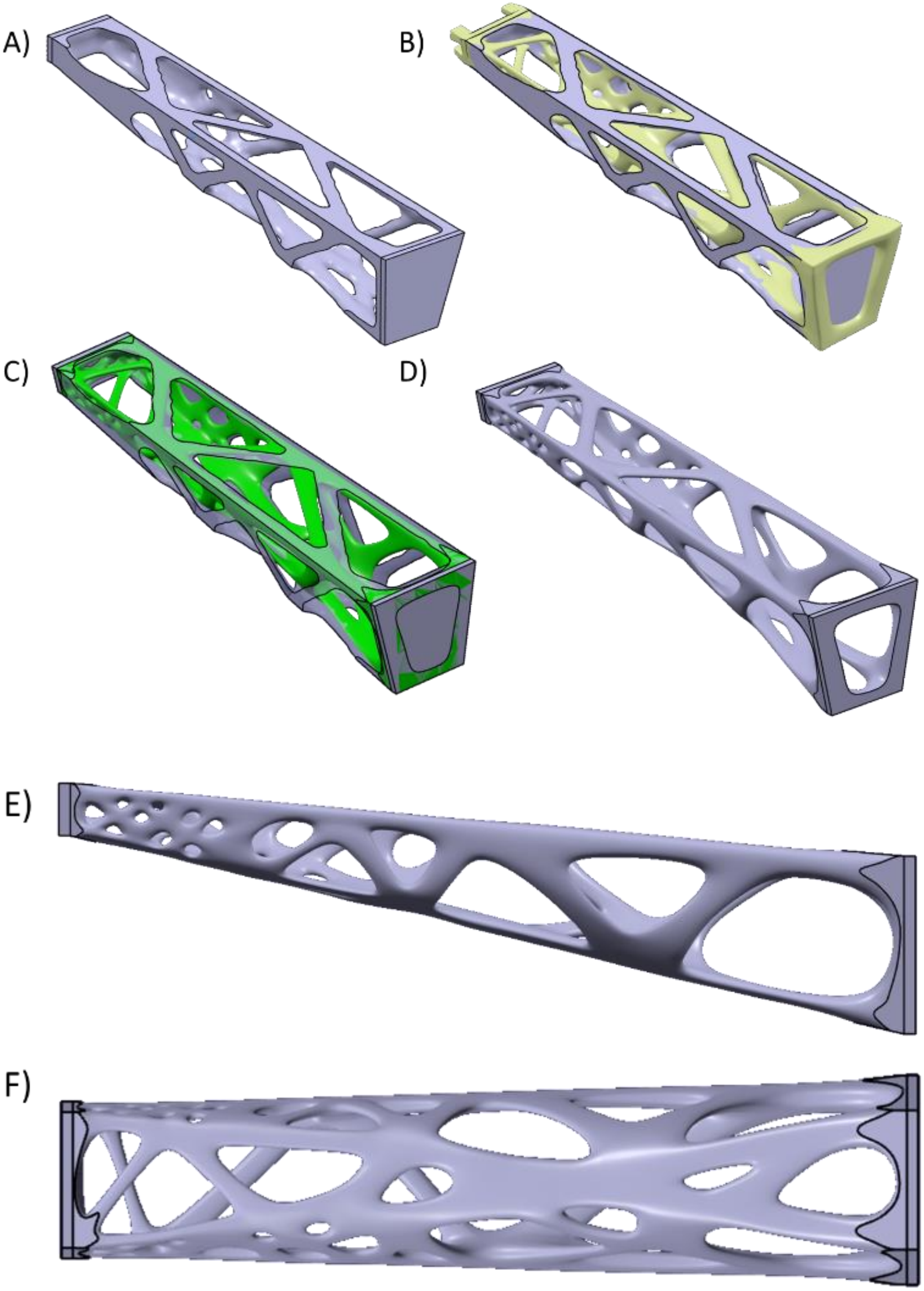

Figure 6.8. A) Run 2 topology optimization result, B) surface reconstruction (yellow) overlaid with optimization result solid, C) final design (green) overlaid with optimization result solid, D) smoothed final design solid isometric view, E) final design solid side view, F) final design solid bottom view.

Orientation of parts in a powder bed fusion build chamber is often a trade-off of many factors. From build height driving processing time and quantity of powder needed, to the quantity of supports driving post-processing time and effort. A middle span split in the beam was selected in order to minimize the overall build height in the electron beam build chamber with the specimens oriented vertically. The vertical orientation heavily reduced the amount of supports needed and post processing effort; however, minimizing this direction is important to reduce the build time, as well as the quantity of powder required in the hoppers. It is not possible to load additional powder while insitu; therefore, it was necessary to keep the length of each span section equal to minimize the overall build height.

The design of the interface for the two beam elements was a challenge similar to the one any engineer faces with seemingly infinite design possibilities. Without the luxury of example geometry to imitate, a 3-dimensional interlocking shape was created with the adjoining faces arranged to transfer the critical bending and torsion loads. This beam had three interfaces, each with different cross-sectional areas and shapes, but because joint design was not the focus of this study the geometry was simplified and likely not optimal. A bonded assembly was the primary reason for the layout of the joint, with the capability of adding fasteners. The forward and aft sections of the beam are intended to slide together axially with a designated surface clearance of 0.1 mm to create a tight fit that could still be manually assembled. Figure 6.9 displays the 3-dimensional shapes of each of the three joints on the forward and aft sections of the beam. A maximum fore-aft overlap of 10 mm was sufficient for adequate surface area contact, any more would have required more complicated interfaces.

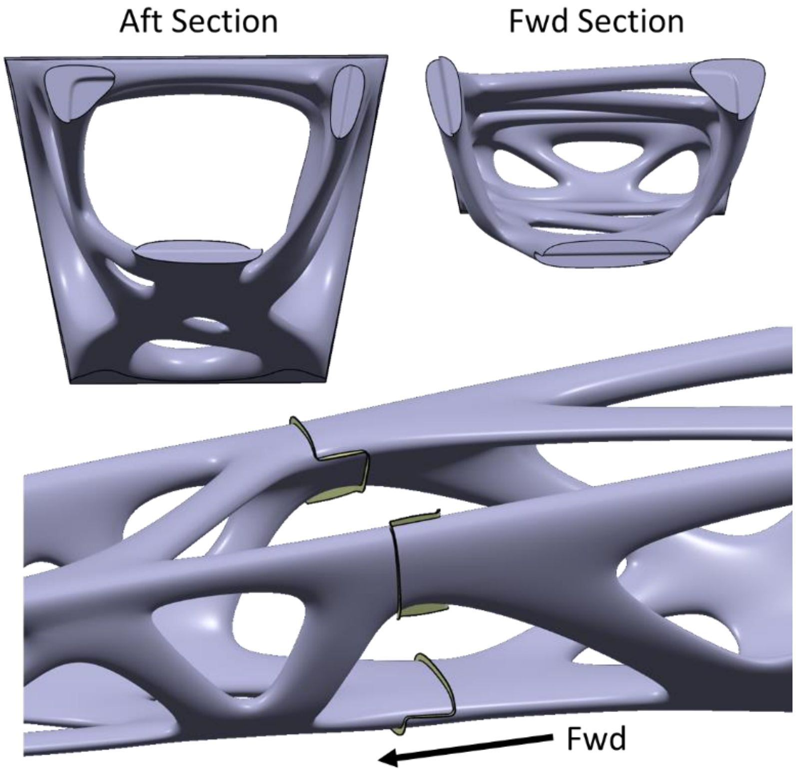

Figure 6.9. Top) Aft and forward views of the three joint locations, Bottom) Rotated view of the assembled beam at the mid-span joint location with the 3D splitting surfaces shown.

6.1.3 *Stress Analysis*

The resulting solid from Run 2 of the topology optimization was meshed and analyzed for stress and displacement using the same load case defined for the design space. Those results provided influence and guidance for the resurfacing and design for additive manufacturing. The following new design was then meshed and run through the load cases to identify areas of predicted stress that would exceed the requirements. An iterative loop was established in the process flow where after the initial analysis, the design was modified, remeshed, and analyzed again before incorporating additional changes to the design. Overall, there were at least 10 design/analysis iterations performed to determine the final specimen geometry.

The Run 2 optimization solid was meshed using robust quadratic tetrahedron (TET10) elements with an average element size of 1.27 mm. This FEM model contained a total of 412,364 elements and 692,225 nodes. The average aspect ratio was 1.709 with only 487 (0.12%) elements reported as poor. The same loading conditions that were applied to the design space from Figure 6.4 for the topology optimization were reapplied to the optimized mesh using the same boundary conditions. Loads were applied at the CG point below the front of the beam with rigid coupling connections tying the input loads to the external faces of the forward 5 mm extrusion. At the aft extrusion external faces, fixed displacements were applied for all directions to not allow translation or rotation. Computation time for the four load cases using the Abaqus solver required less than 10 minutes on a Dell Precision 7520 laptop.

Per the requirements of the beam, the primary concern was for the maximum principal stress criteria to stay below 579.2 MPa. Because the failure mode will be in tension, scales for the analysis were set to 572 MPa maximum and 0 MPa minimum to highlight areas of interest close to exceeding the design value in tension as red with black in the middle, and compressive stress will display black surrounded by blue. Figure 6.10 shows some of the results of the stress analysis for the Run 2 optimized result. Without any input for stress criteria in the optimization targets, the peak principal stresses for the bending +/-Z load cases ranged from 335 MPa to 424 MPa respectively. For the torsion +/- Y load cases the principal stresses ranged from 696 MPa to 541 MPa respectively. Close inspection of the +Y case was conducted because it showed a stress beyond the desired range and was found to exist at the corner of the load application boundary. Upon analyzing the Von Mises Stress, the +/-Y case peaks at 558 MPa while the +/-Z case peaks at 421 MPa. A maximum displacement of 1.24 mm occurred at the forward end for the torsional case, while the bending case resulted in a maximum displacement of 2.91 mm.

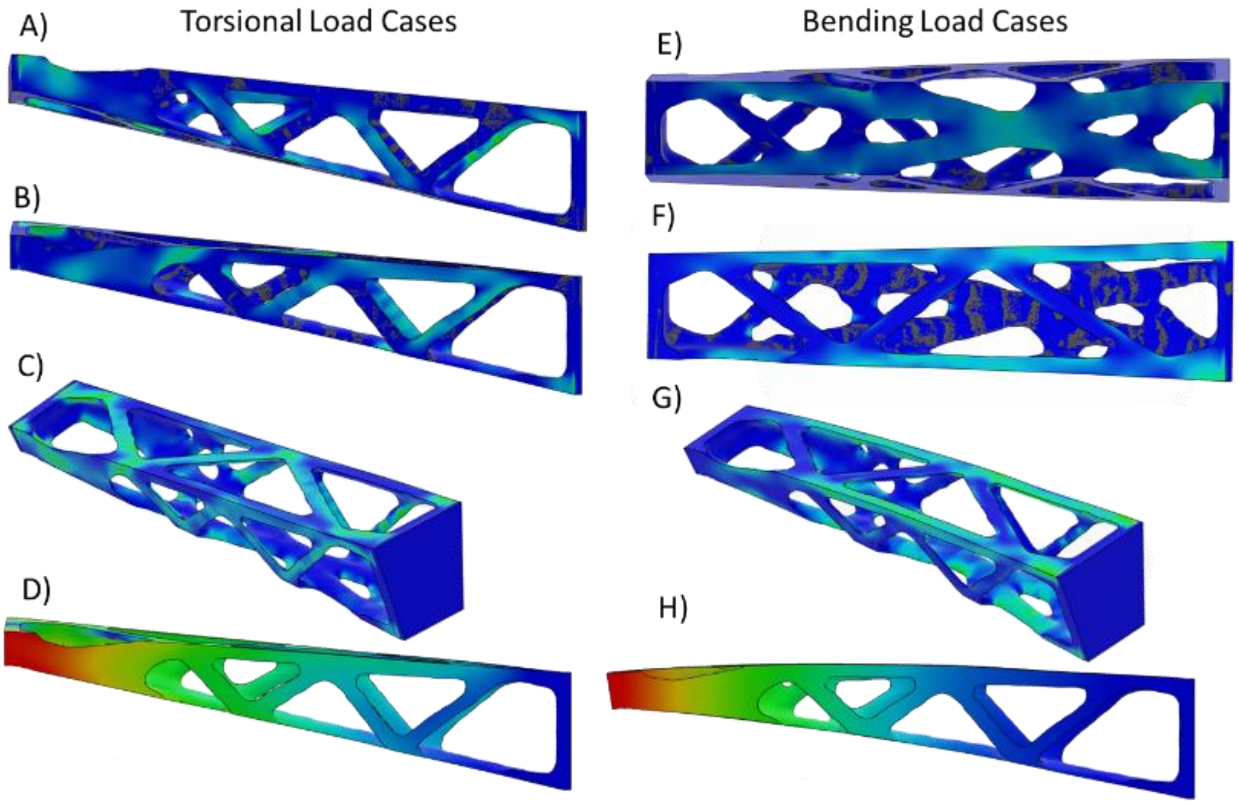

Figure 6.10. Stress analysis results of the Run 2 optimization solid, A) +Y loading maximum principal stress, B) -Y loading maximum principal stress, C) Y direction loading von mises stress, D) Y direction displacement, E) +Z loading maximum principal stress, F) -Z loading maximum principal stress, G) Z direction loading von mises stress, H) Z direction displacement.

These results indicate that the optimized structure is over performing in bending, but adequately stiff in torsion. This suggests that there was opportunity for weight reduction in the redesign phase. In bending, particularly in the +Z direction, the lower crossing members are the primary tensile load path, yet the average stress is lower than half of the maximum allowed which still has a 1.5 factor of safety beyond that limit. In torsion, the primary load paths twist around the structure clearly indicating the crossing top-bottom, or left-right truss elements as the key beam components. Depending on the direction of twist, elements in tension in one direction show as in compression in the opposite loading direction. There is still a strong indication that these elements are larger than required with average stresses also less than half of the allowable limit.

Following the analysis results of the topology optimized solid, an iterative redesign loop took place where modifications were made to the resurfaced CAD model and it was remeshed and analyzed before additional modifications were made. The analysis results presented here and shown in Figure 6.11 reflect the final configuration of the tapered box beam structure. The solid model was meshed similar to the optimized result using robust quadratic tetrahedron (TET10) elements with an average element size of 1.27 mm. This FEM model contained about 5% fewer elements for a total of 389,681 and 651,656 nodes. The average aspect ratio was 1.692 with far fewer elements reported as poor at 44, or 0.01%. Similar loading conditions were applied at the CG point below the front of the beam with rigid coupling connections and the same boundary conditions at the aft extrusion to not allow translation or rotation in any direction. Computation time for the four load cases using the Abaqus solver required less than 10 minutes on a Dell Precision 7520 laptop.

As previously stated, the weight from the stiffness optimized result was able to be reduced by 7% using stress criteria to slim down oversized truss elements and increasing radii in connections. That had the effect of increased deformation in the Y and Z directions to 1.78 mm (43.5%) and 3.58 mm (23%) respectively which were still considered within acceptable values at the maximum loading condition. The peak stress condition was still found in the +Y torsional loading condition at the same boundary condition edge as before with the stress increasing to 781 MPa. It was reasoned that this was acceptable because even if it is artificially high being at the boundary condition, it was still 10% below the theoretical yield stress of the material. Elsewhere in the beam in that loading condition the peak stress was just below the design limit at 571 MPa.

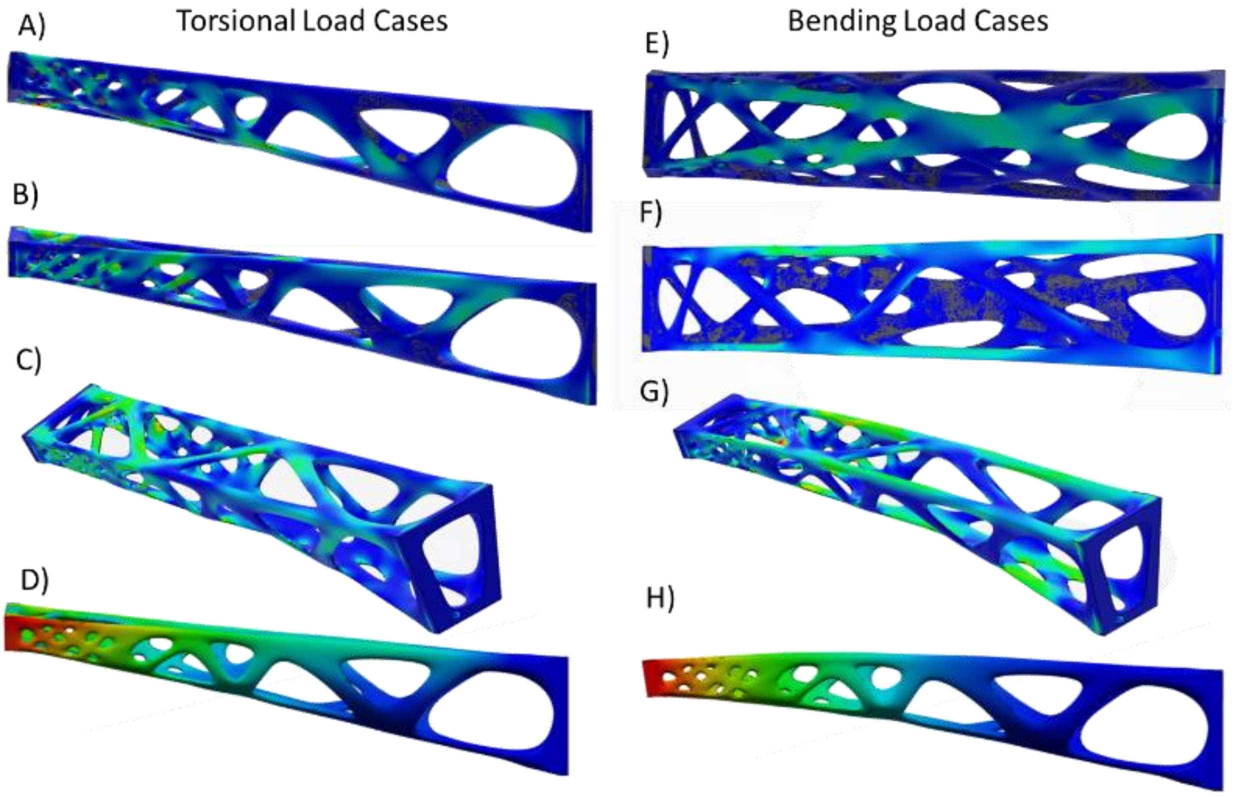

Figure 6.11. Stress analysis results of the final design solid, A) +Y loading maximum principal stress, B) -Y loading maximum principal stress, C) Y direction loading von mises stress, D) Y direction displacement, E) +Z loading maximum principal stress, F) -Z loading maximum principal stress, G) Z direction loading von mises stress, H) Z direction displacement.

In the redesign for additive manufacturing phase described in Section 6.1.2, special attention was paid to applying smooth curves and cross section transitions. That allowed stress to be distributed more evenly without the concern for complexity which would make the beam more difficult to manufacture via traditional methods. The final geometry of the beam met all design requirements for both stress and weight.

6.1.4 *Build and Machine Setup*

To manufacture a CAD model using an Arcam A2X, the .CATPart model file was translated into a .stl file. The translation tessellates the surface of the model into triangles that closely match the curvature; the smaller the tessellation parameters, the better the .stl geometry will match the original model surfaces. All existing CAD programs allow the saving of 3D models in .stl format which usually requires defining a “sag” and “step” value for an unstructured triangulated surface mesh. For this model a sag of 0.025 mm (0.001 in) and a step of 20 mm (0.787 in) was specified in the .stl file generation. However, the printing device has a beam spot size of 0.25 mm which generates a melt pool of about 0.6 mm in diameter based on the Line experiment discussed in Chapter 4. Any feature in the model smaller than that will not be able to be resolved and will only result in a larger than necessary file size. The mesh quality is important to manufacturing results because a poor translation will appear as facets in the final part which create corners, edges, and stress concentrations that were never part of the original design or analysis.

From there the model was loaded into Materialise Magics to configure the manufacturing layout within the build chamber of the Arcam A2X. This software solution not only helps with the build orientation of the desired parts, but also the design of the support structures. The supports defined in this study are a custom formation of “block” support that is designed to be porous to enable easy powder removal. Initially supports were placed on any downward facing surface that was 35 degrees or less from the horizontal build plane, but after a trial build that critical angle was revised to a steeper slope of 55 degrees or less.

The supports not only provide structural rigidity for the parts, but also assist with thermal management of the build layer. In order to minimize the amount of supports and the subsequent effort of removal, the aft section of the beam was oriented with the aft end closest to the build plate while the forward section was oriented with the forward end closest to the build plate. This orientation keeps the regions of largest thermal mass near the build plate to use it as a heat sink allowing heat from the melt areas to be dispersed more quickly which reduces distortion. A distance of 5 mm was how far the specimens were spaced from the build plate. The beam parts were inclined at 8 degrees so that each section was fairly vertical within the chamber as can be seen in Figure 6.12. This orientation meant that the assembly interfaces would be furthest from where dimensions are most stable closest to the build plate. Any significant distortion from the base to the top of the build will impact the location and shape of the joint surfaces the most and prevent the two halves from fitting together.

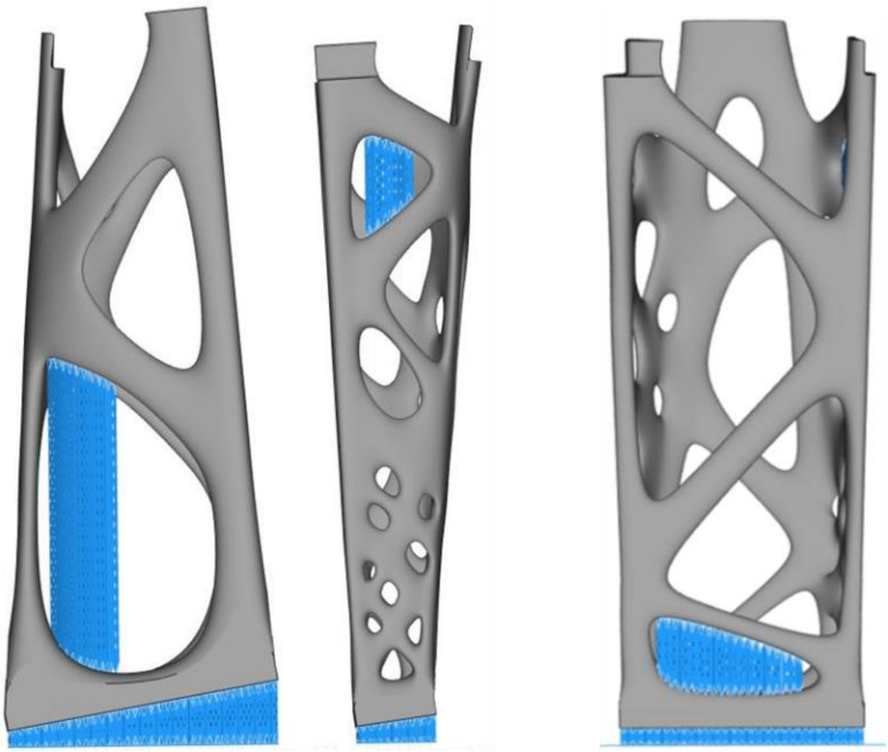

Figure 6.12. Support strategy images for initial trial build configuration with the supports in blue and the parts in grey. (left) side view of aft section, (center) side view of forward section, (left) top view of forward section.

Support features were used to attach the base of the beam sections to the start plate. Perforated and fragmented block supports, as the software identifies them, were the only type of support used throughout the build shown in Figure 6.12, though the parameters for the supports were customized based on previous experience. This would serve as an initial trial build to test the setup with minimal supports. The distortion of overhanging surfaces in PBF additive processes is well documented as described by Smith, C. J., et. al. [4], but the mechanisms are not completely understood due to the large number of process variables to consider. In most cases, the distortion is from solidification taking too long and the melt pool not cooling fast enough. The defect typically continues to worsen with subsequent layers until the build crashes or is identified and stopped by the operator.

With the desired beam components and supports laid out inside the build volume, the .stl models were exported from Magics and imported to the Arcam Build Assembler software for slicing. This software breaks the model into the 2D print layers and encodes the scan strategies for the beam, such as contouring, hatching paths, and hatch rotation. The supports are distinguished separately from the beam models since the Arcam A2X can melt support features with different process parameters from the primary part features as identified in the melt and wafer themes discussed in Chapter 4. By doing this it enables the supports to be weaker and easy to remove from the final geometry which significantly reduces the cost of post processing. The Arcam slicing software finalizes the build into a .abf file which then gets loaded into the machine for execution.

Execution of the trial build was accomplished with used Arcam Ti-6Al-4V powder and it revealed defects caused by insufficient thermal support features in numerous locations shown in Figure 6.13. As the build progressed vertically melting the overhanging regions, more of the melt area was being performed over powder which serves as an insulator. The heat can only escape through the adjacent molten material of that layer which also must cool. This situation retards the cooling rate of the overhanging melted titanium. Instead of the underside of the melted area cooling first, the heat is trapped and the topside cools faster. As the top surface cools faster than the lower surface, the top surface shrinks and contracts causing the edge of the material to deform upwards out of the build plane. The defects in the trial build displayed this behavior which preceded to get worse with subsequent layers before ultimately recovering. How the build was able to recover and complete without crashing is unknown, but it either shows the robustness of the EBM PBF process or the robustness of this non-traditional organic geometry with the process.

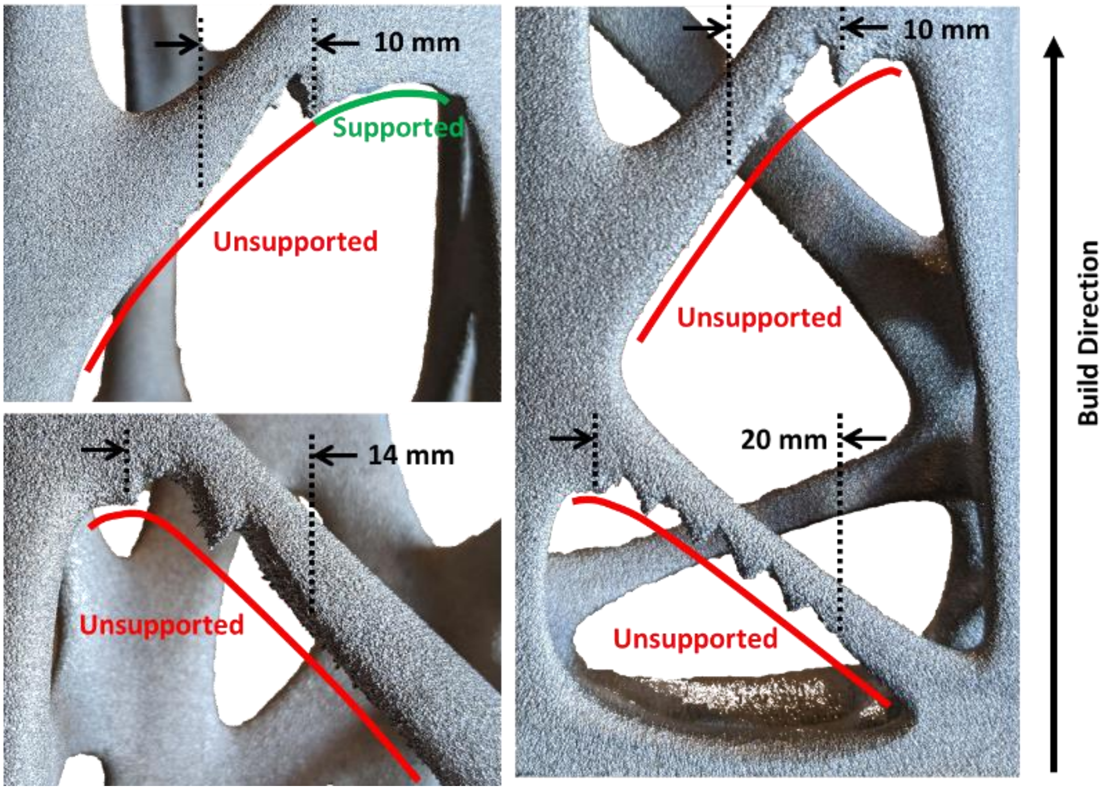

Figure 6.13. Defects resulting from unsupported overhanging negative surfaces in the trial build.

After careful review of the trial build result it was determined that any overhanging negative surfaces less than 55 degrees from horizontal required thermal supports. Unlike Laser PBF processes, the support features do not need to be anchored to the build plate or another portion of the part below it. With EBM, support features can begin as floating geometry, disconnected from anything else, as demonstrated with the rocket motor component build in Section 3.3.3. Per a recommendation from Arcam for best results, all floating supports were initiated 20 mm below the part melt layer. Following this strategy in Figure 6.14, three subsequent builds were completed successfully without the sort of geometric defects experienced in the trial build. Figure 6.15 displays the same regions of the beam as Figure 6.13 from one of the subsequent builds with the revised support strategy. By comparison it does not show any significant geometric defects that were experienced previously with the trial build.

Figure 6.14. Support strategy image for aft/forward section (left/right) final build configuration demonstrating floating support features.

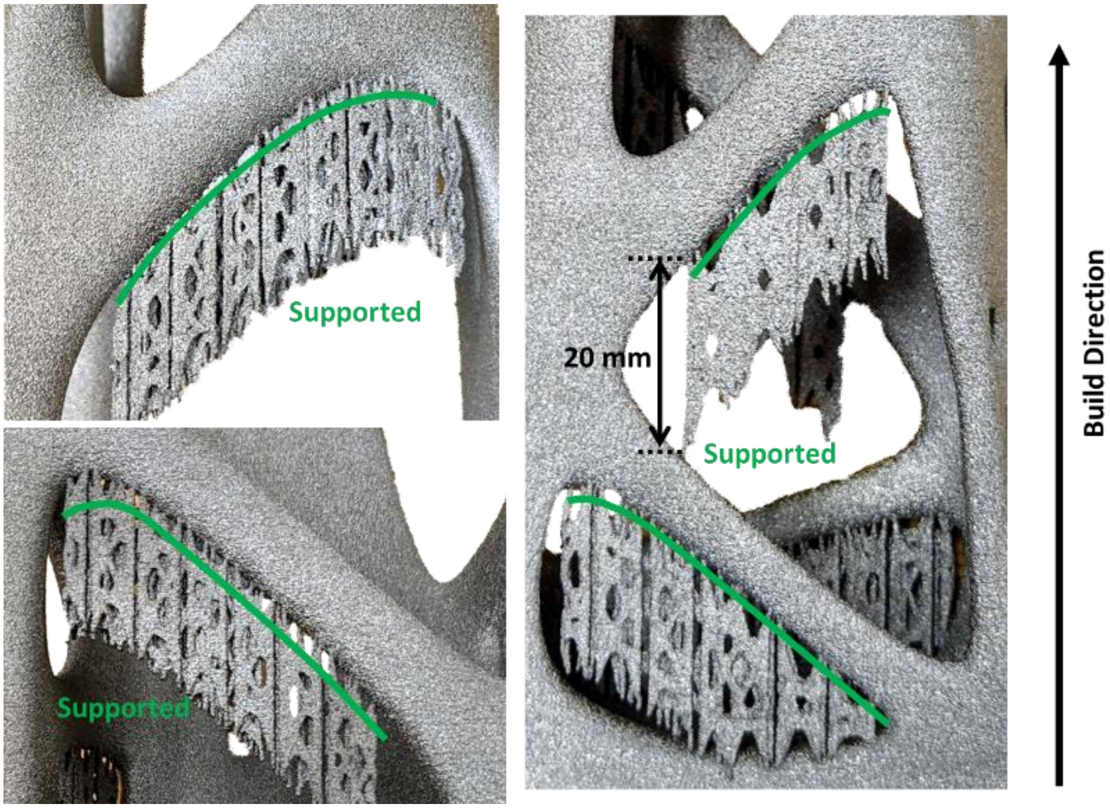

Figure 6.15. Previous areas from trial build with defects now showing corrected by having support features added.

The setup for the manufacturing repeatability experiment consisted of two complete beams per build (front and back), two forward sections and two aft sections displayed in Figure 6.16. In addition, tensile coupons were included to either side of beams and oriented vertically; these will provide insight into the material properties of the printed beams. All build parameters used were provided by Arcam as ‘optimal’ without modification. The build plates were 210 x 210 x 10 mm stainless steel, and the powder was previously used gas atomized Ti-6Al-4V purchased from Arcam. The total build time from the start of heating to the last layer completed was 43 hours and 53 minutes.

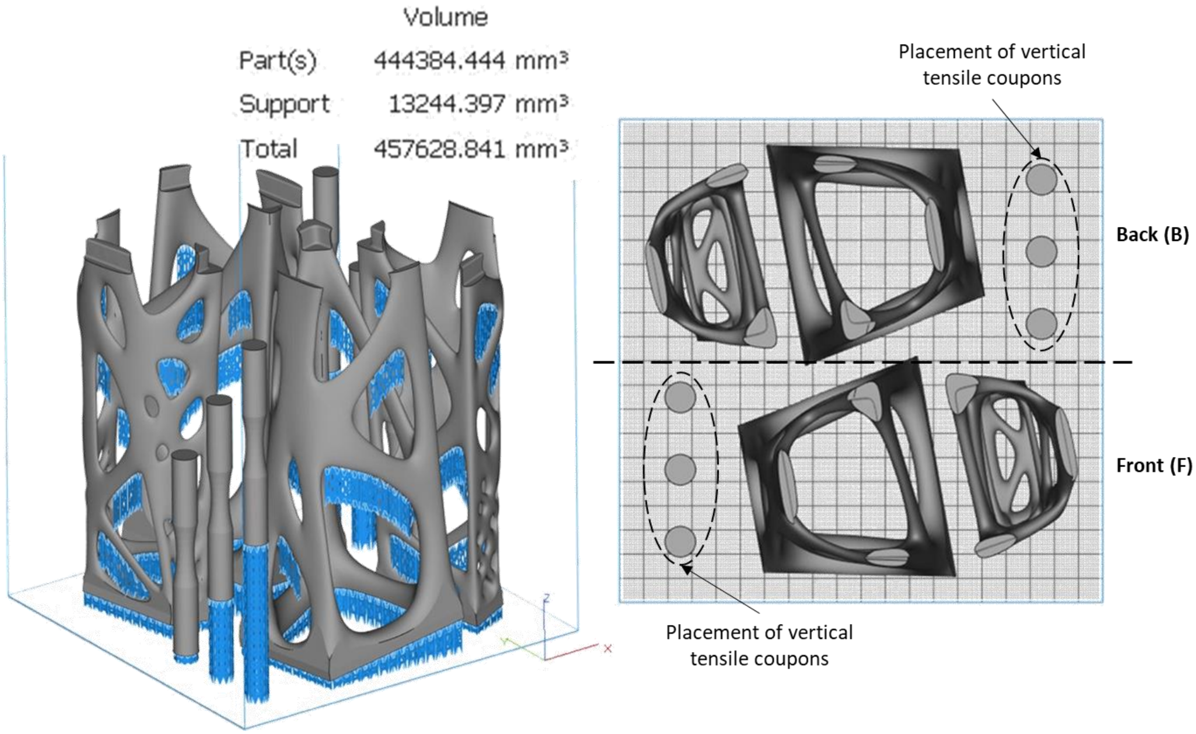

Figure 6.16. Final build configuration with floating support features and build volume layout with a two tapered box beam build arrangement (left) and top view (right).

6.2 RESULTS

In this section, the results of the manufacturing repeatability trials will be shown and analyzed. Three builds were conducted in series from the same batch of used Ti-6Al-4V powder supplied by Arcam. The beam components and tensile coupons were extracted from the powder. After post process support removal, the beam mid-joint interfaces were cleaned and bonded. Six of the total 18 tensile coupons were taken to a lab for material characterization via ultimate strength testing. Separately, the tapered box beam specimens were professionally 3D laser scanned for external dimensional analysis. The final scanned geometry of the printed beams was then compared to the CAD file and across all 6 beam specimens to assess the process repeatability.

6.2.1 *Fabrication*

Upon completion of a build in the Arcam A2X, the vacuum chamber is repressured by the operator. Once equal pressure has been restored, the door lock was released and the chamber door opened. Excess powder within the build chamber was vacuumed to be reused, at the same time the build was raised to reveal the sintered titanium cake that the specimens are buried within (Figure 6.17). The sintered cake, specimens, and stainless steel build plate, together weighed in excess of 23 kg and had to be manually lifted into a trolley to be taken to the PRS. In order to get the specimens out of the powder, the PRS blasted the cake with compressed air mixed with titanium powder through a nozzle that is manually manipulated, similar to a grit blasting station. Since the build plate is stainless steel rather than titanium, none of the parts had to be cut from the plate. The difference in materials make for very weak welds that crack during the cooling phase and allow for removal by hand. Often times the parts separate from the plate on their own during the powder recovery phase without any direct effort.

Figure 6.17. The sintered cake of titanium resulting from a build that is ready to be extracted from the Arcam A2X chamber.

The fabricated components exhibited a rough as-built surface that is typical of the powder bed fusion process. From experience additive part curvatures can often times appear faceted like a cut diamond which is an artefact of a bad model-to-STL conversion with poor values for the sag and step parameters. The entire surface curvature and transitions of the parts in this experiment were smooth without facets which validates the correct .stl mesh parameters were utilized. It was observed that surfaces opposite the build direction that were not supported were rougher than parallel or top surfaces. Printing the parts at an angle such that no final surface was parallel with the build plane resulted in a fairly uniform surface condition.

Once the excess powder was removed from the specimens the parts were prepared for assembly. First, the supports were manually removed with dykes and the ends of the beam, both forward and aft, were ground flat with a belt sander. Where small nubs remained at locations where support features joined the specimen these were smoothed using a tungsten carbide rotary tool. It was thought that the design and additive manufacturing of the beam in two halves due to the build volume restriction would present a challenge for assembly of the final beam. An interface at three locations was designed with a clearance gap of 0.1 mm to account for deviations from the CAD model in the final geometry. From the manufacturing results it was determined that the designed clearance was sufficient to ensure easy assembly with a slight friction fit.

Due to the organic shape of the structure and lack of exterior flat surfaces for traditional ease of assembly, a bonding strategy was developed and employed to ensure a good chemical and mechanical bond. For that reason, the interfacing surfaces were solution cleaned with acetone prior to being sanded with a diamond rotary tool to remove any oxidation or contaminants, then the interfaces were solution cleaned again. The two parts were then bonded together using JB Weld and allowed to cure for more than 24 hours at room temperature. The bond quality is not expected to be sufficient to actually withstand the design loads, so future work will include six steel MS35265-19 bolts and MS21043-04 hex nuts to be added to ensure the joints will not be the failure point during physical testing. An assembled full beam specimen is shown in Figure 6.18.

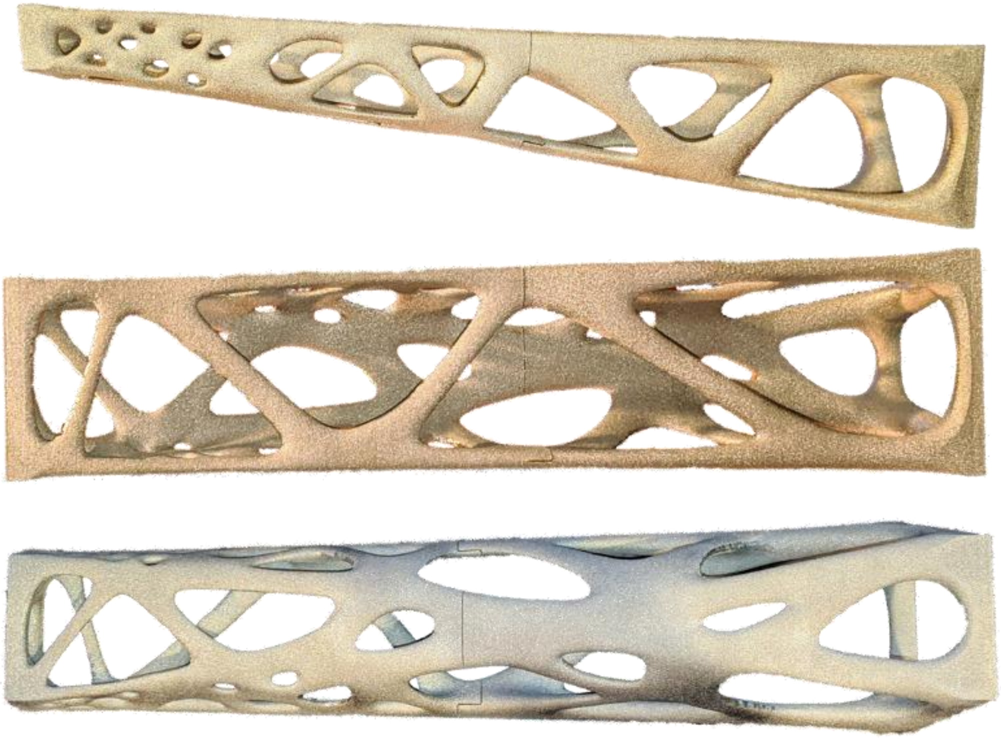

Figure 6.18. Side, top, and bottom view images respectively of the titanium tapered box beam specimens.

6.2.2 *Tensile Test Results*

Within each of the three builds, six round tensile specimens (ASTM-E466 9 mm diameter) were produced in the vertical orientation, three alongside each beam specimen. One of the three was selected for tensile testing to help assess the material strength of the beams, while the others were set aside for future work. The tensile specimens that were tested were located about midway between the start plate and the top of the build with supports that extended to the plate. For post processing, only the supports were removed and no smoothing operations were performed such that they would be tested in the as built condition. It is evident from the tensile specimen imaged in Figure 6.19 that they possess the same rough surface as the beams they were printed with. The tests were conducted using an Instron 5585H (250kN capacity) machine with Instron mechanical wedge grips (100kN capacity), an Instron 2525-174 load cell (250 kN capacity), and an Instron 2630-101 (10 mm gauge length) extensometer spanning the middle of the tapered section. Each specimen was loaded to ultimate and the measured section had a length of 25.4 mm and a cross-sectional area of 63.62 mm^2.

Figure 6.19. Image of tensile specimen in lower grip of Instron machine with digital extensometer attached to the tapered test section.

Overall results from the tensile testing are displayed in Table 6.9 and shown in Figure 6.20. Out of the six specimens, the average failure load was 72.8 kN with a standard deviation of 600 N which shows that the specimens were fairly consistent across the three builds. The average tensile stress at maximum load was very high at over 1144 MPa, but with only a 3.8% elongation it indicates the material is very brittle. The brittleness is likely due to the oxygen pickup of the titanium powder over time with multiple reuse [30]. The yield stress at a 0.2% offset was also very high averaging 1096.9 MPa, and only 47.5 MPa difference between that and ultimate. This small difference also indicates a low ductility brittle material.

Table 6.9. Average measurements from six tensile specimen tests.

Measure	units	Average	Std Dev
Maximum Load	kN	72.8	0.6
Tensile stress at Maximum Load	MPa	1144.4	8.7
Modulus (Automatic)	MPa	102851	1961
% Elongation	%	3.80	0.67
Tensile stress at Break (Standard)	MPa	1134.2	11.1
Tensile stress at Yield (Offset 0.2 %)	MPa	1096.9	9.1
Tensile strain (Extension) at Maximum Load	mm/mm	0.036	0.006

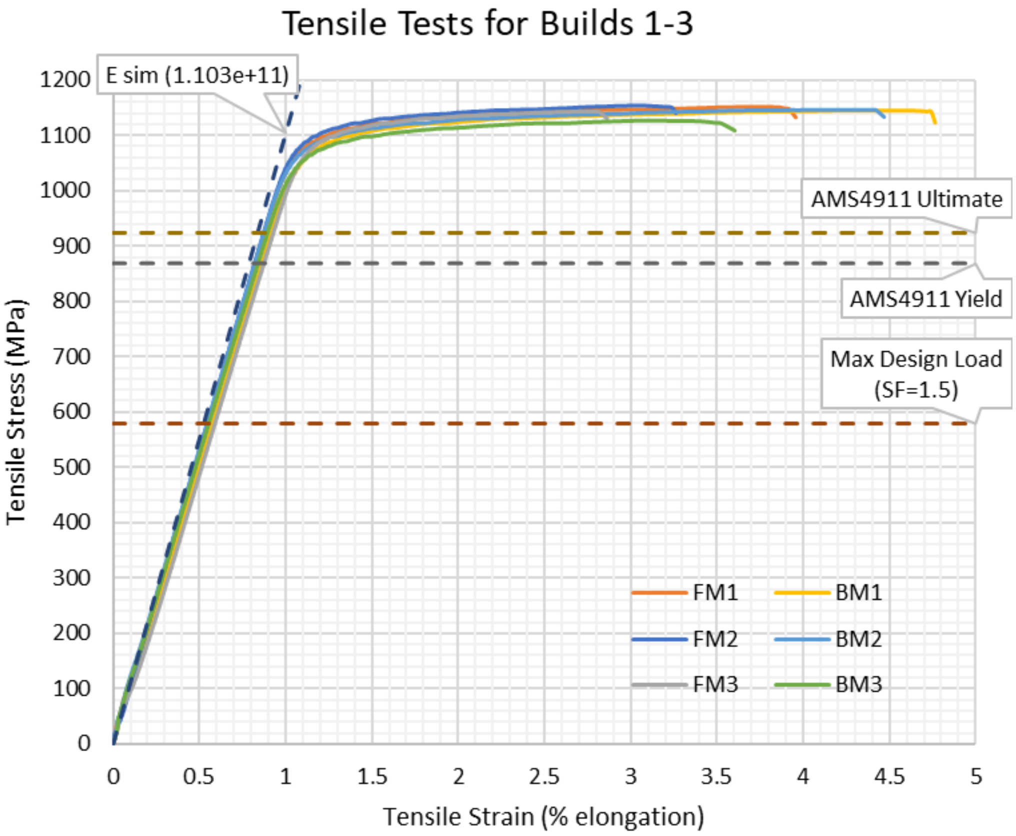

Figure 6.20. Tensile test results for the six tensile specimens.

Nevertheless, when comparing these results to the AMS4911 values used in sizing the beams it shows that the AMS values were quite conservative. Recall from section 6.1.1 that a traditional forward strut box assembly would be manufactured using sheet metal or machined plate, so the assumed material properties for the topology optimization and stress analysis were 920 MPa ultimate and 869 MPa yield, with a required 1.5 maximum principal stress factor of safety leading to a maximum principal stress allowed of 579.2 MPa (84 ksi). Based on Figure 6.20 the material shows a margin greater than 200 MPa for ultimate and yield strengths and that boosts the margin of safety to 1.9. The simulation analysis used a Young's Modulus of 1.103e+11 which shows to fairly closely match the actual slopes that averaged 1.02e+11.

An aspect of these builds was to also look at differences between multiples of the same parts manufactured within the same build volumes. From the Step-Ramp tapered build experiment discussed in Chapter 5, the machine may vary the hatching scan parameters between identical parts, even within the same build layer. Those differences lead to differences in the final geometry and similar effects were seen in the material property tensile data. The specimens were labeled with three characters that identify their location within the build chamber and which build they were manufactured in. The first letter identifies the specimen as being in the front (F) or the back (B) of the build chamber, while the second letter denotes the build height as middle (M). The number identifies which of the three builds it was manufactured. A similar nomenclature was used to identify the beams without the second character build height identifier.

Data from the three builds was separated into build location and compared in Table 6.10. Here one can see some clear differences, most notably in the elongation which shows the front specimens have a 21.5% less elongation. The front specimens also have a 1.4% higher static strength before yielding and broke at 1% higher load. Therefore, specimens in the front of the chamber will likely be more brittle than those at the back with the heavily reused material, and this trend likely will extend to the tapered box beam specimens.

Table 6.10. Average measurements from six tensile specimen tests grouped into build volume location Front and Back.

Measure	units	Front	Back	% diff
Maximum Load	kN	73.1	72.5	0.9%
Tensile stress at Maximum Load	MPa	1149.5	1139.3	0.9%
Modulus (Automatic)	MPa	103764	101938	1.8%
% Elongation	%	3.34	4.25	-21.5%
Tensile stress at Break (Standard)	MPa	1142.5	1125.9	1.5%
Tensile stress at Yield (Offset 0.2 %)	MPa	1104.8	1089.1	1.4%
Tensile strain (Extension) at Maximum Load	mm/mm	0.032	0.039	-19.4%

6.2.3 *Scan Results*

The assembled beam specimens were sent to be professionally scanned by Digital Scan 3D. This company used a Kreon Ace Skyline blue laser 3D scanner which specifies an accuracy of up to 9 µm. Each of the six parts were scanned numerous times from different angles attempting to capture as much of the organically shaped geometry as possible. The various scans were assembled into an .stl file; however, it was impossible to scan 100% of the beam surfaces and some internal regions were not able to be scanned as can be seen in Figure 6.21. The .stl files were loaded into a software program called GOM Inspect in order measure dimensions of the scanned geometry and analyze the surfaces. Analysis of the scans was conducted by examining the total length and total volume. No datum system was previously established for the beams and there are no significantly straight or flat features to create one; therefore, these parameters were compared to the nominal CAD geometry based on an overall best fit as demonstrated in Figure 6.22.

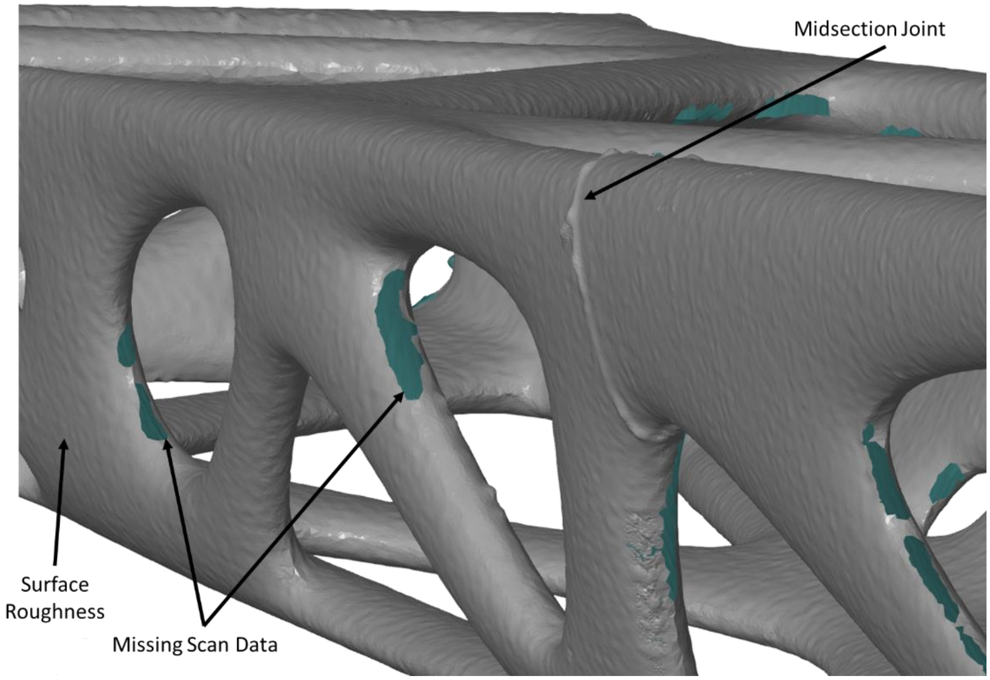

Figure 6.21. Example section of scanned STL data using specimen 1F

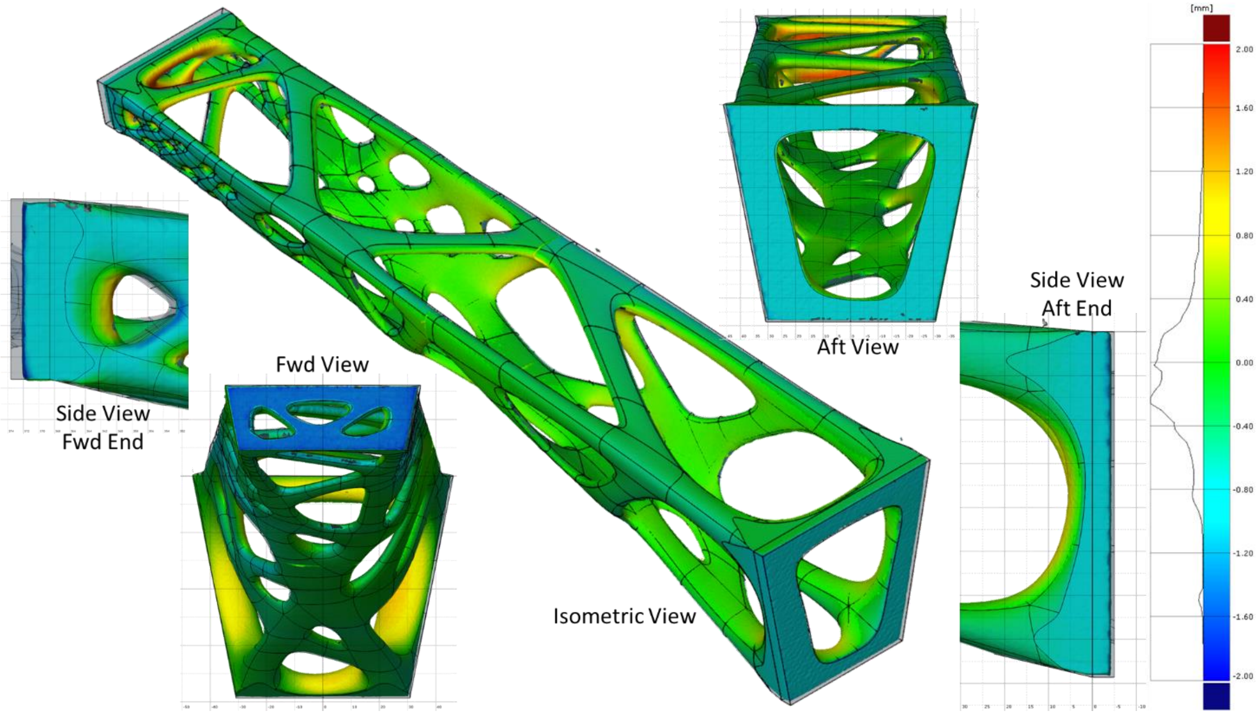

Figure 6.22. Example of geometric best fit surface analysis comparison to nominal CAD using scan results of specimen 1F (blue indicates inside the CAD geometry and yellow outside). The scanned surface is overlaid with a transparent CAD model.

A surface best fit from the scanned geometry to the CAD model had good results with alignment to the CAD surfaces with no outliers. The alignment primarily matched the middle of the beams such that the largest differences showed at the forward and aft extremities. In general, the all of the beam specimens were smaller than the CAD model. When overlaid with the CAD model, the scanned outer surfaces were equal to or inside the nominal surface implying the printed beams had thermally contracted as they cooled. The contraction is most notable at the forward and aft ends of the beams and can be seen in the side views of Figure 6.22 where the transparent grey CAD surface protrudes beyond the colored scan surface. Scanned surfaces protruding from the CAD model are seen primarily on the inner surfaces of the beam.

The thermal shrinkage of the titanium beams can be quantified with the overall length measured from the scanned surfaces. From the CAD geometry the designed nominal length from the aft plane to the forward plane was 378.59 mm. The longest specimen(s) was 3B (build: 3, location: back) and 1B (build: 1, location: back) which both measured equally at 376.4 mm, and 3F (build: 3, location: front) was the shortest specimen that measured 376.14 mm giving a deviation range of only 0.26 mm. Average length for the six beams was 376.29 mm, which is 0.6% (2.19 mm) shorter than nominal, but with a standard deviation of only 0.036% or 0.10 mm (0.004 inches). This indicates that the EBM process is repeatable and could more closely match the CAD model if it is compensated for thermal expansion at the elevated build chamber temperature.

While the scanner was not able to completely scan all surfaces, a total volume measurement was still possible and could be compared with the nominal CAD volume of 222.11 cm^3. After reviewing the length data, it is no surprise that the largest and smallest volume specimens were 3B and 3F respectfully. The volume of 3B measured 214.29 cm^3 while the 3F measured 212.80 cm^3, giving a range of 1.49 cm^3 (0.09 in^3). At an assumed titanium density of 4.43 g/cc that would be a weight variation of 6.6 grams (0.015 lbs). The average volume for the six beams was 213.43 cm^3, which is an 8.68 cm^3 difference from nominal or a 3.9% reduction. This is not an insignificant amount and further stresses the need for compensating the CAD models for thermal expansion prior to converting it to an .stl file to be manufactured. Similar to the length measurements, the standard deviation of the volumes was also very small at only 0.59 cm^3 between the six specimens. Figure 6.23 shows the variation of the measured lengths and volumes and how they compare to the average. Because the variation is so small compared to the deviation from nominal, the design CAD values could not be included in the plot.

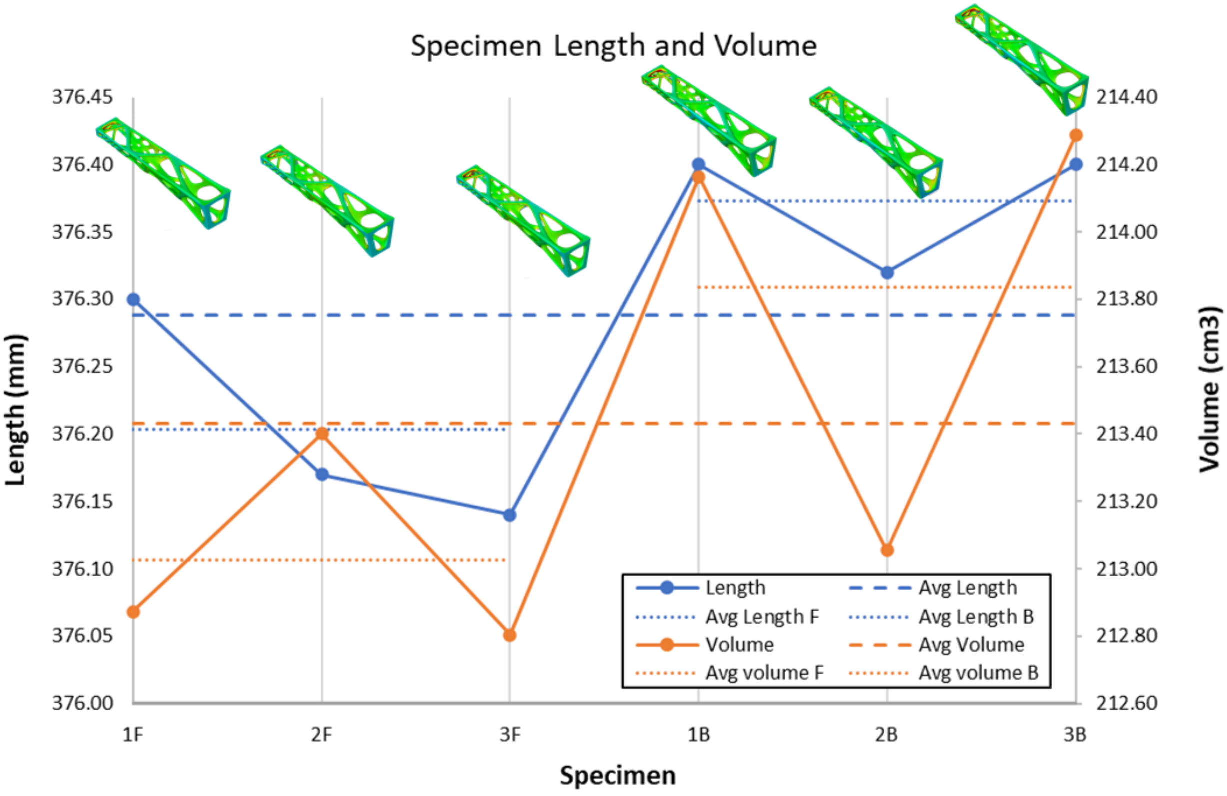

Figure 6.23. Plot of the six beam specimens' total length and total volume as measured from 3D scan .stl files grouped by build location.

In Figure 6.23 the specimens were grouped by location within the build chamber rather than the build number which displays the beams printed in the front of the chamber followed by those printed in the back. From this perspective it can be seen that there are significant differences based on build location. For length, all of the front specimens were shorter than those in the back, and while there was one back beam that had a volume measurement similar to the front beams the average volume of the back beams was higher. Table 6.11 displays the average and standard deviation of the specimens grouped by build location. Amongst those in the same location the variation is smaller than the overall range.

Table 6.11. Average length and volume measurements grouped by build location.

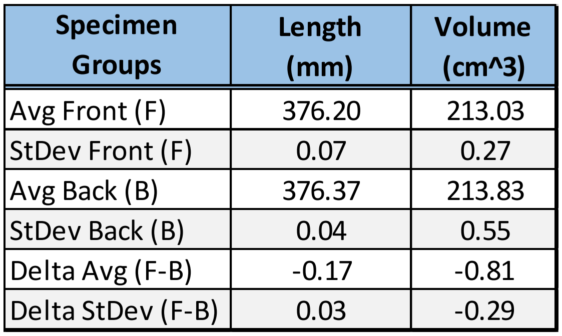

Specimen Groups	Length (mm)	Volume (cm^3)
Avg Front (F)	376.20	213.03
StDev Front (F)	0.07	0.27
Avg Back (B)	376.37	213.83
StDev Back (B)	0.04	0.55
Delta Avg (F-B)	-0.17	-0.81
Delta StDev (F-B)	0.03	-0.29

Figure 6.24 is a similar plot to Figure 6.23 except that the specimens are grouped by build number in order to compare the variation in length and volume from build to build. Unlike the grouping by build location, this plot does not reveal any discernable trends. It could be that there is not enough data to reveal a trend from build to build in geometric accuracy, but there is no reason to suspect that there might be one. Overall, it still shows the variability in length and volume are very small compared to the difference to the CAD geometry.

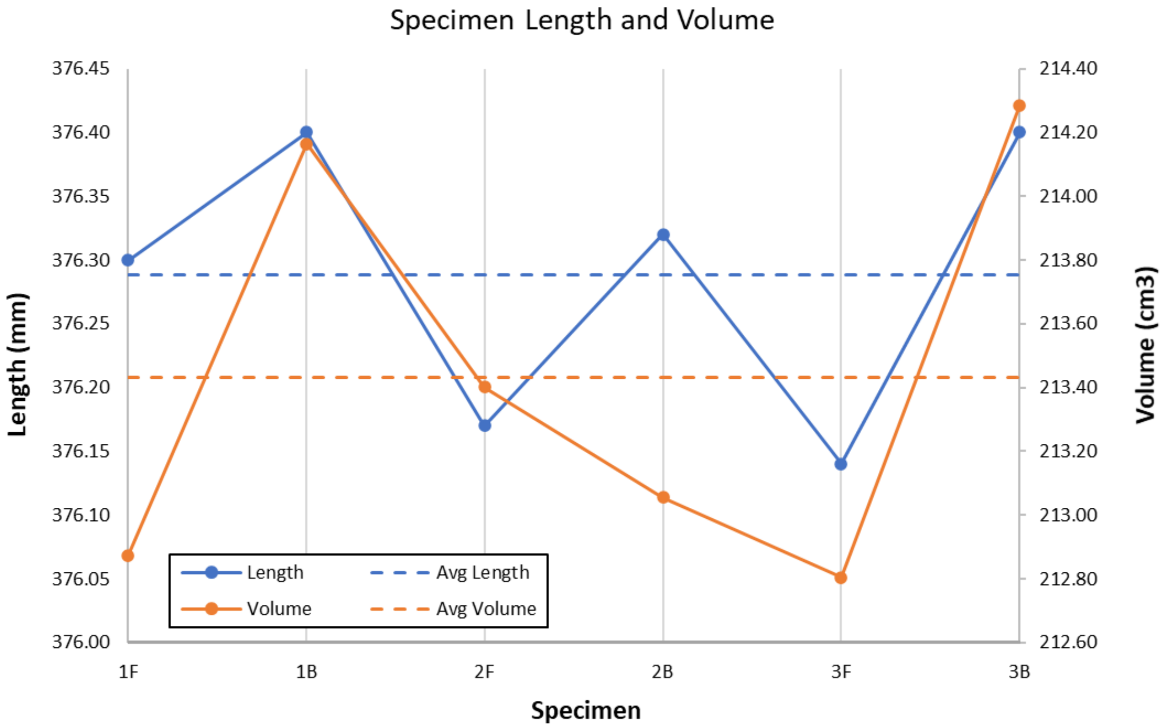

Figure 6.24. Plot of the six beam specimens' total length and total volume as measured from 3D scan .stl files grouped by build location.

6.3 DISCUSSION

An Arcam A2X was utilized to produce six topology optimized tapered box beams from gas atomized Ti-6Al-4V powder to assess manufacturing repeatability of the EBM process. The design requirements that were provided led to the generation of a design space where a 3D topology optimization was performed. The first run however did not achieve a desirable result and the shape control target had to be removed to further simplify the problem. This was already a heavily simplified aerospace engineering problem with very few load cases and an acceptable result was only achieved with the fewest number of objectives specified (maximize stiffness with a mass target). This demonstrated that topology optimization algorithms and software need further improvement in order to be able to converge with more complex 3D problems faced in industry.

On the other hand, topology optimization greatly increased the speed of the design for additive manufacturing (DfAM) process. Without topology optimization to use as an example and starting point, the total process time to achieve a final design would take much longer. It is difficult for an engineer to look at an empty design space and conceive a marketable design that they have not encountered previously. Design for additive manufacturing is a critical consideration in the design process where one must consider: the energy source, the feedstock material, the maximum build volume, the build orientation, where supports will be needed, and how supports will be removed. These are fundamental aspects that must be taken into account prior to and during the design of any additive part.

Software that enables rapid iteration between design and FEM analysis, one that blurs the traditional line between the roles of a designer and stress analyst, is essential to making DfAM cost effective. In this work the native CAD geometry was able to be meshed, simulated, and analyzed without the need to transfer the model to another platform. That not only saved time, but also reduced the risk of errors by eliminating numerous model translations between formats and design update cycles. Once the organic design was finalized the process of translating it to a .stl, setting up the build in Magics, and slicing it was straight forward.

Prior to the experimental builds being conducted, a trial build was performed to fine tune the support strategy. It was previously thought that the sintered powder bed could print overhanging part geometry at lower angles than 45 degrees from the horizontal build plane due to the stability provided by the sintered powder. However, numerous overhang regions distorted causing significant geometric defects, likely due to the difference in solidification rate between the top and bottom of the melt pool. The defects compounded layer after layer, but eventually each one recovered and the build did not crash. Once support structures were added to the overhanging surfaces that were less than 55 degrees from the horizontal, the defects went away. *The ideal support strategy for a build is an area of additive manufacturing that still requires trial and error and is in need of more research to understand the mechanisms driving the need and placement for the sacrificial geometry.*

All three builds and beam sections were printed successfully and the beams were able to be assembled. That alone demonstrated that the EBM PBF build process was geometrically stable enough for a CAD model to have an interface clearance of 0.1 mm at the top of a build and still allow for assembly. This stability was also seen in the scan-to-scan variability of the overall length where the standard deviation amongst the six beams was only 0.1 mm. However, since the CAD model was not compensated for thermal expansion at the build chamber temperature, the parts were shorter than nominal on average by 2.19 mm or 0.6% end to end.

The most significant result matched previous experiments where there was more variability from part location within the machine than there was from build to build. This is likely due to each part within the build having a different hatching history. Based on the results from the tensile specimens *it is also reasonable to assume the part location, and subsequently the different hatching history, has affected the material properties and the micro structure of the titanium.* Since the build to build variation from the same location within the build chamber was even smaller than the overall variation, if the hatching history for identical parts within the build volume can be controlled and duplicated, then we should see the process become even more stable.

Chapter 7. SUMMARY AND CONCLUSION

The aerospace industry has been investing heavily in metal additive manufacturing which includes some of the biggest names like GE, Boeing, and Airbus. This industry requires a high level of manufacturing and materials process control. What makes additive unique is that the part and material properties are being created at the same time which jumbles together a large number of process variables. With traditional manufacturing the process variables are broken up into the various steps in a product value stream, each with a limited number of process variables that are easier to control. By combining the material and part manufacturing into a single step, there remains a lot of uncertainty for how to control all of the interdependent variables. Process control, and thus manufacturing repeatability, in this industry is directly linked to product safety. Optimistically, additive manufacturing could bring about the next step change in aircraft capability, however a sufficient number of successful examples are still needed.

The work described here-in demonstrated the repeatability of the electron beam melting powder bed fusion additive process in manufacturing a topology optimized tapered box beam from Ti-6Al-4V using an Arcam A2X located at the University of Washington Mechanical Engineering department. It began with a literature review of additive manufacturing, the EBM process, design for additive manufacturing and topology optimization. There was an examination of the metallurgy, material properties, and potential defects. That was followed by the description of the materials, methods, and procedures to be used in experiments that were tested with an early rocket motor component case study.

Once proper protocol had been established, a build was commissioned to take a fundamental look at the resulting melt topology of the default Arcam ‘optimized’ melt and wafer themes. Then the melt area to analyze was scaled into two and three dimensions by manufacturing discrete step and sloped specimens that enabled the analysis of intra-layer melt quality correlated with increasing thermal mass. A final experiment scaled the build to actual component manufacturing that was designed specifically for the EBM additive process. That investigation not only examined the intra-build geometric variability, but also the build-to-build variability of an organically shaped tapered box beam.

7.1 SUMMARY

The EBM additive technology utilizes an electron beam as the energy source to melt metal powder within a vacuum environment. The machine takes a software build file that was prepared from a .stl model of the geometry that the operator wishes to manufacture. Several setup and calibration steps must then take place: 1) to identify the size of the start plate and the material, 2) select the models and associate melt themes, 3) load the powder, 4) level the build plate, 5) calibrate the fetch powder quantity, 6) pull the vacuum, 7) center the beam, 8) calibrate the beam focus, and finally 9) press the go button. Each layer begins with a preheating phase to maintain an overall constant heat energy and sinter the powder, which is followed by the melting phases. Two themes are employed with different process parameters for melting the supports with a wafer theme and the part with a melt theme. The melt process occurs in two steps starting with the contouring outline scan and the in-fill hatching scan. There are many types of defects that can occur with this process, but almost all relate back to either too much heat input or insufficient heating. Large geometric defects can occur with overhanging structures if insufficiently supported.

The typical powder particle diameter ranges from 45-105 µm with an average around 75 µm. Microstructure of additively manufactured EBM Ti-6Al-4V consists of dominate prior β columnar grains with a high amount of grain oriented vertically along the Z axis (build direction) with α + β lamellar structure (mainly Windmanstätten, or “basket weave”) inside the β grains and organized into discrete groups of α lamellae with similar thicknesses [19]. Operation of the Arcam A2X followed the operator's manual procedures carefully for build setup, extraction, and powder handling. It consists of a control cabinet on the left and a chamber cabinet on the right. Within the cabinets are a cooling system, beam column electromagnetic coils, the vacuum turbo pumps, and electronic components. In the control cabinet is a 60kV power supply that generates the power acceleration needed for the electron beam. Electrons are emitted from the top column above the build chamber which holds a filament that consists of lanthanum hexaboride. The printing was conducted according to 'optimized' default parameters provided by Arcam with no adjustments. The chamber door on the right cabinet seals the build chamber and contains an observation window. The operator is protected from radiation based on the door thickness, the external shell plate and lead glass.

Metrology of the various test specimens was conducted with a Keyence VR-3100 and a Kreon Ace Arm and Skyline laser scanner. The Keyence was used for small specimens and employs fringe projection technology with triangular ranging to instantaneously measure height, length, angle, volume, etc. of an object. This system allowed for the detailed characterization of the specimen topology without a lot of difficult calibration. The 3D laser scanner was used for measuring the larger beam specimens which consisted of generating various point clouds at different angles and combining them into a single .stl model of the file geometry. That geometry could then be analyzed using quality assurance software to compare the measurements to each other and the original model.

The purpose of conducting the Line experiment was to provide a fundamental look at the resulting melt based on the process parameters programed into the melt and wafer themes. During a typical component build it is difficult to see the nuances of what as actually happening with the beam power, how the beam moves, and its interaction with the surrounding powder. This is because the melting happens so quickly and the high temperature vacuum chamber makes it very difficult to install additional monitoring equipment. By creating 4 mm single beam width melt lines on top of sintered powder in different directions, the topographies of the melt could be characterized. The experiment was designed to duplicate the results of another experiment as reported by Jamshidinia, et. al. [31] who produced similar short single melt lines in titanium powder to investigate the effects of process parameters on the heat distribution with a moving EBM heat source. However, here the influences of different electron beam scanning themes was studied by measuring the melt pool widths, depths, and surface topographies.

The Step-Ramp experiment was conducted for the purpose of demonstrating the variability from multiples of the same CAD geometry and detecting possible sources. The designed build contained a set of four different CAD geometries made from discrete step and shallow ramp models that were repeated four times throughout the build chamber for a total of 16 specimens. Each set of two steps or ramps came in different thicknesses where the first Step-Ramp pair varied in height from 100 μm to 700 μm, and the second Step-Ramp pair varied in height from 200 μm to 1400 μm. The starting ramp and step thickness values were selected because the Arcam A2X machine specifies a layer thickness of 50 μm, therefore 100 μm represents two print layers. Generally, it is not best practice to try to print such thin geometry in metal because the distortion can be significant enough to crash the build, however that was not the case here and the build was successful. Each of the 16 specimens were imaged and had each visible layer characterized for surface topography and roughness.

Since design engineers tend to adhere to designs they have encountered previously, it is difficult to mentally bypass barriers that have been imposed by traditional DfMA fabrication techniques. With an empty design space, and an AM machine, it is challenging to conceive of a design that cannot be manufactured another way. Therefore, it is important for engineers to find additive examples to shift mindsets and change perspectives. This is where topology optimization is able to provide the necessary assistance to aid the additive designer to successfully employ DfAM techniques. Topology optimization can generate seemingly infinite geometric examples depending on the targets, constrains, and boundary conditions, that could satisfy some or all design requirements. While it has been utilized in aircraft and aerospace structures for decades to optimize stiffener layouts and sizing, now combined with an AM machine, it can be an even more effective tool for generating nontraditional configurations of common structures that make best use of material and space.

Based on the lessons learned in the Line build and Step-Ramp build experiments the tapered box beam experiment was conducted to explore the application of an organically shaped topology optimized cantilevered beam structure in the place of a traditional tapered forward strut box beam of an engine pylon. The design space had to be scaled down to fit in the chamber of the Arcam A2X as two parts. It was conducted in order to demonstrate the manufacturing repeatability of the design for additive manufacturing structure, where multiples of beam parts were printed out of Ti-6Al-4V powder and default process parameters. The work flow of the optimization process, design strategy, manufacturing, and assembly was presented and it serves as vital information for any additive manufacturing engineer who must design for the additive EBM process and understand how repeatable the process is at manufacturing capable products. A 3D topology optimized, organically shaped, asymmetric solution was generated using maximum stiffness criteria, which was followed by a CAD design and finite element stress analysis for maximum stress criteria to ensure the result would meet the design requirements. Two complete beam specimens were arranged in the build chamber and that build was repeated three times. After assembly, the beams were 3D laser scanned and analyzed for variation.

Each subsequent experiment in this work built upon the previous one, providing new understanding of the EBM process before scaling up to eventually building engineered components. The overall method ended up with new discoveries about the sources of variation in the process at different scales. The results of these experiments can provide real meaning and value to the science of metal additive manufacturing and to industries that wish to implement the technology in a safe and controlled manner.

7.2 CONCLUSION

The series of experiments conducted in this work, including the rocket motor component build, delivered many valuable conclusions. From the case study, it provided a means of learning the EBM process and how to safely operate the machine and handle titanium powder. It demonstrated the capability of nesting large geometry in an EBM machine and not needing to anchor it to the build plate or other components within the build. The support strategy that was tested helped to show the dilemma of making support features too robust to remove easily, where as if they had been made with less material it is unknown at which point the build would not be successful. It highlighted the lack of analytical understanding of the need for support features, and that this part of metal additive manufacturing is still largely trial and error.

From the Line experiment the geometric variability in the melt theme and wafer theme was shown to be significant enough to impact design. An engineer wanting to create small features can only do so to a certain size, and the machine will deliberately undersize melt lengths by 200-300 µm. When specifying the design parameters for support structures it is important to know that anything manufactured with the wafer theme will be 100-400 µm longer. Therefore, a designed gap in support geometry of 0.4 mm or smaller will likely be closed off, and that lesson was carried forward into the rest of the experiments.

The Line experiment also confirmed the stationary spot melting nature of the contour scan and that it was automatically selected with the default process parameters. The theme selection was determined to actually be done in the Arcam Build Assembler software for creating the build file and not in the machine control setup for process theme selection. The characteristics from the Line experiment can be used to validate numerical models and simulations of the heat/energy application as it is associated with the observed build characteristics.

The Step-Ramp experiment showed how well EBM creates four sets of the same geometry in different locations and heights within the build chamber; however, no two specimens were the same or matched the CAD geometry. The hatching scan history of each part was found to be important for manufacturing repeatability such that it must be better controlled for identical parts within the build chamber. Initial melt layers up to 300 μm (6 layers) contain heavy porosity so the down skin surface of all parts will contain poor strength properties. A designer must consider the build direction in their design such that up to 300 μm of any downward facing surface either be removed via post processing, or that amount of additional thickness is added and not expected to carry high stress.

Topographically, the variation in the melt peaks on the top layer surface means any given hatch line may vary by as much as 100 μm which is greater than the average powder particle size and twice that of the layer thickness. That level of variation in the top melt must certainly affect the following layer since the beam scan is melting an unknown random thickness of powder that could be as much as 3 layers deep. Specimens closer to the build plate showed much less variation in maximum height with S_z pointing also to the 300 μm layer thickness where the roughness became more consistent. If possible, it would be best to orient parts such that critical features for larger assembly are closer to the build plate which was done in the case of the tapered box beam experiment which placed the ends at bottom of the build; though that was also done because those regions of the structure contained the largest thermal mass and would benefit from the added cooling provided by the build plate.

From the topology optimized tapered box beam experiment it demonstrated the repeatability and robustness of the EBM process at manufacturing a DfAM organic shape. Despite the design requirements reflecting a heavily simplified aerospace engineering problem, the first topology optimization run containing a shape control did not achieve a desirable result. Only once the optimization was reduced to its most basic target of maximizing stiffness was a usable result attained. It showed that topology optimization algorithms and software need further improvement in order to be able to converge with more complex 3D problems faced in industry. While their results can still only serve as a guide for the practicing design engineer, it will greatly increase the speed of the design for additive manufacturing process. Also, software that enables rapid iteration between design and FEM analysis, is essential to making DfAM cost effective.

It was important to test the support strategy with a trial build prior to the experimental builds in order to fine tune the support strategy. Since the sintered powder bed could not facilitate melting overhanging part geometry at smaller angles than 55 degrees from the horizontal build plane, numerous overhang regions distorted causing significant geometric defects. Those defects were likely due to the difference in solidification rate between the top and bottom of the melt pool. Once support features were added to those overhanging regions the defects went away, again highlighting that the ideal support strategy for a build is in need of more research to understand the mechanisms driving the need and placement for the sacrificial geometry.

All three builds of the tapered box beams printed successfully and were able to be assembled showing that the EBM build process was geometrically stable enough for an interface clearance of 0.1 mm to be located at the top of a build. That level of stability was also seen in the scan-to-scan variability of the overall length where the standard deviation amongst the six beams was only 0.1 mm. To get a better comparison back to the nominal CAD model, it should have been compensated for thermal expansion at the build chamber temperature prior to converting it to a .stl. If that had been done the printed beams would not have been shorter than nominal by an average of 2.19 mm or 0.6% end to end.

The most significant result from the beam experiment matched the Step-Ramp experiment and the tensile test data where there was more variability from part location within the machine than there was from build to build. It is the different hatching history experienced by each identical part that is the key driver of these differences, much like weld sequencing for a large weldment. By looking at the variation of the top surface melts in the Step-Ramp experiment and compounding that variation layer after layer for a full build height, it is easy to conceive of this mechanism being the cause. *The different hatching histories not only affect the dimensional deviation, but also variability in the material properties and likely the microstructures.* The hatching history for identical parts within the build volume must be controlled and duplicated to ensure the process more stable and repeatable.

7.3 RECOMMENDATIONS FOR FUTURE STUDY

Based on the experimental results, there is much more work to be on one several fronts.

- Most notably is the need for further understanding the EBM hatching scan strategy and how to control the infill parameters to improve variability of identical parts within the same build volume. That will also help to stabilize the geometric variation and material properties.

- Another highlight of this series of experiments is the need for an analytical optimization model for EBM support features. Automating the prediction of support locations and surface area required would be a huge benefit to many industries and reduce the cost of AM.
- As for the experiments reported here, a future investigation would involve a microstructure analysis of the Line, Step-Ramp, tensile coupons, and Beam specimens.
- For mechanical properties the tapered box beams should be tested to ultimate strength which would validate the combination of the DfAM process involving topology optimization and EBM additive manufacturing technology. However, based on the stress analysis and expected material properties of the beams, a test rig is likely to be expensive in order to react the necessary loads to fail the structure.

BIBLIOGRAPHY

1 Sames, W. J., List, F. A., Pannala, S., Dehoff, R. R., & Babu, S. S. (2016). The metallurgy and processing science of metal additive manufacturing. *International Materials Reviews*, 61(5), 315–360. https://doi.org/10.1080/09506608.2015.1116649

2 Schoinochoritis, B., Chantzis, D., & Salonitis, K. (2017). Simulation of metallic powder bed additive manufacturing processes with the finite element method: A critical review. Proceedings of the Institution of Mechanical Engineers, Part B: *Journal of Engineering Manufacture*, 231(1), 96–117. https://doi.org/10.1177/0954405414567522

3 Herzog, D., Seyda, V., Wycisk, E., & Emmelmann, C. (2016). Additive manufacturing of metals. *Acta Materialia*, 117, 371–392. https://doi.org/10.1016/j.actamat.2016.07.019

4 Smith, C. J., Derguti, F., Hernandez Nava, E., Thomas, M., Tammas-Williams, S., Gulizia, S., … Todd, I. (2016). Dimensional accuracy of Electron Beam Melting (EBM) additive manufacture with regard to weight optimized truss structures. *Journal of Materials Processing Technology*, 229, 128–138. https://doi.org/10.1016/j.jmatprotec.2015.08.028

5 Körner, C. (2016). Additive manufacturing of metallic components by selective electron beam melting - A review. *International Materials Reviews*, 61(5), 361–377. https://doi.org/10.1080/09506608.2016.1176289

6 DebRoy, T., Wei, H. L., Zuback, J. S., Mukherjee, T., Elmer, J. W., Milewski, J. O., … Zhang, W. (2018). Additive manufacturing of metallic components – Process, structure and properties. *Progress in Materials Science*, 92, 112–224

7 Mindt, H. W., Desmaison, O., Megahed, M., Peralta, A., & Neumann, J. (2018). Modeling of Powder Bed Manufacturing Defects. *Journal of Materials Engineering and Performance*, 27(1), 32–43. https://doi.org/10.1007/s11665-017-2874-5

8 Wong, K. V., & Hernandez, A. (2012). A Review of Additive Manufacturing. *ISRN Mechanical Engineering*, 2012, 1–10. https://doi.org/10.5402/2012/208760

9 Raplee, J., Plotkowski, A., Kirka, M. M., Dinwiddie, R., Okello, A., Dehoff, R. R., & Babu, S. S. (2017). Thermographic Microstructure Monitoring in Electron Beam Additive Manufacturing. *Scientific Reports*, 7. https://doi.org/10.1038/srep43554

10 Tammas-Williams, S., Withers, P. J., Todd, I., & Prangnell, P. B. (2017). The Influence of Porosity on Fatigue Crack Initiation in Additively Manufactured Titanium Components. *Scientific Reports*, 7(1). https://doi.org/10.1038/s41598-017-06504-5

11 Bagehorn, S., Wehr, J., & Maier, H. J. (2017). Application of mechanical surface finishing processes for roughness reduction and fatigue improvement of additively manufactured Ti-

6Al-4V parts. *International Journal of Fatigue*, 102, 135–142. https://doi.org/10.1016/j.ijfatigue.2017.05.008

12 P.Edwards, A.O'Conner and M. Ramulu, Electron Beam Additive Manufacturing of Titanium Components: Properties and Performance, A*SME Journal of Manufacturing Science and Engineering*, Vol.135, Dec, 2013, pp.-061016-1-061016-7, doi:10.1115/1.4025773

13 Thompson, M. K., Moroni, G., Vaneker, T., Fadel, G., Campbell, R. I., Gibson, I., … Martina, F. (2016). Design for Additive Manufacturing: Trends, opportunities, considerations, and constraints. *CIRP Annals - Manufacturing Technology*, 65(2), 737–760. https://doi.org/10.1016/j.cirp.2016.05.004

14 Seepersad, C. C. (2014). Challenges and Opportunities in Design for Additive Manufacturing. *3D Printing and Additive Manufacturing*, 1(1), 10–13. https://doi.org/10.1089/3dp.2013.0006

15 Zhu, J. H., Zhang, W. H., & Xia, L. (2016). Topology Optimization in Aircraft and Aerospace Structures Design. *Archives of Computational Methods in Engineering*, 23(4), 595–622. https://doi.org/10.1007/s11831-015-9151-2

16 Leary, M., Merli, L., Torti, F., Mazur, M., & Brandt, M. (2014). Optimal topology for additive manufacture: A method for enabling additive manufacture of support-free optimal structures. *Materials and Design*, 63, 678–690. https://doi.org/10.1016/j.matdes.2014.06.015

17 Vo, T. H., Museau, M., Vignat, F., Villeneuve, F., Ledoux, Y., & Ballu, A. (2018). Typology of geometrical defects in Electron Beam Melting. *Procedia CIRP*, 75, 92–97. https://doi.org/10.1016/j.procir.2018.04.033

18 Rafi, H. K., Karthik, N. V., Gong, H., Starr, T. L., & Stucker, B. E. (2013). Microstructures and mechanical properties of Ti6Al4V parts fabricated by selective laser melting and electron beam melting. *Journal of Materials Engineering and Performance*, 22(12), 3872–3883. https://doi.org/10.1007/s11665-013-0658-0

19 Galarraga, H., Warren, R. J., Lados, D. A., Dehoff, R. R., & Kirka, M. M. (2017). Fatigue crack growth mechanisms at the microstructure scale in as-fabricated and heat treated Ti-6Al-4V ELI manufactured by electron beam melting (EBM). Engineering Fracture Mechanics, 176, 263–280. https://doi.org/10.1016/j.engfracmech.2017.03.024

20 Cabanettes, F., Joubert, A., Chardon, G., Dumas, V., Rech, J., Grosjean, C., & Dimkovski, Z. (2018). Topography of as built surfaces generated in metal additive manufacturing: A multi scale analysis from form to roughness. Precision Engineering, 52(January), 249–265. https://doi.org/10.1016/j.precisioneng.2018.01.002

21 Bendsøe, M. P., & Kikuchi, N. (1988). Generating optimal topologies in structural design using a homogenization method. *Computer Methods in Applied Mechanics and Engineering*, 71(2), 197–224. https://doi.org/10.1016/0045-7825(88)90086-2

22 Bendsøe MP, Sigmund O (2003) Topology optimization: theory, methods and applications. Springer, Berlin

23 Altair Engineering. (2009). SOGECLAIR Aerospace Employs HyperWorks to Optimize Additively Manufactured Aircraft Components: Topology optimization of a large engine pylon structure. Retrieved from http://www.smart-industries.fr/files/exposants/fiches/produits/pdfs/sogeclear_879.pdf

24 Remouchamps, A., Bruyneel, M., Fleury, C., & Grihon, S. (2011). Application of a bi-level scheme including topology optimization to the design of an aircraft pylon. Structural and Multidisciplinary Optimization, 44(6), 739–750. https://doi.org/10.1007/s00158-011-0682-3

25 Chan, K. S., Koike, M., Mason, R. L., & Okabe, T. (2013). Fatigue life of titanium alloys fabricated by additive layer manufacturing techniques for dental implants. *Metallurgical and Materials Transactions A: Physical Metallurgy and Materials Science*, 44(2), 1010–1022. https://doi.org/10.1007/s11661-012-1470-4

26 Greitemeier, D., Palm, F., Syassen, F., & Melz, T. (2017). Fatigue performance of additive manufactured TiAl6V4 using electron and laser beam melting. *International Journal of Fatigue*, 94, 211–217. https://doi.org/10.1016/j.ijfatigue.2016.05.001

27 Lewandowski, J. J., & Seifi, M. (2016). Metal Additive Manufacturing: A Review of Mechanical Properties. *Annual Review of Materials Research*, 46(1), 151–186. https://doi.org/10.1146/annurev-matsci-070115-032024

28 Seifi, M., Dahar, M., Aman, R., Harrysson, O., Beuth, J., & Lewandowski, J. J. (2015). Evaluation of Orientation Dependence of Fracture Toughness and Fatigue Crack Propagation Behavior of As-Deposited ARCAM EBM Ti-6Al-4V. *Jom*, 67(3), 597–607. https://doi.org/10.1007/s11837-015-1298-7

29 Rawal, S., Brantley, J., & Karabudak, N. (2013). Additive manufacturing of Ti-6Al-4V alloy components for spacecraft applications. *RAST 2013 - Proceedings of 6th International Conference on Recent Advances in Space Technologies*, 5–11. https://doi.org/10.1109/RAST.2013.6581260

30 S. Ghods, E. Schultz, C. Wisdom, R. Schur, R. Pahuja, A. Montelione,D. Arola, M. Ramulu, Electron beam additive manufacturing of Ti6Al4V: Evolution of powder morphology and part microstructure with powder reuse. *Materialia* Volume 9 March 2020 Article 100631

31 Jamshidinia, M., Kong, F., & Kovacevic, R. (2013). Numerical Modeling of Heat Distribution in the Electron Beam Melting ® of Ti-6Al-4V . *Journal of Manufacturing Science and Engineering*, 135(6), 061010. https://doi.org/10.1115/1.4025746

32 S. Ghods, E. Schultz, C. Wisdom, R. Schur, R. Pahuja, A. Montelione,D. Arola, M. Ramulu, Electron Beam Additive Manufacturing of Ti6Al4V: Importance of powder reuse on metal porosity, pore size and spatial distribution. Submitted to *Materialia* (2020)

VITA

Eric Bol has always been passionate for all things aviation and space related. From a young age he was a volunteer member of the Civil Air Patrol who rose to the rank of Cadet Major and served as a squadron commander at events. Originally, he targeted a military career in the US Army as a helicopter pilot with an ROTC scholarship; however, due to medical reasons he was disqualified from service within the Department of Defense. From there he then pivoted to target an engineering career in aerospace, and in 2006, Eric received his Bachelor of Science in Aeronautical and Astronautical engineering from the University of Washington College of Engineering.

Following graduation Eric began his career at Boeing as a Flight Test Engineer. For five years he performed duties as a weights engineer and cabin supervisor on numerous test flights across 737’s, 747’s, 767’s, 777’s 787’s. After the first delivery of the 787-8 he transitioned to a design engineer within Propulsion Product Development. In that role his primary responsibility involved studying advanced nacelle architectures for inlets, fan cowls, thrust reversers, core cowls, plugs, pylons, aft fairings, and engine build up (EBU) systems. This is where Eric first learned about additive manufacturing and began investigating potential implementation of the technology in commercial aircraft propulsion products.

With 5 years of experience as an advanced propulsion designer he was recruited into what is now known as the Boeing Additive Manufacturing Innovation Center (BAMIC) to work on metal additive manufacturing development. This is where he discovered his desire to further advance his level of understanding of additive manufacturing and began pursuing his Ph.D. on the subject at the University of Washington Mechanical Engineering department. After 2 years, Eric moved to the Product Development Materials and Fabrication team to develop new material systems and technologies for future aircraft. This is where he resides currently at Boeing, leading technology development projects primarily with titanium.